



LUND UNIVERSITY

The Importance of Dosimetry and Radiobiology in Nuclear Medicine

Quantitative methods and modelling

Stenvall, Anna

2022

[Link to publication](#)

Citation for published version (APA):

Stenvall, A. (2022). *The Importance of Dosimetry and Radiobiology in Nuclear Medicine: Quantitative methods and modelling*. Lund University.

Total number of authors:

1

General rights

Unless other specific re-use rights are stated the following general rights apply:

Copyright and moral rights for the publications made accessible in the public portal are retained by the authors and/or other copyright owners and it is a condition of accessing publications that users recognise and abide by the legal requirements associated with these rights.

- Users may download and print one copy of any publication from the public portal for the purpose of private study or research.
- You may not further distribute the material or use it for any profit-making activity or commercial gain
- You may freely distribute the URL identifying the publication in the public portal

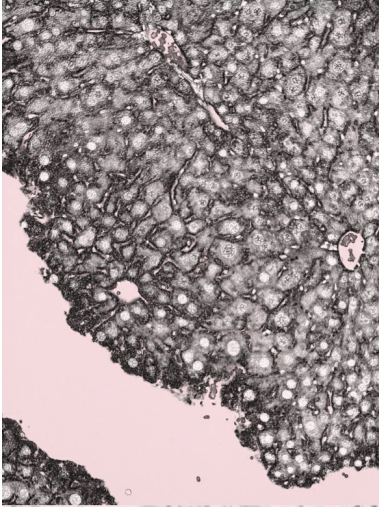
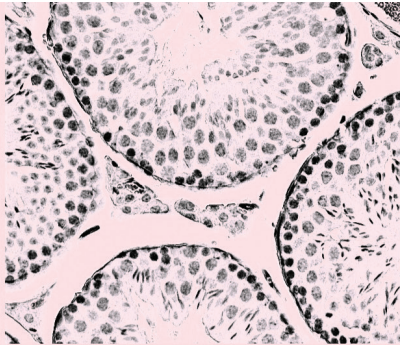
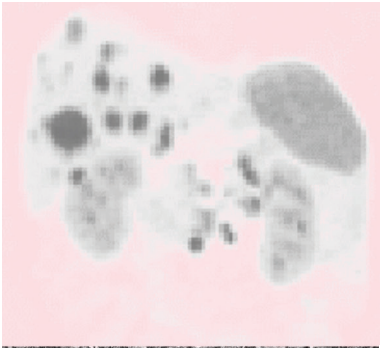
Read more about Creative commons licenses: <https://creativecommons.org/licenses/>

Take down policy

If you believe that this document breaches copyright please contact us providing details, and we will remove access to the work immediately and investigate your claim.

LUND UNIVERSITY

PO Box 117
221 00 Lund
+46 46-222 00 00

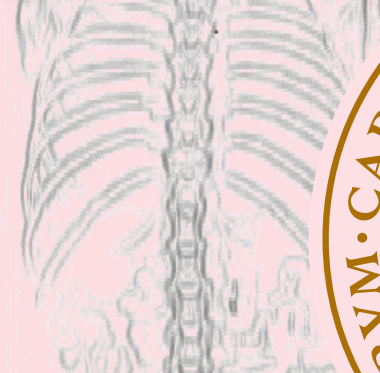
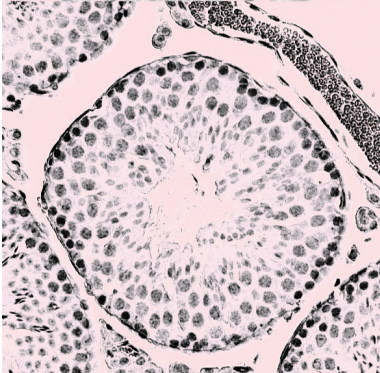
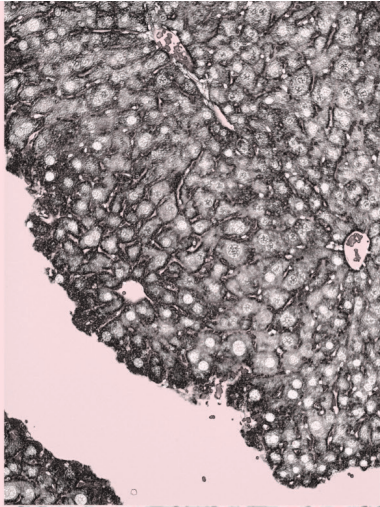
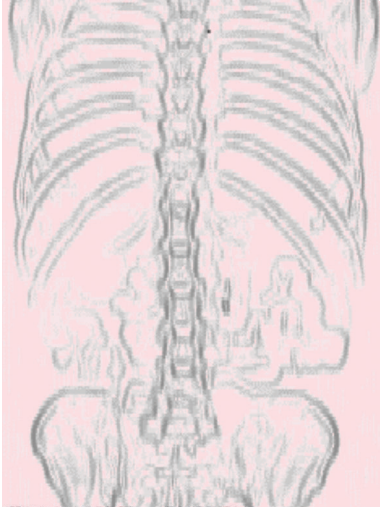


The Importance of Dosimetry and Radiobiology in Nuclear Medicine

Quantitative methods and modelling

ANNA STENVALL

MEDICAL RADIATION PHYSICS, LUND | LUND UNIVERSITY



The Importance of Dosimetry and Radiobiology in Nuclear Medicine

QUANTITATIVE METHODS AND MODELLING

Nuclear medicine uses radioactive pharmaceuticals for diagnostic or therapeutic purposes. The ionizing radiation emitted from the radiopharmaceutical is partially absorbed within the patient's body and internal dosimetry is the method to estimate the absorbed dose to a tumour or a risk organ. This is of special importance in radiopharmaceutical therapy (RPT), where particle-emitting radionuclides are utilized for their therapeutic effect. A better understanding of where and to what extent the radiation energy is deposited, *i.e.* dosimetry, in combination with a better understanding of the irradiation-induced biological processes in tissues and tumours, *i.e.*, radiobiology, is the foundation to establish an absorbed dose-effect relationship.

This book is the doctoral thesis of Anna Stenvall and presents quantitative methods and modelling within the fields of dosimetry and radiobiology in nuclear medicine.



The Importance of Dosimetry and Radiobiology in Nuclear Medicine

Quantitative methods and modelling

The Importance of Dosimetry and Radiobiology in Nuclear Medicine

Quantitative methods and modelling

Anna Stenvall



LUND
UNIVERSITY

Thesis for the degree of Doctor of Philosophy

Faculty opponent


Michael Lassmann, Prof. Dr. rer. nat.

Klinik für Nuklearmedizin, Universitätsklinikum Würzburg,
Würzburg Germany

To be presented with the permission of the Faculty of Science, Lund University, Lund, Sweden. To be defended in the Torsten Landberg lecture hall, 3rd floor in the Radiotherapy building, Klinikgatan 5, Skåne University Hospital, Lund, on Friday the 28th of October 2022 at 09:00.

Organization LUND UNIVERSITY Medical Radiation Physics Skåne University Hospital, Lund SE-221 85 LUND Sweden		Document name DOCTORAL DISSERTATION	
		Date of issue 2022-09-16	
Author(s) Anna Stenvall		Sponsoring organization	
Title and subtitle The Importance of Dosimetry and Radiobiology in Nuclear Medicine. Quantitative methods and modelling.			
Abstract <p>Nuclear medicine uses radioactive pharmaceuticals for diagnostic or therapeutic purposes. The ionizing radiation emitted from the radiopharmaceutical is partially absorbed within the patient's body and internal dosimetry is the method to estimate the absorbed dose to a tumour or risk organ. This is of special importance in radiopharmaceutical therapy (RPT), where particle-emitting radionuclides are utilized for their therapeutic effect. A better understanding of where and to what extent the radiation energy is deposited, <i>i.e.</i> dosimetry, in combination with a better understanding of the irradiation-induced biological processes in tissues and tumours, <i>i.e.</i> radiobiology, is the foundation to establish an absorbed dose-effect relationship. This thesis comprises quantitative methods and modelling within dosimetry and radiobiology, with a special focus on quantitative methods for activity concentration, absorbed dose calculation and quantification of biological effects after nuclear medicine exposures. Nonuniformity of activity distribution and the biological effect of internal irradiation is considered in Paper I and Paper II. When a radiopharmaceutical primarily localizes within specific tissue substructures of an organ, the average absorbed dose to the whole organ may become insufficient for dosimetric analysis. Hence, the nonuniformities of the distribution of activity need to be considered and absorbed dose calculations to part of an organ, cellular, or a sub-cellular structure may be a better predictor of the therapy outcome or normal tissue toxicity. In Paper I, a small-scale anatomical dosimetry model of the liver tissue structure addressed the issue of activity nonuniformity. Monte Carlo simulations were performed to simulate the particle transport from various substructure sources within the organ model for some clinically available radionuclides. The model enabled comparison between the average absorbed dose to the entire organ and the local absorbed dose close to the source region, which for particle emitting radionuclides differed significantly. To address the resulting biological effect after internal irradiation, an <i>ex vivo</i> method using the γH2AX surrogate marker to visualize and quantify DNA double-strand breaks in <i>in vivo</i>-irradiated tissues was developed. The method was demonstrated to be useful for γH2AX-foci quantification in both the fast proliferating, radiosensitive testis tissue and the slow proliferating and more radioresistant liver tissue. Image-based activity quantification and absorbed dose estimation are considered in Paper III and Paper IV, using somatostatin receptor targeting agents for both diagnostic and therapeutic applications for neuroendocrine tumours. In Paper III, the quantitative accuracy of pre-therapeutic ^{111}In-Octreoscan® SPECT/CT and ^{68}Ga-DOTA-TATE PET/CT images was investigated due to the change in clinical method to use PET- instead of SPECT-imaging. Further, the quantitative relationship between the therapeutic pair of DOTA-TATE was investigated in Paper IV. The relationship between activity uptakes observed at ^{68}Ga-DOTA-TATE PET imaging and absorbed doses at subsequent ^{177}Lu-DOTA-TATE therapy was studied. The study demonstrated that on a group level, a higher tumour uptake measured from pre-therapeutic PET images is associated with higher absorbed doses in subsequent therapy with ^{177}Lu-DOTA-TATE. However, on the individual level, there are limitations of using the ^{68}Ga PET as a predictor for therapy absorbed dose.</p>			
Key words Nuclear medicine, radionuclide therapy, radiopharmaceutical therapy, dosimetry, Monte Carlo modelling, radiobiology, γ H2AX, DOTA-TATE, PET, SPECT			
Classification system and/or index terms (if any)			
Supplementary bibliographical information		Language English	
ISSN and key title		ISBN 978-91-8039-359-1 (print) 978-91-8039-360-7 (pdf)	
Recipient's notes		Number of pages 102	Price
		Security classification	

I, the undersigned, being the copyright owner of the abstract of the above-mentioned dissertation, hereby grant to all reference sources permission to publish and disseminate the abstract of the above-mentioned dissertation.

Signature 

Date 2022-09-16

The Importance of Dosimetry and Radiobiology in Nuclear Medicine

Quantitative methods and modelling

by Anna Stenvall



LUND
UNIVERSITY

Cover illustration front: Mosaic of [^{68}Ga]Ga-DOTA-TATE PET MIP images*, high-pass filtered CT MIP images* and H&E stained tissue sections of testis and liver. Images are, to almost unrecognizability, adjusted for brightness and contrast. © Anna Stenvall 2022

*Image data were obtained from two clinical trials, Iluminet (EudraCT No 2011-000240-16, Regionala etikprövningsnämnden Lund, Dnr 2011/287), Gapetto (EudraCT No 2012-004313-13, Regionala etikprövningsnämnden Lund, Dnr 2012/657). Complementary ethics approval was obtained for inclusion of patient data acquired after the closure of Gapetto (Etikprövningsmyndigheten Verksamhetsregion Lund, Dnr 2019-00564). Written informed consent for participation in the studies was obtained from all patients. All procedures performed were in accordance with the ethical standards of the institutional and national research committee and with the principles of the 1964 Declaration of Helsinki and its later amendments.

Paper I: © Institute of Physics and Engineering in Medicine. Reproduced with permission. All rights reserved

Paper II: © The Authors (Open Access)

Paper III: © The Authors (Open Access)

Paper IV: © The Authors (Manuscript)

Medical Radiation Physics, Lund
Faculty of Science, Lund University

ISBN: 978-91-8039-359-1 (print)

ISBN(N+1): 978-91-8039-360-7 (pdf)

Printed in Sweden by Media-Tryck, Lund University

Lund 2022



Media-Tryck is a Nordic Swan Ecolabel certified provider of printed material. Read more about our environmental work at www.mediatryck.lu.se

Printed matter
3041 0903

MADE IN SWEDEN 

Jag hoppas det uppstår en viss förvirring. Det vore skönt.
– **Ernst Kirchsteiger**

Contents

Summary	iii
Populärvetenskaplig sammanfattning	v
Abbreviations and symbols	vii
Preface and list of publications	ix
1 Introduction and aim.....	1
1.1 Nuclear medicine.....	1
1.1.2 The importance of dosimetry and radiobiology.....	2
1.3 Aims of this work.....	3
2 Background	5
2.1 Ionizing radiation and its interaction with matter.....	5
2.2 Ionizing radiation and health effects.....	6
2.3 Dosimetry in nuclear medicine	7
2.3.1 Dosimetry for diagnostic nuclear medicine.....	8
2.3.2 Dosimetry for radiopharmaceutical therapy.....	9
3 MIRDBased internal dosimetry	17
3.1 Fundamental quantities	17
3.2 MIRDB formalism.....	18
3.2.1 Small-scale dosimetry.....	20
3.3 Realistic digital phantoms	22
3.4 The Monte Carlo method.....	22
3.4.1 Radiation transport.....	24
3.4.2 The MCNP code.....	25
3.4.3 The EGS4 code.....	25
3.5 A small-scale dosimetry model of the liver tissue.....	25
4 Radiobiology in nuclear medicine	29
4.1 Classical radiobiology	29
4.1.1 DNA damage and response	30
4.1.2 Cell death and radiobiological modelling.....	32
4.1.3 Stepping away from classical radiobiology.....	34

4.2 Radiobiology in nuclear medicine.....	34
4.3 γ -H2AX as a biomarker for DNA DSB in tissues.....	34
4.4 Visualizing tissue properties	36
4.4.1 Immunolabeling	36
4.4.2 Microscopy imaging.....	38
4.4.3 Image analysis.....	40
4.5 Targeting, labelling, and visualization of γ -H2AX foci in testis and liver tissues after systemic irradiation.....	41
5 Imaging, activity quantification and absorbed dose determination	45
5.1 Imaging in nuclear medicine.....	45
5.2 The gamma camera and SPECT imaging	46
5.2.1 Image degradation	47
5.2.2 SPECT reconstruction and calibration.....	49
5.2.3 Image segmentation.....	51
5.2.4 Time activity determination and absorbed dose calculations	52
5.3 PET camera and imaging.....	54
5.3.1 Image degradation in PET	54
5.3.2 Calibration.....	56
6 Quantitative imaging for neuroendocrine tumours	59
6.1 Biodistribution of ^{68}Ga - and ^{177}Lu -SSTR analogues	60
6.2 Application of pre-therapeutic imaging in SSTR treatment.....	62
6.3 Relationships between uptake of [^{68}Ga]Ga-DOTA-TATE and absorbed dose in [^{177}Lu]Lu-DOTA-TATE therapy	64
7 Summary of papers.....	67
8 Concluding remarks and future directions.....	69
Acknowledgements	73
References	75

Summary

Nuclear medicine uses radioactive pharmaceuticals for diagnostic or therapeutic purposes. The ionizing radiation emitted from the radiopharmaceutical is partially absorbed within the patient's body and internal dosimetry is the method to estimate the absorbed dose to a tumour or risk organ. This is of special importance in radiopharmaceutical therapy (RPT), where particle-emitting radionuclides are utilized for their therapeutic effect. A better understanding of where and to what extent the radiation energy is deposited, *i.e.* dosimetry, in combination with a better understanding of the irradiation-induced biological processes in tissues and tumours, *i.e.*, radiobiology, is the foundation to establish an absorbed dose-effect relationship. This thesis comprises quantitative methods and modelling within dosimetry and radiobiology, with a special focus on quantitative methods for activity concentration, absorbed dose calculation and quantification of biological effects after nuclear medicine exposures.

Nonuniformity of activity distribution and the biological effect of internal irradiation is considered in Paper I and Paper II. When a radiopharmaceutical primarily localizes within specific tissue substructures of an organ, the average absorbed dose to the whole organ may become insufficient for dosimetric analysis. Hence, the nonuniformities of the distribution of activity need to be considered and absorbed dose calculations to part of an organ, cellular, or a sub-cellular structure may be a better predictor of the therapy outcome or normal tissue toxicity. In Paper I, a small-scale anatomical dosimetry model of the liver tissue structure addressed the issue of activity nonuniformity. Monte Carlo simulations were performed to simulate the particle transport from various substructure sources within the organ model for some clinically available radionuclides. The model enabled comparison between the average absorbed dose to the entire organ and the local absorbed dose close to the source region, which for particle emitting radionuclides differed significantly. To address the resulting biological effect after internal irradiation, an *ex vivo* method using the γ H2AX surrogate marker to visualize and quantify DNA double-strand breaks in *in vivo*-irradiated tissues was developed. The method was demonstrated to be useful for γ H2AX-foci quantification in both the fast proliferating, radiosensitive testis tissue and the slow proliferating and more radioresistant liver tissue.

Image-based activity quantification and absorbed dose estimation are considered in Paper III and Paper IV, using somatostatin receptor targeting agents for both diagnostic and therapeutic applications for neuroendocrine tumours. In Paper III, the

quantitative accuracy of pre-therapeutic ^{111}In -Octreoscan® SPECT/CT and ^{68}Ga Ga-DOTA-TATE PET/CT images was investigated due to the change in clinical method to use PET- instead of SPECT-imaging. Further, the quantitative relationship between the theragnostic pair of DOTA-TATE was investigated in Paper IV. The relationship between activity uptakes observed at ^{68}Ga Ga-DOTA-TATE PET imaging and absorbed doses at subsequent ^{177}Lu Lu-DOTA-TATE therapy was studied. The study demonstrated that on a group level, a higher tumour uptake measured from pre-therapeutic PET images is associated with higher absorbed doses in subsequent therapy with ^{177}Lu Lu-DOTA-TATE. However, on the individual level, there are limitations of using the ^{68}Ga PET as a predictor for therapy absorbed dose.

Populärvetenskaplig sammanfattning

Nuklearmedicin är en medicinsk inriktning där radioaktiva läkemedel och strålningen som dessa sänder ut används för att ställa diagnos eller behandla ett flertal olika sjukdomar. Vanligtvis består detta läkemedel av två sammankopplade delar. En radionuklid, som är en radioaktiv variant av ett grundämne och ett läkemedel som är designat för att tas upp i kroppens sjuka område. Det radioaktiva läkemedlet ges ofta till en patient genom en injektion i ett blodkärl, varpå det cirkulerar runt i kroppen för att sedan fördelas i enlighet med patientens fysiologi och läkemedlets specifika egenskaper.

Radionukliden sänder ut joniserande strålning, vilket betyder att strålningen har så mycket energi att den kan skada vävnad genom att slå ut elektroner från molekyler i biologisk vävnad. Strålningen kan vara antingen gammastrålning (fotonstrålning) eller partikelstrålning, där partikelstrålningen har lagom kort räckvidd och ger en större biologisk effekt. Detta nyttjas således för att ge skador på det sjuka området, vilket blir radionuklidterapiens behandlande effekt. Gammastrålning däremot, tar sig till stor del ut från kroppen och kan mätas upp utanför patienten med en scintillationskamera (även kallad gammakamera) eller via positron-emissionstomografi, med en så kallad PET-kamera. Detta ger en nuklearmedicinsk bild av hur det radioaktiva läkemedlet har fördelats i kroppen. Således väljer man olika radionuklider om ändamålet är diagnostik eller terapi. Vissa radionuklider, så som Lutetium-177 (^{177}Lu) kan förutom gammastrålning sända ut betastrålning, som är en typ av partikelstrålning. Denna nuklid används tack vare sin partikelstrålning för strålbehandling av tumörer, medan fotonstrålningen från sönderfallet kan användas för nuklearmedicinsk bildtagning.

För vissa undersökningar eller radionuklidterapi är det av intresse att använda den nuklearmedicinska bilden för att beräkna hur mycket av det radioaktiva läkemedlet som tagits upp i en tumör eller ett organ. Det kallas att kvantifiera det radioaktiva upptaget, eller aktiviteten, och är ett mätvärde som kan användas för att vidare beräkna den stråldos som deponerats i tumören eller organet. Stråldosen anges i storheten absorberad dos och är ett mått den mängd energi som den joniserande strålningen avgett till sin omgivning, i detta fall cellerna i vävnaden. Denna beräkning kan inte göras analytiskt, utan strålningens transport genom vävnaden behöver simuleras i ett datorprogram, enligt den så kallade Monte Carlo metoden.

För att erhålla tillförlitliga resultat över aktivitetupptag och absorberad dos, är det av största vikt att veta hur noggranna dessa bildtagningar och mätmetoder är. I detta arbete har vi undersökt en konventionell gammakamerametod med radionukliden

Indium-111 (^{111}In) och en ny PET-metod med radionukliden Gallium-68 (^{68}Ga) för att erhålla diagnostiska nuklearmedicinska bilder för patienter med neuroendokrina tumörer. Vid diagnostik och behandling av neuroendokrina tumörer används idag samma läkemedel, DOTA-TATE, märkt med ^{68}Ga för diagnostik och med ^{177}Lu för terapi. Möjligheten att använda samma, eller snarlika, läkemedel för såväl diagnostik som terapi (numera kallat teragnostik) ger en unik möjlighet att anpassa behandlingen till den individuella patienten. Dock är utvärderingen av ^{68}Ga -PET-bilderna oftast begränsad till en visuell eller en delvis kvantitativ jämförelse mellan upptag i tumörer och normalorgan. Som en del av denna avhandling har sambandet mellan upptag av [^{68}Ga]Ga-DOA-TATE mätt i PET-bilder och absorberad dos till tumörer och normala organ vid efterföljande behandling med [^{177}Lu]Lu-DOA-TATE studerats. Syftet var att kunna öka förståelsen kring de kvantitativa sambanden. Utöver det så har vi undersökt möjligheten att redan från PET-bilderna kunna förutspå vilken absorberad dos en enskild tumör kommer erhålla vid en efterföljande terapi.

Ytterligare en faktor som försvårar bestämningen av den absorberade dosen till en tumör eller ett organ vid nuklearmedicinsk diagnostik eller terapi, är att det radioaktiva läkemedlet sällan fördelar sig helt jämnt inom organet. För att ta hänsyn till detta har vi i detta arbete utvecklat en ny dosimetrisk modell för levervävnaden, som med hjälp av Monte Carlo modellen kan beräkna en absorberad dos tar hänsyn till denna ojämna fördelning. Modellen och simuleringarna visar att ett uträknat medelvärde av stråldosen över hela organet inte är tillräckligt noggrant i fall då det radioaktiva läkemedlets fördelning är mycket ojämn och de emitterade partiklarnas räckvidd är kort.

En noggrann bestämning av den absorberade dosen behövs också för att bestämma ett samband mellan exponeringen med joniserande strålning och dess biologiska effekt på den vävnad vari energin deponeras. Som en del i denna avhandling har en experimentell metod utvecklats för att kvantifiera en viss typ av DNA skada, som kallas dubbelsträngsbrott. Denna skada kan uppstå i en cells arvs massa efter exponering för joniserande strålning. Med hjälp av lasermikroskopi har vi kunnat visualisera och kvantifiera dessa dubbelsträngsbrott i musvävnad efter intern bestrålning från det radioaktiva ämnet ^{111}In . Med dessa modeller och metoder har vi fått nya sätt att noggrannare bestämma både absorberad dos och dess resulterande biologiska effekt för olika celltyper. Vi hoppas därmed kunna finna starkare dos-responssamband, som i framtiden ska kunna användas för att förfina doseringen av det radioaktiva läkemedlet, för att på så sätt maximera behandlingseffekten utan att risken för strålskador på friska organ blir oacceptabelt hög.

Abbreviations and symbols

1D, 2D, 3D	one-, two-, and three-dimensional
BED	biologically effective dose
CLSM	confocal laser scanning microscopy
CT	computed tomography
CZT	cadmium zinc telluride
DAPI	fluorescent intercalating DNA stain (4',6-diamidino-2-phenylindole)
DNA	deoxyribonucleic acid
DOTA	a linker molecule (a chelator) with the formula $(\text{CH}_2\text{CH}_2\text{NCH}_2\text{CO}_2\text{H})_4$
DTPA	a linker molecule named diethylenetriaminepentaacetic acid
EANM	European Association of Nuclear Medicine
EBRT	external beam radiotherapy
FDA	Food and Drug Administration
FOV	field of view
FWHM	full width at half maximum
H2AX	member X of the H2A histone family
H&E	haematoxylin and eosin stain
ICRP	International Commission on Radiological Protection
ICRU	International Commission on Radiation Units & Measurements
IF	immunofluorescence
IHC	immunohistochemistry
LET	linear energy transfer
LOR	line of response
LQ	linear quadratic
MIP	maximum intensity projection

MIRD	Medical Internal Radiation Dose
MTD	maximum tolerable dose
NaI(Tl)	thallium-doped sodium-iodide
NET	neuroendocrine tumour
μ	(mu) is the prefix for micro, denoting a factor of 10^{-6} (one millionth)
p.i.	post injection
PK	pharmacokinetics
PBPK	physiologically based pharmacokinetic
PET	positron emission tomography
PMT	photomultiplier tube
PRRT	peptide receptor radionuclide therapy
PVE	partial volume effect
RBE	relative biological effectiveness
RC	recovery coefficient
RIT	radioimmunotherapy
ROS	reactive oxygen species
RPT	radiopharmaceutical therapy
SF	surviving fraction
SiPMT	Silicon photomultiplier
SIRT	selective internal radiation therapy
SPECT	single-photon emission computed tomography
SSTR	somatostatin receptor
SUV	standardised uptake value
TIA	time integrated activity
TIAC	time integrated activity curve
ToF	time of flight
UNSCEAR	United Nations Scientific Committee on the Effects of Atomic Radiation
γ H2AX	phosphorylated member X of the H2A histone family

Preface and list of publications

This doctoral thesis presents my contributions to the field of internal dosimetry and radiobiology studies within the field of radiation physics in diagnostics and therapies in nuclear medicine.

The studies include simulations and anatomical modelling, pre-clinical studies and *ex vivo* experiments, and clinical studies using phantoms and patient data. The thesis sheds light on the importance of radiation dosimetry and radiobiology in nuclear medicine.

The thesis is based on the following publications, referred to by their Roman numerals:

Paper I: A small-scale anatomical dosimetry model of the liver

Stenvall A, Larsson E, Strand SE, Jönsson BA.
Physics in Medicine and Biology. 2014. **59**, pp 3353-3371

The scientific foundation for Paper I was formulated during the fast rise of selective internal radiation therapy (SIRT) treatments of liver metastasis and increasing concern about doses absorbed by the liver during radioimmunotherapy. The small-scale anatomical model was initially developed as my master's thesis work, which then evolved into Paper I. This project developed a Monte Carlo-based small-scale dosimetry model mimicking the microarchitecture of the liver lobule. The aim was to determine S values for different source-target combinations within the liver tissue microstructure; for, at the time, common radionuclides used for therapy as well as for diagnostic purposes. The purpose of the study was to illustrate a case where the whole organ average absorbed dose, according to conventional MIRD formalism, may not be a good predictor of the biological liver response. This is because an inhomogeneous radiopharmaceutical distribution could result in a non-uniform absorbed dose distribution within the organ tissue microarchitecture.

Contributions

I took part in the study design and the development of the methodology. I took a significant part in designing the specific anatomical model, performing the Monte Carlo simulations, the data analysis, and presenting of the results. I drafted the manuscript and was the main and corresponding author.

Paper II: Quantitative γ -H2AX immunofluorescence method for DNA double-strand break analysis in testis and liver after intravenous administration of $^{111}\text{InCl}_3$

Stenvall A, Larsson E, Holmqvist B, Strand SE, Jönsson BA.
EJNMMI Research. 2020. **10**: p. 22

In this paper, at the time of initialisation, the use of the γ -H2AX foci as a biological marker for radiation-induced DNA double-strand breaks was novel and rarely used as a biomarker after or during systemic irradiations with radionuclides. Thus, the central investigation developed and validated an *ex vivo* method for identifying and quantifying γ -H2AX foci in tissue biopsies from mice after intravenous administration and internal irradiation from $^{111}\text{InCl}_3$. The research question that arose after the method was developed was an investigation of the induction of γ -H2AX foci as a function of time after injection, and the resulting absorbed dose. Two intrinsically different tissues were chosen: highly-proliferative and highly radiosensitive testicular tissue, and the normally non-proliferating and radioresistant liver tissue.

Contributions

I took a significant part in the study design and the development of the study's methodology. I performed the animal studies and the staining of tissue sections and microscopy imaging. I took a significant part in the absorbed dose calculation, data analysis, and interpretation of the results. I drafted the manuscript and was the main and corresponding author.

Paper III: Quantitative analysis of phantom studies of ^{111}In and ^{68}Ga imaging of neuroendocrine tumours

Jönsson L, **Stenvall A**, Mattsson E, Larsson E, Sundlöv A, Ohlsson T, Hindorf C.
EJNMMI Physics. 2018. **5**: p. 5

This paper's idea arose with the rise of ^{68}Ga -DOTA-conjugated peptides for functional PET/CT imaging of neuroendocrine tumours, a technique that gradually replaced conventional ^{111}In -Octreotide scintigraphy imaging. The research purpose was an investigation of the possibility of replacing conventional qualitative image quality evaluation with a quantitative method. Therefore, this study examined the differences in image quality between the two imaging techniques and investigated the accuracy of ^{68}Ga -PET and ^{111}In -SPECT image quantification. A phantom study was designed to examine the possibility of accurately quantifying the activity and volume for differently-sized spheres for varying sphere-to-background concentration ratios for several segmentation methods.

Contributions

I took a significant part in the study design, the method development. I performed the phantom measurements and took a significant part in data analysis. I took part in the writing of the manuscript.

Paper IV – Relationships between uptake of [⁶⁸Ga]Ga-DOTA-TATE and absorbed dose in [¹⁷⁷Lu]Lu-DOTA-TATE therapy

Stenvall A*, Gustafsson J*, Larsson E, Roth D, Sundlöv A, Jönsson L, Hindorf C, Ohlsson T, Sjögreen Gleisner K.

Manuscript submitted to EJNMMI Research 2022-09-06

****Shared first authorship***

This paper is based on data from two clinical studies performed at the Skåne University Hospital, involving patients with neuroendocrine tumours (NETs), undergoing both pre-therapy PET/CT-imaging with the diagnostic pharmaceutical [⁶⁸Ga]-Ga-DOTA-TATE, and radiopharmaceutical therapy and SPECT/CT- and planar peri-therapeutic imaging with the therapeutic radiopharmaceutical [¹⁷⁷Lu]Lu-DOTA-TATE. The use of the same or similar peptides for imaging and therapy offers unique assistance in therapy stratification. Still, there is no consensus today on the predictive value of ⁶⁸Ga-DOTA-TATE PET/CT imaging concerning the response, absorbed dose, or activity uptake in tumours and organs in [¹⁷⁷Lu]Lu-DOTA-TATE therapy. This research project aimed to deepen the understanding of the relationship between the uptake of [⁶⁸Ga]-Ga-DOTA-TATE and the absorbed dose and activity concentration in tumours and organs in the subsequent [¹⁷⁷Lu]Lu-DOTA-TATE therapy. Furthermore, the possibility of predicting ¹⁷⁷Lu-absorbed dose in tumours based on pre-therapeutic ⁶⁸Ga-uptake is investigated, using population-based effective half-lives for G1- and G2-graded tumours.

Contributions

I took a significant part in study design and patient data collection. I participated in the method development, analysed the data, and interpreted the results. I took a small part in image processing and statistical analysis. I drafted the manuscript and was the shared first author.

Paper I: © Institute of Physics and Engineering in Medicine. Reproduced with permission. All rights reserved

Paper II: © The Authors (Open Access)

Paper III: © The Authors (Open Access)

Paper IV: © The Authors (Manuscript)

1 Introduction and aim

In this chapter, the reader is shortly introduced to the diagnostic and therapeutic applications of nuclear medicine and the need for the development of activity concentration quantification, absorbed dose calculations and quantification of biological effects after nuclear medicine exposures. The aims of this thesis are presented, and the research questions stated at the beginning of this thesis project are placed within the broader context of radiation physics within nuclear medicine diagnostics and therapy.

1.1 Nuclear medicine

Nuclear medicine refers to medical procedures, including diagnostics and therapies, where a radioactive agent is administered to a patient. The radiopharmaceutical is systemically distributed, *i.e.*, treatment agents are circulated in the bloodstream rather than being aimed at one specific area. Pharmaceuticals are then delivered through extravasation through capillaries, and their pharmacokinetics depend on the specific pharmaceutical or radionuclide administered, in combination with patient physiology. In most diagnostic and some therapeutic applications, the *in vivo* distribution of the radiopharmaceutical after its administration is imaged using either a gamma camera or a positron emission tomography (PET) camera.

The term “functional imaging” is used for diagnostic purposes, indicating that a specific physiological function within the body is evaluated by imaging. The isotope chosen is a photon emitter with half-lives in the order of hours, and the amount of activity delivered is below harmful radiation levels. The amount of the pharmaceutical is low, so as to not affect the physiology of the studied process. On the contrary, radiopharmaceutical therapy (RPT) intends to create a biological effect on a specific target area within the patient's body. This effect is achieved using radionuclides emitting particle radiation, which has a more significant biological effect than photon irradiation, combined with a half-life in the order of days. For RPT, a pre-calculated activity is administered to the patient, delivering its radiation energy continuously while the radiopharmaceutical is retained within the body.

Theragnostic agents are being developed and increasingly used in cases where the same or similar pharmaceutical is labelled with a radionuclide suitable for either imaging or therapy. Hence the fusion of the terms “therapy” and “diagnostics”. This is now widely

used in the imaging and therapy of neuroendocrine tumours (NETs), where the molecular target is the somatostatin receptor (SSTR) expressed on the tumour cell surface. For diagnostic PET imaging, the most common tracers used today are ^{68}Ga -labelled chelator-conjugated somatostatin analogues DOTA-TATE and -TOC, whereas ^{177}Lu -labelled DOTA-TATE or -TOC is used in NET therapy [1]. Information from the diagnostic tool SSTR-PET is used for therapy stratification.

For all patients undergoing radionuclide therapies, a patient-specific target volume should be individually planned according to EU Council Directive 2013/59/EURATOM [2]; including keeping absorbed doses to non-target tissues as low as reasonably achievable (ALARA). This is not the situation for many cases of RPT, in which treatment is instead given using a fixed activity or an activity scaled to body size. Since pharmacokinetics are likely to vary from patient to patient, the activity accumulated by tumours and healthy organs will, for all patients, be individualised, resulting in a patient-dependent absorbed dose. For successful treatment, the absorbed dose to the target volume needs to reach a certain level, while at the same time, the absorbed doses to non-target organs should not exceed certain levels, to avoid serious side effects. With a fixed activity or an activity scaled by body size, reassessed so as to not induce severe complications, the treatment effect is unlikely to be maximized. Hence, there is increasing interest in methods for quantifying radiopharmaceutical uptake and retention, and thus the resulting absorbed dose, as well as the resulting quantifiable biological effect on both tumours and at-risk organs, and their relation to patient outcome.

1.1.2 The importance of dosimetry and radiobiology

This thesis presents quantitative methods for activity concentration, absorbed dose calculation, and quantification of biological effects in nuclear medicine. In nuclear medicine and radiopharmaceutical therapies, the radiation source often gives rise to non-straightforward exposures, consisting of mixed radiation quality, low absorbed dose rate, time-varying prolonged exposures, and inhomogeneous absorbed dose distributions. Currently, dose–effect relationships are not fully utilized in most radionuclide therapies. The prerequisites for the determination of either the absorbed dose or the biological effect are not fully understood in relation to the heterogenous distribution of the radiopharmaceuticals, including determination of the absorbed dose at the relevant tissue, cellular, or sub-cellular scale, as well as the determination of the relevant biological effect on the systemic, cellular, or molecular level.

Today, only sparse evidence exists as to the advantages of patient-specific dosimetry. However, the hypothesis is that a better understanding of where and to what extent both the radiation energy is deposited—*i.e.* therapy dosimetry—and the subsequent radiation-related processes in tissues and tumours—*i.e.* radiobiology—is the foundation to better assess pre-clinical as well as clinical therapy outcomes, and normal tissue complications.

This thesis addresses some of these issues by developing a more realistic dosimetry model for liver micro-architecture, where simulations of inhomogeneous activity distribution can be performed, and the resulting absorbed doses studied. The second focus of the thesis is developing methods for detecting and quantifying ionizing radiation-induced tissue effects—such as the possibly lethal DNA double-strand break—within tissue samples from internally-irradiated laboratory animals. The third and fourth foci of the thesis concern the role of medical radiation physics within the field of clinical nuclear medicine. They focus on the quantitative accuracy of clinical nuclear medicine imaging systems, and how the extracted data can be used as predictive markers for improved therapy selection.

1.3 Aims of this work

The work presented in this thesis is intended to develop and investigate quantitative methods within the fields of nuclear medicine dosimetry and radiobiology. The overall goal was to provide methods for more detailed quantification of activity concentration, absorbed dose, and the resulting biological effects in order to better understand the biological endpoints following nuclear medicine exposure and through this, the ability to deliver safe and effective treatments to the patient.

The specific aims of the four papers framed by this thesis were:

- I. To develop a representative small-scale dosimetry model for liver tissue microstructure for calculation of the absorbed dose in different cell types in liver tissue from radionuclides inhomogeneously distributed within the portal tract or accumulated within liver-specific macrophages.
- II. To develop an experimental method for visualisation and quantification of radiation-induced DNA double-strand breaks in specific cell types in tissues of the testes and liver after systemic administration of $^{111}\text{InCl}_3$.
- III. To investigate the differences in image quality, detectability, and accuracy in activity quantification of spherical structures, as surrogates for tumours, in neuroendocrine tumour imaging with ^{111}In -Ocreoscan® SPECT/CT and ^{68}Ga [Ga-DOTA-TATE PET/CT and to investigate the possibilities of quantitative image quality evaluation.
- IV. To investigate the relationship between activity uptake quantified in ^{68}Ga [Ga-DOTA-TATE PET/CT imaging and absorbed doses to organs and tumours in ^{177}Lu [Lu-DOTA-TATE therapy, to better assess the diagnostic information in therapy stratification.

2 Background

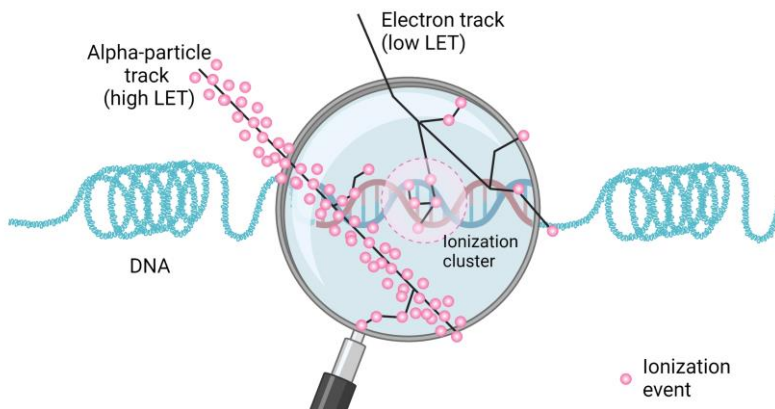
This chapter presents the nature of radionuclides and ionizing radiation, and the concept of absorbed dose is defined upon and elaborated. The chapter aims to define health effects as they are related to the absorbed dose. A section is then dedicated to radionuclide therapies and results from clinical and dosimetry studies are presented.

2.1 Ionizing radiation and its interaction with matter

Radioactive decay, the origin of ionizing radiation from radionuclides, refers to the spontaneous transformation of atoms, including changes in the nuclei or the energy states of the nuclei. The energy released in such a transformation is emitted as particles (*e.g.* alpha particles, electrons, or positrons) and/or photons. Such an unstable nucleus is called a radionuclide. The transformation of an atom is a stochastic process involving the whole atom. A nuclear transformation can also involve the atomic shell structure, causing the emission or capture of electrons, emission of photons, or both. The result of the transformation is another nuclide or a transition to a lower energy state of the same nuclide.

Ionizing radiation interacts with matter in a series of interactive processes in which radiation energy is transferred to other secondary particles and finally becomes deposited in the matter. The energy deposited in the material—the mean energy imparted, divided by the mass of the volume of interest—is denoted “absorbed dose”. It is defined in units of joule per kilogram and has the special name gray (Gy) [3]. Dosimetry is the measure, calculation, or assessment of the absorbed dose received by a dosimeter, detector, or biological matter.

The yield and spatial distribution of the ionizations are different for high- and low-linear energy transfer (LET) radiation. The LET is the mean energy, dE_{Δ} , lost by the charged particle that is absorbed locally along the particle track while traversing a distance; dl , defined as $L_{\Delta} = \frac{dE_{\Delta}}{dl}$ [3]. Δ is the threshold energy used to define local energy absorption, since energy depositions higher than Δ will produce delta particles that cannot be considered locally absorbed. The difference in LET between radiation types can be orders of magnitude; see Figure 2.1.



Figur 2.1. Illustration of radiation tracks from low- and high-LET tracks. Electrons illustrate the low-LET tracks and the high-LET track is illustrated by an alpha particle. Picture inspiration from [4], created with BioRender.com.

2.2 Ionizing radiation and health effects

The biological response of cells exposed to ionizing radiation depends on the radiation absorbed dose. Thus, numerous physical and biological factors also affect the biological response, such as radiation quality, LET and the absorbed dose rate, the fraction of the organs irradiated, or the radionuclide distribution within the tissues. The biological factors affecting this response include cell proliferation rate and intrinsic radiosensitivity, the cell cycle phase at the time of irradiation, and the alignment of functional subunits in normal tissues. In its simplest form, ionizing radiation's general health effects are reported as functions of absorbed dose after short-term low-LET exposures, often termed “acute irradiation”.

According to the terminology for ranges of absorbed doses used by the United Nations Scientific Committee on the Effects of Atomic Radiation (UNSCEAR), absorbed doses from low LET radiation to the whole body or to a specific organ or tissue below 10 mGy are considered “very low”. Absorbed doses between 10 mGy and 100 mGy are considered “low”; 100 mGy to 1 Gy is considered “moderate”; and absorbed doses greater than 1 Gy are considered “high” [5].

Deterministic effects from irradiation exposures are characterized by a threshold absorbed dose. If that threshold is exceeded, the effect's excess probability and severity will increase with the absorbed dose. Deterministic effects arising after acute exposure to ionizing radiation are well studied, and a robust body of scientific evidence about its occurrence is present [5]. According to the International Commission on Radiological Protection (ICRP), the observed deterministic effects from acute low LET irradiation range from observations of temporary male sterility occurring three to nine weeks after acute irradiation of the testes at absorbed doses of 0.1 Gy to permanent male and

female sterility within three weeks after absorbed doses in the testes and ovaries of 6 Gy and 3 Gy respectively. Skin burns within three weeks or acute pneumonitis within one to three months after acute irradiation of 5–10 Gy and 6–7 Gy, respectively [6]. Several cells need to be functionally inactivated or killed for severe deterministic effects, leading to a major impact on the tissue of an organ or the whole organism [5].

In contrast to deterministic effects, stochastic effects depend on cell modifications, such as radiation-induced cancers. Stochastic effects are characterised by the absence of a threshold-absorbed dose, whereupon any exposure is presumed to be associated with an increased probability for the effect to occur. However, the severity of a stochastic effect does not increase with absorbed dose. Stochastic effects, initialized by ionizing radiation, are indistinguishable from those caused by other sources. Nevertheless, biological indicators of exposure to ionizing radiation exist (Table 1), even though none are uniquely associated with radiation exposure, nor is it guaranteed that a health effect will manifest in that individual after detection.

Table 1. Biological indicators of exposure to ionizing radiation. Table adopted from [5].

Biological indicator	Lowest absorbed dose range from acute exposure (Gy)	Explanation
Blood cells	0.5–1	Reduction of the number of lymphocytes. Early response to radiation exposure.
Reciprocal translocations	0.3–0.5	Useful in assessing radiation exposures that occurred a long time ago.
Micronuclei	0.1–0.3	A small nucleus formed whenever a chromosome or a chromosomal fragment is not incorporated into one of the daughter nuclei during cell division.
Dicentric chromosomes	0.05–0.1	An asymmetric misrepair forms chromosomes with two centromeres and chromosomes without. Some chemicals are also known to cause dicentric chromosomal aberrations.
γ -H2AX foci	0.003	The most sensitive biological indicator found up until now.

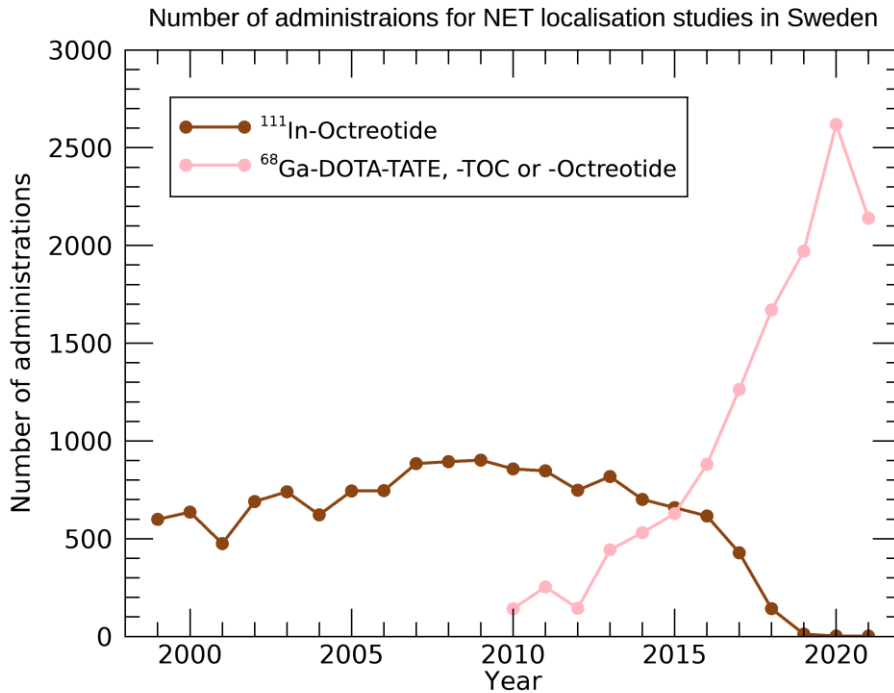
Today, the most sensitive biological indicator of exposure to ionizing radiation is the biomarker γ -H2AX foci, a target initiated in the early DNA damage response to a double-strand break (details presented in chapter 4.3 γ -H2AX as a biomarker for DNA DSB in tissues). The use of γ -H2AX in radiobiology and radiation protection started in the early 2010s. It was attractive due to its high sensitivity even after absorbed doses as low as 3 mGy, and its ability to visualise the actual site of DNA damage spatially in single cell nuclei or at the tissue level. However, γ -H2AX foci are not uniquely associated with DNA repair after ionizing radiation exposure.

2.3 Dosimetry in nuclear medicine

During nuclear medicine diagnostic or radiopharmaceutical therapy, patients are administered a radiopharmaceutical agent via intravenous, intra-arterial, or oral administration. In Sweden in 2021, more than 100,000 patients were undergoing diagnostic nuclear medicine examination, and around 3,000 patients were treated with RPT [7].

2.3.1 Dosimetry for diagnostic nuclear medicine

In diagnostic nuclear medicine, the amount of activity administered per diagnostic investigation and the type of radionuclide used has a very low risk of inducing any harmful biological effect. Dosimetry in diagnostic nuclear medicine was developed to assess these radiation risks at the population level, using population-based pharmacokinetic models and population-based anatomical models for absorbed dose factors. To achieve the radiation risk, the mean absorbed dose to a target region is weighted by a radiation quality factor, intended to account for the difference in damage profile depending on radiation quality. For low LET radiation, the quality factor is taken to be unity. Furthermore, weighting factors for specific organs or tissues are applied, representing the relative radiation sensitivity of each irradiated organ. The sum of the radiation-risk-weighted equivalent doses, the effective dose (in units of joule per kilogram named sievert (Sv)), to a reference patient, based on biokinetic data is presented in the ICRP publications 53 [8], 80 [9] and 106 [10] and the mathematical Medical Internal Radiation Dose (MIRD) phantoms [11]. Effective doses for a reference patient undergoing typical diagnostic investigations range from 0.36 mSv in a 30 MBq ^{99m}Tc -lung ventilation study to 9.6 mSv for a one-day myocardial perfusion scintigraphy protocol with an administered activity of 1200 MBq [12]. In 2013, when this thesis work was initiated, two diagnostic imaging methods for neuroendocrine tumours were available. The conventional SPECT-compatible ^{111}In -Octreotide and the uprising PET-compatible ^{68}Ga -DOTA-TATE, -TOC or -Octreotide. The ^{68}Ga -labelled tracer became the new method of choice in Sweden after 2015, as illustrated in Figure 2.2. The effective dose from 185 MBq ^{111}In -Octreotide is 10 mSv, whereas the effective dose from 175 MBq ^{68}Ga -DOTA-TATE (assumed 2.5 MBq/kg for a patient of 70 kg) is lower by a factor of two, reaching 5.1 mSv [12].



Figur 2.2. The development of the number of radiopharmaceutical administrations for neuroendocrine tumour localization studies in Sweden from 1999 to 2021. The conventional radiopharmaceutical ^{111}In -Octreotide was gradually replaced by ^{68}Ga -labelled somatostatin analogues, which became the dominant radiopharmaceutical after 2015. Data from the Swedish isotope statistic register [7].

2.3.2 Dosimetry for radiopharmaceutical therapy

For radiotherapeutic applications activity is administered to reach high absorbed doses in target regions where biological effects are desired. By designing a targeting agent specific to the target region, in combination with a suitable radionuclide, selective irradiation of a particular tissue is possible while absorbed doses to other tissues remain within tolerable limits. The population-based methodology used for dosimetry in diagnostics and radiation protection failed to show compelling evidence for better treatment outcomes with dosimetry-based treatment planning [13]. Dosimetry formalisms utilizing the patient's unique anatomy and individual biokinetics—based on quantitative imaging within the field of radiopharmaceutical therapy—are now available. But despite the exclusive ability to track and quantify the radiopharmaceutical in both target and non-target tissues at the desired time point after administration, as per the requirements of European Council directive article 56 [2], dosimetry is not always performed in RPT.

To allow for change and take steps toward compliance with the demands in article 56, in 2020 the EANM clarified three levels of absorbed dose handling [14], which was inspired by the framework for prescribing, recording and reporting absorbed doses defined for different radiation therapy modalities by the International Commission on Radiation Units & Measurements (ICRU). In late 2021, ICRU published report 96 on dosimetry-guided radiopharmaceutical therapy, where this framework was implemented for RPT [13]. The adoption of this framework by the EANM resulted in the following formulations for optimization and prescription of nuclear medicine treatments: (1) activity-based prescription and cohort-average dosimetry; (2) activity-based prescription and patient-specific dosimetry; and (3) dosimetry-guided patient-specific prescription and verification. Most treatments in nuclear medicine can be considered standardized treatments, where level 1 compliance is the minimum requirement. To fulfil the requirements for level 2 compliance, recording and reporting of the absorbed dose to at-risk regions and optionally also to treatment regions are required, and for level 3 compliance the prescribed administered activity is calculated based on the absorbed dose intended to be delivered to the treatment region or at-risk regions [14].

The number of new radionuclide therapies that have obtained marketing authorization within the EU has increased in recent years including $^{223}\text{RaCl}_2$ (Xofigo®, Bayer, Germany) for bone metastasis [15], [^{177}Lu]Lu-DOTA-TATE (Lutathera®, Advance Accelerator Applications, USA, Inc. Millburn, NJ) for neuroendocrine tumours [16], and in a late-stage clinical trial [^{177}Lu]Lu-PSMA-617 for metastatic castration-resistant prostate cancer [17], which in early 2022 received marketing approval by the Food and Drug Administration (FDA) in the US under the name Pluvicto™ (Advance Accelerator Applications, USA, Inc. Millburn, NJ). But despite the large number of clinical trials substantiating this, prospective evidence of an absorbed dose-effect response that could guide personalized treatment has not been achieved [18]. Most dose-effect relationships after RPT have been derived from retrospective studies, and the question of whether an absorbed dose-response exists to guide personalized treatment has long stood unanswered [19]. First, in 2021, the trial DOSISPHERE [20], concerning ^{90}Y -microsphere treatments of liver cancer, showed evidence for the superiority of dosimetry-guided patient-specific prescription.

The most common radiopharmaceutical therapies are treatments of benign hyperthyroidism and thyroid cancer with $^{131}\text{I}(\text{NaI})$ [7], using the targeting ability of the radionuclide itself via the natural uptake of iodine by the thyroid. Whereas dosimetry for benign thyroid disease often is performed according to level 3 [21], radioiodine therapies for thyroid cancer usually have a large therapeutic window, and dosimetry is rarely performed [22].

2.3.1.1 Peptide receptor radionuclide therapy

Peptide receptor radionuclide therapy (PRRT), designed to have a high affinity and specificity to tumour cells, is an increasingly common form of RPT for treating tumours of neuroendocrine origin. The therapy evolved from the diagnostic gamma-

camera imaging of somatostatin expressing tumours using ^{123}I -Octreotide [23, 24] and ^{111}In -DTPA-Octreotide [23]. The ^{111}In labelled Octreotide was first proposed for therapeutic applications due to the internalization of the radiopeptide and the emission of short-range Auger electrons and conversion electron emissions [25]. Therapies showed modest results, and for the next generation of radiopharmaceuticals for PRRT, the DOTA chelator made it possible to create stable conjugation with the high energy β -emitters ^{90}Y and later ^{177}Lu , based on the hypothesis of increased efficacy due to the longer particle range in tissue [26]. The longer range of ^{90}Y (E_{max} : 2.28 MeV [27], approximate average path length: 11 mm [28]) compared to ^{177}Lu (E_{max} : 0.49 MeV [29], approximate average path length: 2 mm) [28], thus showed higher occurrence and severity of renal toxicity [30]. Lutetium-177 is also of particular interest in RPT, due to its decay, which in addition to β -particles, also emits low and medium energy photons of 113 keV and 208 keV, which are suitable for gamma camera imaging.

Finally, radionuclide therapy targeting somatostatin receptor subtype (SST₂)-positive midgut neuroendocrine tumours (NETs) with [^{177}Lu]Lu-DOTA-TATE was studied in the NETTER-1 phase III trial [31]. The study showed clear progression-free survival and overall survival benefits for the patient receiving [^{177}Lu]Lu-DOTA-TATE. The [^{177}Lu]Lu-DOTA-TATE was delivered in four fixed activity infusions of 7.4 GBq every 8 weeks, therefore it is assumed that these figures could be further improved by applying patient-specific dosimetry. The therapy is limited by the potential adverse effects on the kidneys and bone marrow, which emphasizes further optimizations [16]. Regardless, in 2018 the use of four fixed activity infusions of [^{177}Lu]Lu-DOTA-TATE was authorized for use in the European Union, and optimism rose for radiopharmaceutical therapy.

In the phase II trial “Iuminet”, conducted at two referral centres in Sweden (Skåne University Hospital, Lund and Sahlgrenska University Hospital, Gothenburg), the number of ^{177}Lu -PRRT cycles was individualized based on kidney dosimetry. Patients received treatment up to a cumulative biological effective dose of 27 ± 2 Gy, with further treatment up to 40 ± 2 Gy for patients complying with specific criteria for kidney function and age [32]. The median number of treatment cycles for all patients was 5 (1–9), with 51 patients (53%) receiving more than four cycles. The results demonstrated that dosimetry-based PRRT is safe and effective, and that the progression-free survival and overall survival were the highest for kidney BED above 29 Gy [33]. Still, there is an unmet need for randomized trials in PRRT which intend to demonstrate and quantify the risks and benefits of personalized versus standard treatment schemes.

2.3.1.2 Radioembolization using ^{90}Y -microspheres

For treatment of liver cancer and liver metastases with intrahepatic arterial-delivered radioactive compounds (selective internal radiation therapy (SIRT)), healthy liver tissue is dose-limiting. Today, the most common SIRT treatments use ^{90}Y -labeled microspheres for radioembolization, enabling the delivery of high absorbed doses to small target volumes with a relatively low toxicity profile [34]. The theory behind the

treatment technique is to create point sources of radiation that preferentially accumulate in the peri- and intra-tumoral arterial vasculature. Hence, microspheres are injected into the hepatic artery since metastatic lesions in the liver almost exclusively receive blood supply from the hepatic artery. In contrast, normal liver tissue is primarily supplied by blood from the portal vein [35]. The microspheres are neither metabolized nor excreted, so the effective half-life is equal to the physical half-life, and the microspheres will persist in the liver. The normal tissue adjacent to deposition locations of the radiolabelled microspheres will be exposed to the energy emitted from the radionuclides.

The DOSISPHERE trial [20] showed a significantly improved response rate for dosimetry-guided patient-specific prescription, where ≥ 205 Gy was delivered to the largest treated lesion. In the non-dosimetry group, the average absorbed dose to the normal liver reached 79 Gy, whereas in the dosimetry-guided group, the average absorbed dose to the liver reached 120 Gy (with one patient receiving 150 Gy). Liver function alterations were manageable, and only one patient in the dosimetry-guided group experienced liver failure [36]. Even though the SIRT treatment is considered to be treatment with a medical device and thus not a radiopharmaceutical therapy, it is still considered, due to the rising interest in SIRT that took place at the time this thesis was begun, and because it is an ideal model for absorbed dose calculation of heterogeneously-distributed radiopharmaceuticals.

2.3.1.3 Normal tissue exposure during RPT

In general, establishing the tumour-absorbed dose-versus-response relationship in RPT has yet to be prioritized [37]. Also, for normal tissues, dose limits are only known for a few combinations of organs and radiopharmaceuticals. In a recent review summarizing the current state of radiation dosimetry in RPT, it is evident that more is known for external beam radiotherapy (EBRT) than for RPT [36]. Early reporting of radiation toxicity from EBRT was influenced by the percentage of the organ irradiated, where, for example, one third of the liver or a part of the kidney could be irradiated to a higher absorbed dose without any radiation toxicity than would be the case for whole-organ irradiation [38]. These data were updated and expanded through the Quantitative Analysis of Normal Tissue Effects in the Clinic (QUANTEC) [39]. Thus, it is increasingly clear from clinical studies in RPT that the absorbed dose limits derived for EBRT do not predict radiation toxicity from radiopharmaceuticals. Therefore, radiopharmaceutical-specific dose-limits are required [36].

The biological effect (described in more detail in chapter 4) of radiopharmaceutical therapy is intrinsically based on the energy deposition within the tissue, as is the case in EBRT. Some critical differences between the absorbed dose delivery between RPT and EBRT make it hard to extrapolate from one discipline to another. Some fundamental differences include [36]:

- Radiopharmaceutical therapy is a systemic therapy where pharmacokinetics give rise to time-varying radiopharmaceutical residence times in different parts of the body (systemic domain)
- Radiopharmaceutical therapy gives rise to spatial nonuniformity of energy deposition, which, depending on radiation quality, can give rise to nonuniform absorbed doses (spatial domain)
- Radiopharmaceutical therapy is often given with a low absorbed dose rate, and radionuclide decay give rise to time variations in the absorbed dose rate (temporal domain)

The pharmacokinetic domain describes the systemic transport of radiopharmaceuticals through the body after administration. Spatial nonuniformity may arise due to heterogeneity in the expression of the molecular target in the region of risk (*e.g.*, SSTR2 expression) or due to the physiologic transport of the radiopharmaceutical through the liver or kidneys, where physiological regions of the organs are nonuniformly exposed. Variations in the temporal domain of absorbed dose delivery (the absorbed dose rate), arise due to the radiopharmaceutical's physical decay and biological elimination. These effects are interlinked, making partial organ irradiation, as possible in EBRT, typically not obtainable in RPT.

Radiopharmaceutical therapies use effective targeting agents, where a substantial fraction of the administered activity is retained in the target region. However, irradiation of healthy tissues is inevitable, and depending on the targeting agent, undesired high retention within normal tissues has been identified. Regions at risk in RPT are irradiated due to specific uptake of the radiopharmaceutical or the organ's physiological excretory functions, such as in the kidneys and liver. Colloids and antibodies accumulate in the liver [40-42]. In contrast, smaller molecules, such as peptides, have a longer retention time within the kidneys [16, 30].

Blood

After intravenous administration of radiopharmaceuticals, the blood is the first compartment exposed to radiation. The major determinant of absorbed dose to haematopoietic cells are the radiopharmaceuticals circulating through the bone marrow. For radiopharmaceuticals targeting SSTR, specific targeting of activated leucocytes and monocytes may also contribute [43]. Biomarkers indicating DNA damage, such as γ H2AX and 53BP1, have been found to have elevated levels in peripheral blood lymphocytes after ^{177}Lu -PRRT [44, 45].

Liver

Published data on the activity distribution within the liver is thoroughly listed in **Paper I** [46] and is briefly listed here. Quantitative autoradiography has demonstrated nonhomogeneous uptake of different ^{111}In -labelled radiopharmaceuticals and $^{99\text{m}}\text{Tc}$ -colloids [42, 47, 48]. The uptake has been associated with uptake via phagocytizing

Kupffer cells, creating radioactive hotspots within the tissue, and hence receiving a self-absorbed dose up to 15000-fold greater than the estimated mean absorbed dose to liver tissue [49]. For radioimmunotherapies (RIT), where radionuclides are labelled with an antibody, the liver uptake is often high. This is perhaps due to cross-reactivity of antibodies with normal liver tissues, binding of the antibody to constant fragment (Fc)-receptors on normal liver tissue, and possible interaction between the administered antibody with circulating antigens, forming immune complexes that are sequestered by the liver [40].

Kidney

The activity uptake in kidneys in PRRT is known to be non-uniform, as de Jong *et al.* [50] demonstrated through autoradiography of a histological section of the kidney after administration of ^{111}In -DTPA-Octreotide. Kidney accumulation arises from re-absorption of the radiopeptide in the proximal tubular and the resulting unspecific retention in the interstitial space [30]. Furthermore, depending on the radionuclide, the uptake pattern can translate into an inhomogeneously-absorbed dose distribution, as shown in a study by Konijnenberg *et al.* [51]. The activity distribution derived in de Jong *et al.* was used to simulate radiation transport from the uptake of ^{111}In , ^{90}Y and ^{177}Lu . The absorbed dose distribution for the low energy beta emitter ^{177}Lu and the low energy conversion electron and Auger-electron emitter ^{111}In produced absorbed dose distributions dependent on the activity distribution.

Testis

Studies of rodent testes have demonstrated nonuniform activity uptake after intravenous administration. After administration of ^{111}In -chloride highly heterogeneous distribution of was shown in the multilevel autoradiography studies by Jönsson *et al.* [47, 52, 53]. Uptake was located in the interstitial tissue and the spermatogonia, considered the most radiosensitive cells in adult humans [54, 55].

2.3.1.4 Dose limiting organs

The uptake mechanisms and micro-distribution of radiopharmaceuticals in normal tissues and regions at risk after administration have, for different treatments, defined dose-limiting organs, such as the kidneys [30], the bone marrow [16], the liver [56] and/or the testes [41]. Hence, absorbed dose calculations to non-target areas are of high importance. Accordingly, a 'balancing act' emerges, where absorbed doses to regions at risk must be below a certain threshold to avoid severely deterministic side effects. At the same time, the absorbed dose to the tumour must be sufficient for the treatment to be successful. Even though the absorbed dose limits to normal tissues depend on absorbed dose rate, radiation quality, tissue type, and the time between treatments, it is often practical to present the limit in units of absorbed dose for a specific treatment schedule and radiopharmaceutical.

Strigari *et al.* [56] evaluated normal tissue complication probability after SIRT and found a 50% probability of severe liver toxicity at a biologically-effective dose (BED) of 93 Gy_{BED}, averaged over the entire liver volume, corresponding to a mean liver dose of 52 Gy; a value higher than the absorbed dose of 40 Gy for a 50% probability of liver failure after whole liver external irradiation presented by Emami *et al.* [38] This indicates that absorbed doses in microsphere treatments need to be interpreted differently than external beam-absorbed doses, most probably due to the nonuniformity in the microscale distribution throughout the hepatic arterial system [36]. For RITs, where radionuclides are labelled with an antibody, the uptake pattern is different than for SIRT. In a study published by Wahl *et al.* [57], the maximum tolerable dose (MTD) after RIT using the radiopharmaceutical ⁹⁰Y ibritumomab tiuxetan (Zevalin®) was found to exceed 28 Gy. Still, the MTD was not reached due to discontinuation of the drug's availability.

The kidney is generally considered to be the dose-limiting organ in therapy with [¹⁷⁷Lu]Lu-SSRT [16, 43]. The kidney tolerance absorbed dose of 23 Gy, derived from experience in EBRT, has been suggested for renally-excreted radiopharmaceuticals [38]. To reduce the risk of kidney toxicity, co-administration of amino acids is performed during the infusion and the first few hours afterwards. Amino acids introduce a competitive inhibition of reabsorption to proximal tubular cells, which have reduced the dose absorbed by the kidney by up to 50 % [36]. Experience from modern RPT with peptides and small molecules, summarized by Wahl *et al.*, [36], indicates that the tolerance limit for kidneys is higher than the 23 Gy tolerance limit adapted from EBRT, and that adoption of this level may result in underdosing target regions.

When a radiopharmaceutical primarily localizes within tissue substructures of an organ, absorbed dose estimations at the whole-organ level become insufficient, and the relationship between absorbed dose and biological effect might be impossible to establish from patient data. Hence, today's radionuclide therapies may require a modified formulation of the absorbed dose determination where the heterogeneous distribution of the radiopharmaceuticals in the tissue—either intended or unintended—is considered.

3 MIRD-based internal dosimetry

Internal dosimetry is a method for indirect assessment of absorbed dose to a region, that could be an organ or part of an organ, from radionuclides or radiopharmaceuticals deposited within the body. The rationale of internal dosimetry is that the absorbed dose to an organ or sub-organ, or a related quantity thereof, can relate to a biological effect observed within the organ or be used in radiation protection to express population risk of a stochastic induction cancer or non-cancer diseases.

3.1 Fundamental quantities

The fundamental quantity of radiation dosimetry is defined by the ICRU as the energy imparted, ε , to matter in a given volume [58]

$$\varepsilon = \sum_i \varepsilon_i \quad (3.1)$$

where each energy deposit, ε_i , is the energy deposited in a single interaction expressed in joule (J) or electronvolt (eV). The summation of energy deposits to the energy imparted in the volume of interest can be done for one or more energy deposition events. Each energy deposited, ε_i , can be expressed as follows:

$$\varepsilon_i = \varepsilon_{in} - \varepsilon_{out} + Q \quad (3.2)$$

Where ε_{in} and ε_{out} are the stochastic quantities describing the energy of the incident particle, excluding rest energy, and the energy of all ionizing particles leaving the interaction, excluding their rest energies. Q is the change in rest-mass energy of the nucleus and all particles involved in the interaction, *i.e.* $Q > 0$ implies a reduction of rest mass energy and $Q < 0$ implies an increase of rest-mass energy.

The mean energy imparted, $\bar{\varepsilon}$, *i.e.* the expectation value of the stochastic quantity ε , to the matter of interest with the mass m in the volume V is defined in Eq. 3.3. The mean energy imparted equals the mean radiant energy, R_{in} , of all charged and non-charged particles that enter V , minus the mean radiant energy, R_{out} , that leaves V , plus the mean sum, $\sum Q$, of all changes of the rest energy that occur within V [58]:

$$\bar{\epsilon} = R_{in} - R_{out} + \sum Q \quad (3.3)$$

The absorbed dose, D , based on the expectation value of the energy imparted, $\bar{\epsilon}$, to the matter in the volume V , with the mass m , has the unit joule per kilogram, with the special name gray [Gy] and can be expressed as follows:

$$D = \frac{d\bar{\epsilon}}{dm} \quad (3.4)$$

3.2 MIRD formalism

The most widely-adopted mathematical scheme for estimating absorbed doses within diagnostic and therapeutic nuclear medicine is the MIRD formalism, with the latest standardization of nomenclature defined in MIRD pamphlet No. 21 [59]. Two region types need to be determined for practical implementation of dosimetry in nuclear medicine: the source region and the target region. A source region is a spatial region where the radioactive source is located, and the target regions are the regions of interest for the determination of the absorbed dose.

The expressions derived for the calculation of absorbed dose to a target region, r_T , is based on an expression consisting of two main factors; the first describing the uptake and retention of activity within the source region, r_S , and the second describing the fraction of energy absorbed in r_T from emissions occurring from r_S . Thus, implied in this assumption is that the defined regions, r_T and r_S , are homogenous concerning both material composition, density, and activity distribution. For RPTs with relative short half-lives, organ sizes and body geometry can often be treated as “static” over the period of irradiation, thus reducing the MIRD-formalism to a time-invariant equation. Hence, the mean absorbed dose, D , to r_T can be calculated according to Eq. 3.5:

$$D_{r_T} = \int_0^{\infty} \sum_{r_S} A_{r_S}(t) \cdot S(r_T \leftarrow r_S) dt = \sum_{r_S} \tilde{A}_{r_S} \cdot S(r_T \leftarrow r_S) \quad (3.5)$$

where $A_{r_S}(t)$ is the activity in the source region at time t after administration and $S(r_T \leftarrow r_S)$, denoted the S value, representing the mean absorbed dose per time-integrated activity (previously denoted cumulated activity), \tilde{A}_{r_S} ; *i.e.*, the number of decays taking place within the source region for a certain period of time. The absorbed dose rate per unit activity denoted S value is given by:

$$S(r_T \leftarrow r_S) = \frac{\Delta \cdot \phi(r_T \leftarrow r_S)}{m(r_T)} = \Delta \cdot \Phi(r_T \leftarrow r_S) \quad (3.6)$$

where (Δ), the mean energy emitted per nuclear transformation is multiplied by the fraction of the radiation energy emitted from r_S that is absorbed in r_T , denoted the absorbed fraction, $\phi(r_T \leftarrow r_S)$ and divided by the mass of the target region m_{r_T} . Alternatively, the S value can be expressed as the specific absorbed fraction $\Phi(r_T \leftarrow r_S)$ in (kg^{-1}) times the emitted energy (Δ). The S value is usually expressed in units of $mGy MBq^{-1} s^{-1}$.

The contributions of absorbed dose to a target region can be divided into two parts: (i) self-absorbed dose, the absorbed dose due to the energy emitted and absorbed in the source region itself ($r_T = r_S$), and (ii) cross-dose, the absorbed dose due to energy absorption from the energy emitted from surrounding sources ($r_T \neq r_S$).

In practical applications of internal dosimetry, both the time-integrated activity curve of the source region and the S value need to be determined. The S value is specific to the radionuclide and the specific geometrical model defining the spatial relationship and tissue compositions of the source and the target regions. The sum of all products of time-integrated activity and S values across all source regions contributing to absorbed doses within the target region, giving the total absorbed dose to the target.

The *a priori* MIRd S values have been published for different spatial geometries, ranging from whole-body organ level (based on, among others, the Cristy–Eckerman whole body phantoms [11] and the ICRP/ICRU reference phantoms [60] with S values presented in the Internal Dose Assessment by Computer (IDAC Dose 2.1) software [61]) to tissue micro-architecture levels [62–64] to the cellular level [65]. The latter can be used if the number of decays within different cellular compartments is known, either from measurements or biokinetic models. These S values make it possible to calculate the absorbed dose to, for example, the cell nucleus from sources distributed either on the cell surface, in the cytoplasm, or in the nucleus itself. The general MIRd formalism is independent of the size of the defined source or the target region. Thus defining—or using a predefined source or target region of dimensions larger than the actual relevant target region, such as by calculating the mean absorbed dose to the whole organ when in reality the activity is localized only to some specific cells—can make the dosimetry calculation an inadequate predictor of its biological effect [66].

3.2.1 Small-scale dosimetry

In conventional dosimetry on the macroscopic scale, the absorbed dose is determined for volumes representing organs or parts of organs, such as organ content versus organ wall or bone surface versus bone marrow. These volumes are in the MIRd-formalism defined as homogenous concerning material composition, density, and activity distribution, creating a convenient way of calculating mean absorbed doses. This macroscopic approach is often used when scintillation camera images are the basis for quantification of activity uptake for some time points after administration. The resolution obtainable with clinical imaging systems is limited, leading to an underestimation of the possible non-uniformity of the activity distribution and the colocalization of activity to the functional units of the organ. It will, for example, not be evident if a radiopharmaceutical is associated with the bone surface, the bone matrix, or the bone marrow [48]; and for low energy beta- and Auger-electron-emitters, this could give rise to a non-homogeneous absorbed dose distribution, and the average organ-absorbed dose will not represent the actual absorbed dose pattern.

Thus, the development of dosimetry models taking the functional units of the organ and the non-uniformity of the activity distribution into account is necessary for a better understanding of the absorbed dose as a predictor of a biological effect. This is possible to achieve without abandoning the general concept of MIRd formalism if conventional organs are replaced by organ subregions, for which the assumptions of homogeneous activity distribution and material composition still hold [66]. One approach is so-called “small-scale dosimetry”. Although not precisely defined, this term refers to dosimetry models where the dimensions of the source and target regions are the same, or even less than, the range of charged particles emitted from a radionuclide; *i.e.* the absorbed fraction cannot be considered to be one [48, 67]. Hence, the electron cross-dose from adjacent regions cannot be neglected, which puts even harder constraints on the geometry and the transport of charged particles throughout the geometry to be calculated or modelled in a realistic way. Figure 3.1 illustrates the absorbed fraction as a function of source region radii for monoenergetic photons and electrons.

Small-scale dosimetry models based on the architecture of differentiated tissue have been published for some organs at risk, such as the testes [64], small intestine [63, 68], kidney [62], bone marrow [69], liver (as part of my research (**Paper I**) [46], and in Gulec et al. [70]). In a small-scale dosimetry model, it is possible to calculate absorbed doses, absorbed fractions and generate S values for various source-target microstructure regions, which can be used to obtain absorbed dose calculations for the defined structures.

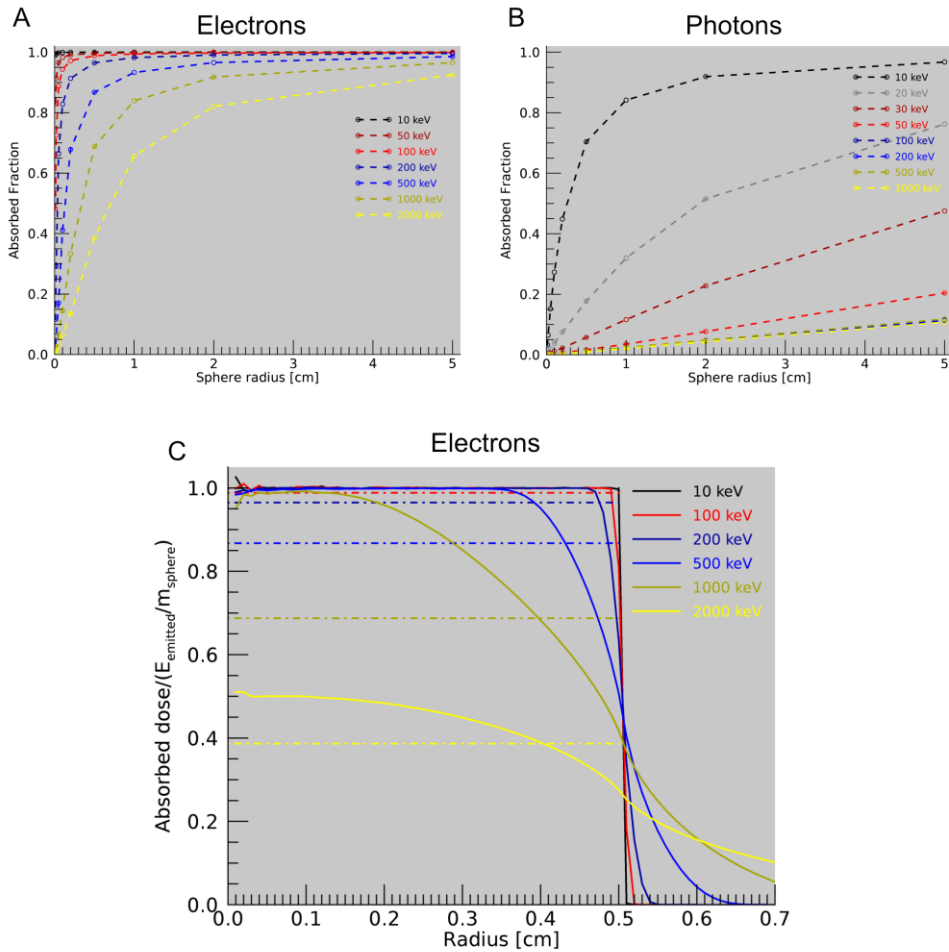


Figure 3.1. Self-absorbed fractions for monoenergetic electrons (A) and photons (B) for uniform tissue-equivalent spheres with different radii. Sub-figure (C) shows the absorbed dose per emitted energy and mass for a sphere with a radius of 5 mm and uniform activity distribution and mono-energetic electrons with different energies. The unit on the y-axis is mathematically equivalent to the absorbed fraction. The solid lines represent the absorbed dose at different distances from the origin, whereas the dashed lines represent the "average absorbed fraction". The figure illustrates the necessity in small-scale-dosimetry models of assessing an absorbed fraction for electrons that is less than one. In courtesy of Erik Larsson.

3.3 Realistic digital phantoms

In internal radiopharmaceutical dosimetry, a digital phantom is a mathematical representation of a 3D object, where an organ's size, shape, and location are defined. The primary development has been in human models, but interest has also been attracted to small-animal models in pre-clinical research [71, 72]. The first human phantoms, just like the small-scale models of today, were primarily described by standard geometrical equations for planes, spheres, and cylinders, and were mainly used to calculate absorbed fractions and S values [73]. However, human anatomy is not realistically described by these phantoms, which limits the accuracy of these calculations. The subsequent introduction of voxel phantoms, segmented from tomographic CT or MRI images, reduced this drawback and has been used for nuclear medicine imaging research and radiation protection dosimetry. Among the most widely-used voxel phantoms is the Zubal phantom [74], the Adult Reference Computational Phantoms compiled by the ICRP [75] and the University of Florida's family of voxel phantoms [76].

The third generation of digital phantoms was developed around the year 2000. They were characterized by fitting smooth surfaces to the segmented volumes of voxel phantoms, either via polygonal meshes or using non-uniform rational b-splines (NURBS). This overcame the limitation of the fixed geometry of the voxel phantoms, as the size and position of the organs in a NURBS phantom can be modified, and simulation of breathing and cardiac motion can be introduced. Among these, the most widely-used are the XCAT phantoms [77], which today are considered state-of-the-art of digital phantoms, consisting of a population of phantoms of different ages, weights, and lengths [78], also including paediatric phantoms [79]. Furthermore, surface-based small-animal phantoms were developed, such as the mouse phantom MOBY [72]. The phantom design allows for modification of organ size and location. Execution of the Moby program generates a three-dimensional voxel-based phantom of specified size, which can be used as input for Monte Carlo simulations. In Larsson et al. [80] the Moby phantom was used to generate absorbed fractions and S values for mice organs. In this thesis, this work further was developed to match the mice population used in **Paper II**.

3.4 The Monte Carlo method

Monte Carlo methods are used to solve problems involving statistical processes and have become a valuable and vital tool in medical physics due to the stochastic nature of radiation emission, transport, and detection. The computerized Monte Carlo technique was first developed and applied within the Manhattan Project at Los Alamos National Laboratory, for calculations of neutron interactions during the development of the atomic bomb [81].

The Monte Carlo method is applied to solve physical problems where analytical approaches are not applicable. Within medical physics, Monte Carlo methods have mainly been used for studies of radiation transport; either for dosimetry purposes or to evaluate imaging techniques. In **Paper I**, the Monte Carlo method has been used for dosimetry purposes to calculate the distribution of energy depositions from photons and charged particles emitted from radioactive sources interacting within a small-scale anatomical model of liver tissue [46].

The Monte Carlo method is based on the theory that physical processes, such as the interaction between radiation and matter, can be described by statistical probability density functions (PDFs). Using pseudo-random numbers and physically accurate sampling rules, sampling the PDFs will determine the outcome at each step of the process. The full particle track, associated with a particle's full movements through the specified geometry, and the tracks from potentially new particles created in an interaction between the first particle and the medium, is called a "history". In an entire history, the final particle tracks depend on the cross-sections for different interactions associated with the particle type, its energy, and the medium it is traversing. Repeat these steps and an estimate of the desired parameter—one that converges towards the true solution—can be obtained [81].

Described above is the direct Monte Carlo simulation method, using true probability functions. Different variance reduction methods can be applied to avoid unacceptable long computation times to produce statistically relevant results. Examples of variance reduction can be forced or directed interaction instead of the isotropic emission of particles. One of the more straightforward methods, which can be regarded as a variance reduction method, is using an energy cut-off under which particles are considered locally absorbed. No additional computer time is spent following the particles, and more histories can be run. The variance reduction methods bias the results obtained from a non-direct Monte Carlo simulation, and the result must then be corrected.

The accuracy of the value of a parameter derived via Monte Carlo methods is, in theory, exact if the number of histories derived is infinite. However, its accuracy will still depend on the accuracy of the probability density functions used to describe the physical processes, the model used to describe the system, the quality of the random pseudo-random numbers used to sample the location, energy, and emission direction of the emitted and detected particles, and the number of histories run within the simulation. Even if the system studied could be perfectly described, simplifications and approximations of the system are often required for computation time to be realistic [82].

3.4.1 Radiation transport

3.4.1.1 Photon interactions

Photons interact with matter in a way that results in quite a few interactions and a long mean-free path. A photon interaction with matter will lead to a partial or total energy transfer of the photon energy to electrons within the matter, leading to either a disappearance of the incident photon or scatter at a significant angle with an associated energy loss.

Within the studied energy range, photons interact with matter in four different ways, each way with an associated cross-section dependent on the photon energy and the material it crosses. The four interaction possibilities are the photoelectric effect (τ), coherent scattering (σ_{coh}), incoherent scatter (Compton scatter) ($\sigma_{compton}$) and pair production (κ). The total linear attenuation coefficient (μ) is given by the sum of the four cross-sections:

$$\mu = (\tau) + (\sigma_{coh}) + (\sigma_{compton}) + (\kappa) \quad (3.7)$$

The photoelectric effect explains the full absorption of the incident photon, resulting in the emission of fluorescent photons and/or emission of an Auger electron. Using a photon/electron transport mode, the created particles are stored, enabling the creation of particle tracks of the emitted particles, followed by further tracking of the created particles. Detailed physics treatment includes the coherent scattering and characteristic x-rays that occur after the photoelectric effect.

A photon undergoing Compton scattering undergoes an inelastic scattering against an orbital electron. It results in a deflection of the incident photon and a transfer of momentum to the recoiling electron. The scattering angle and the new energy of the photon, as well as the recoil energy of the electron need to be determined. The energy distribution between the deflected photon and the recoiled electron is calculated using the Klein-Nishina differential cross-section formulation of the Compton angles [83]. For coherent scattering, or scattering without any energy loss, only the scattering angle is calculated, since no recoiling electrons will be produced in the interaction.

3.4.1.2 Electron interactions

The interaction properties of charged particles, compared to the interaction of photons, are fundamentally different and result in a large number of low energy loss interactions. Therefore, the simulation of electrons is much more complex and time-consuming. The dominant interaction is inelastic scatter against atomic electrons, resulting in low energy loss and a small angular deflection. A lot of analytical and semi-analytical methods have been developed for calculating the transport of charged particles. Electron transport is often modelled to reach reasonable computation times using condensed history, where the cumulated effect of many interactions is treated in a

single step. Often a mixed approach is applied, where inelastic interactions are simulated individually, and elastic interactions are grouped and sampled from a multi-scattering approach.

3.4.2 The MCNP code

In **Paper I** the general-purpose Monte Carlo N-Particle code (MCNP) was used (version MCNP5 1.6), together with the parallel developed MCNPX 2.7 [82, 84]. The code package was chosen partly due to long experience in the department of the code combined with the fact that both photons, electrons (with MCNP5) and alpha particles (with MCNPX) could be simulated within the codes without major programming requirements. The MCNP can be used in several transport modes: electron only, photon only, neutron only, electron/photon, and other combinations.

The MCNP code is controlled with input files written in FORTRAN 90 standard. These input files include a block describing the analytical surfaces used to create the geometry, where the geometry compartments are referred to as cells. The second block is written to describe the cells, made up of a specific combination of previously-defined surfaces and their associated material and density. Hence, a material block needs to be included, specifying the atomic composition of the used materials and what cross-section table to use. For the Monte Carlo calculation to be carried out, the defined geometry needs to be supplemented with a source specification card containing a definition of source particle type and energy, and the source's position, distribution, and emission direction. The detection of specific properties, such as energy deposited or particle flux, within the defined cells of the geometry is performed using tallies. A tally works like a detector designed to score the specified data of interest and is placed at a specific point within the geometry.

3.4.3 The EGS4 code

In **Paper IV** the general-purpose electron gamma shower (EGS4) code [85] with parameter-reduced electron-step transport algorithm for electrons (PRESTA [86]) was used to calculate absorbed dose-rate maps from SPECT-images. The PRESTA algorithm switches from multiple scattering to single scattering when electrons are close to boundary crossings, thereby minimising step-size artefacts occurring close to boundaries.

3.5 A small-scale dosimetry model of the liver tissue

In **Paper I**, the Monte Carlo method was applied to calculate S values for several source-target configurations in liver tissue. The geometry created for the human liver small-scale anatomical model was based on a simplification of the functional subunit

(FSU) of the liver; the hexagonal hepatic lobule. The geometry is defined by the first and second degree of analytical surface equations, where each region will have its identification number, making each sub-region identifiable as a source- and/or target region. The hepatic lobule was modelled as a hexagonal prism. Within this hexagonal prism, different liver microarchitecture structures such as hepatocytes, sinusoids, bile canaliculi, spaces of Disse (the space between the hepatocytes and endothelial cells of the sinusoid), Kupffer cells, central veins, portal veins, portal arteries, and the bile duct, were all defined. The model was defined inside a sphere with a radius of 7.3 cm to mimic average liver mass. All defined hepatic components can be chosen as the source or target region. Still, the space of Disse is of special interest as a target region, since it may represent the endothelial cells surrounding the sinusoids, the presumptive target for fatal radiation damage to the liver [87].

Dimensions of each defined structure within the liver microarchitecture were collected from an extensive search of the literature and are presented in detail in **Paper I**. An illustration of the model with its components and dimensions can be found in Figure 3.2.

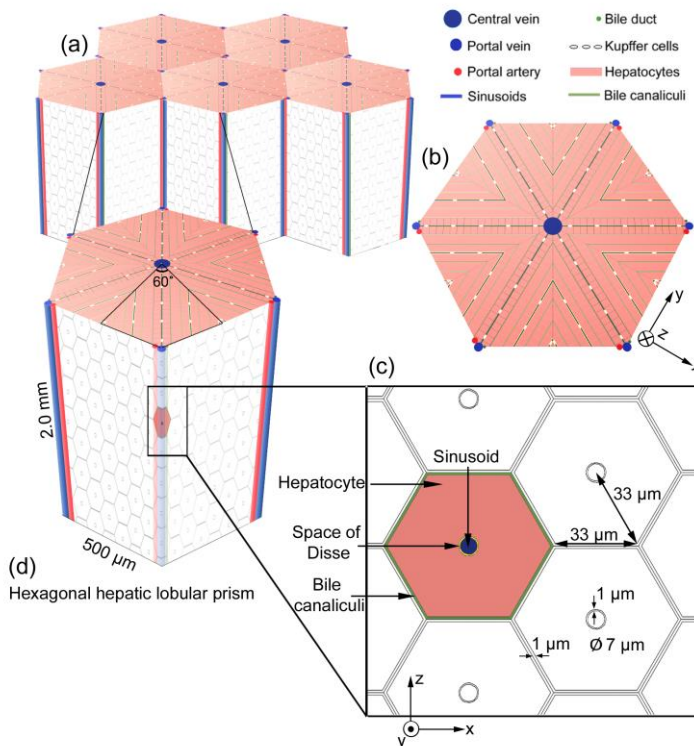


Figure 3.2. The geometry of the small-scale anatomical model of the liver. (a) Illustrates the orientation and organization of the hexagonal lobular prisms. (b) Illustrates the geometry of the vessel and the bile canaliculi within one liver lobule, with the central vein in the centre and one portal artery, one portal vein, and one bile duct in each corner of the lobule. The Kupffer cells are distributed within the sinusoids. (c) Illustrates the organisation and dimensions of cells and structures within the liver lobule. (d) Illustrates the dimension of the hexagonal liver prism.

The deposited energy was tallied over all defined structures in the small-scale anatomical model of the liver tissue with the MCNP energy deposition tally. Tracks of different particle types emitted from the same radionuclide were simulated separately, and the resulting energies were then summed and scaled by their respective yields. The simulation of electron tracks was as detailed as possible, performed by maximizing the number of electron sub-steps per energy step, which implies using the shortest step length possible in the electron transport. The mass of each target region was determined, and the absorbed fractions, specific absorbed fractions, and S-values were obtained.

Calculations were performed for some radionuclides of interest to liver dosimetry, including ^{18}F , ^{90}Y , $^{99\text{m}}\text{Tc}$, ^{111}In , ^{125}I , ^{131}I , ^{177}Lu , and ^{211}At (including its daughter ^{211}Po , $T_{1/2} = 0.52$ s). The absorbed energy from monoenergetic particles was tallied for electron energies of 5–2000 keV, photon energies of 5–200 keV, and alpha particle energies of 3–10 MeV.

The energies and yields of the radionuclides used in the Monte Carlo simulation in this work were obtained using the Radiation Decay 3 software package (Charles Hacker, Griffith University, Gold Coast, Australia), which is based on data from the Radiation Shielding Information Center at Oak Ridge National Laboratories (TN, USA). The beta particle energy spectra were obtained from the National Nuclear Data Centre at Brookhaven National Laboratory (Upton, NY, USA).

The model illustrated cases where average absorbed dose to the whole organ may not be a good predictor of the resulting biological effect. For heterogeneous activity distributions, for example uptake in Kupffer cells of radionuclides emitting low-energy electrons (^{125}I) or high-LET alpha particles (^{211}At) the target absorbed dose for the part of the space of Disse, closest to the source, was more than eight- and five-fold the average absorbed dose to the liver, respectively, as illustrated via the cumulative absorbed dose-ratio histograms in figure 3.3.

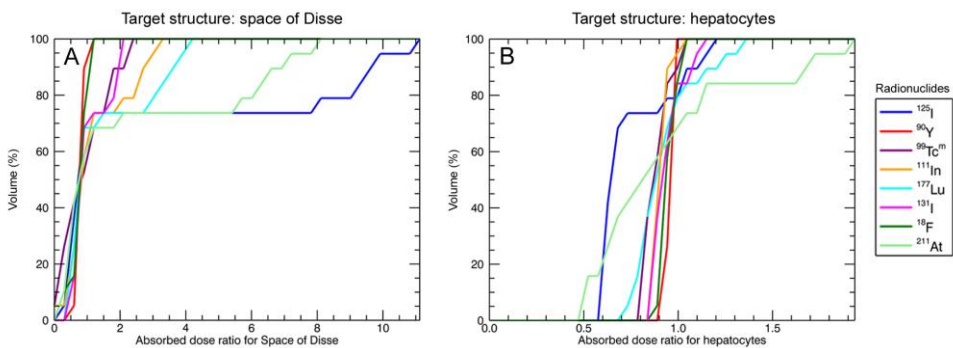


Figure 3.3. Cumulative absorbed dose–ratio volume histogram of the target structures space of Disse (A) and hepatocytes (B) for activity localized in all the Kupffer cells in the model geometry. The dose-ratio volume histograms show the volume percentage of the two different hepatic microstructures having a given dose ratio or lower, where the dose ratio is indicated as the average absorbed dose of the target region to the average absorbed dose to the liver.

4 Radiobiology in nuclear medicine

Radiobiology concerns the biological effects of radiation on living organisms, organs, tissues or cells, and this thesis explicitly discusses the biological effects of ionizing radiation. When ionizing radiation interacts with biological matter, energy from the radiation is deposited within the material, and chemical bonds are broken. Radiobiology is the study of these interactions at the atomic and molecular scale, as well as their induced effect and biological outcome on cells, tissues, and organs. Ionizing radiation may lead to genetic modifications in exposed normal cells surviving initial exposure but may also lead to loss of clonogenic tumour cell survival. This is the dual nature of ionizing radiation in a therapeutic setting.

4.1 Classical radiobiology

The interaction of ionizing radiation on a biological system generates a sequence of events that span from fractions of seconds up to years. These processes can, at the simplest level, be divided into three phases: physical, chemical and biological [88]. The physical phase includes the deposition of radiation energy in electronic states, primary ionizations, excitations, and the following transition of excited states into lower electronic states. This happens on a time scale of 10^{-18} s to 10^{-14} s. The chemical phase describes the rapid interaction of the ionized atoms and molecules with other cellular components. Recombination of ion pairs or an independent molecular species with an unpaired electron in an atomic orbit—called a “free radical”—may persist. Free radicals can attack macromolecules by either donating or accepting an electron. The free radical reactions are complete within 1 ms of radiation exposure. The biological phase ranges on a time scale from 1 s up to years after irradiation. It includes all subsequent processes, from enzymatic sensing and signalling at the site of the chemical damage, the potential damage repair or eventual cell killing, up to late effects and tissue damage [88].

The ionizations occurring in the physical phase after irradiation can be direct or indirect in relation to the target molecule. In classical radiobiology, DNA is considered the target molecule mainly responsible for the biological outcome of irradiation. Still, damage to other structures, such as proteins, lipids, and metabolites, may also play an important role [89]. In direct action, the macromolecule is ionized by the radiation itself, whereas indirect ionization occurs through reactive oxygen species (ROS)

produced by hydrolysis. Despite their short existence, it is approximated that free radicals can diffuse a distance of double the diameter of the DNA helix, and thus results in damage away from initial site of ionization. For low LET radiation, it is estimated that two-thirds of the DNA damage is caused by hydroxyl radicals [89].

4.1.1 DNA damage and response

DNA damage incidence is considered proportional to the absorbed dose and is often quantified per unit of absorbed dose per cell. A wide range of DNA lesions can be produced, including single-strand breaks (SSB)—*i.e.* one of the DNA strands is affected but the other stays intact—double-strand breaks (DSB)—*i.e.* both DNA strands are affected—and DNA base lesions. According to a review from Pouget *et al.* [90], the most abundant DNA damage after irradiation with low LET radiation is the DNA base lesion (1000/cell/Gy), whereas about 40 double strand breaks (DSBs) are formed per Gy per cell.

Although the frequency of DSBs is relatively low, the probability of cell death or induction of mutations is high. If unrepaired, it is considered a lethal event for the cell through chromosomal aberrations or loss of genetic material [90]. Also, if incorrectly repaired (misrepair) damage can reside and manifest as a mutation or lead to cell death [91], as illustrated in the schematics in Figure 4.1.

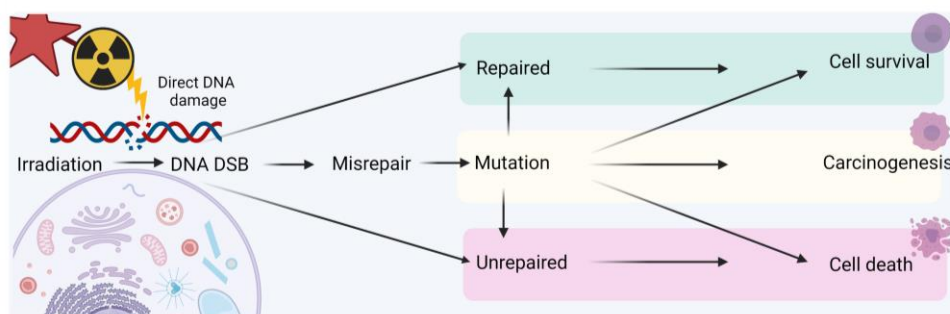
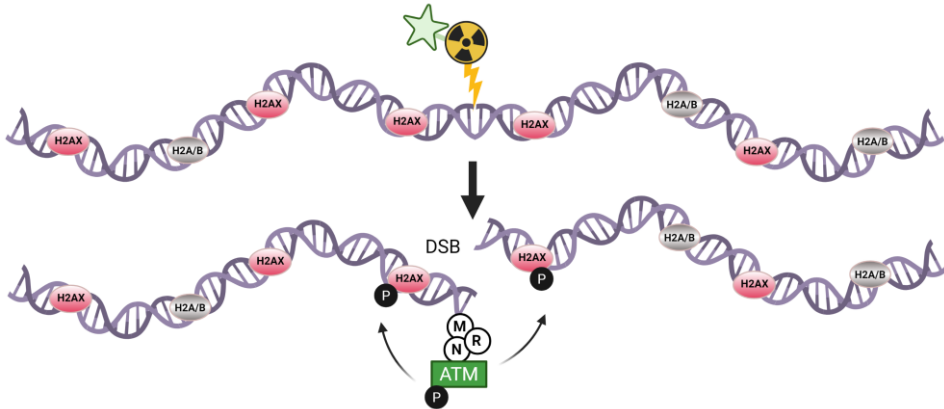


Figure 4.1. A schematic illustration of the standard model of DNA damage response to ionizing radiation, showing the induction of a DNA DSB and its downstream biological consequences, which can lead to repair, misrepair, or non-repair. If the DNA is not repaired, there is a high probability of cell death. In contrast, if the DNA is misrepaired there is a probability of mutation, which can lead to carcinogenesis. Picture inspired by Prise *et al.* [91], created with BioRender.com.

The DNA damage response is a highly complex but ordered process that determines the cellular outcome after the induction of DNA damage caused by ionizing radiation. The damage response is not a single pathway but a group of interrelated signalling pathways, which can be divided into DNA damage sensors and DNA damage effectors. The sensors consist of a group of proteins that actively monitor DNA, searching for damages. If damage is detected, these proteins can signal to the three main effector pathways: the programmed cell death pathway; the DNA repair pathway; or the pathway causing temporary or permanent blocking of the cell cycle, which will determine the outcome for the cell. The blocking of irradiated cells in cell cycle checkpoints is a powerful response, allowing cells to halt cell cycle propagation, allowing the cell to repair DNA damage. After repair, the arrest is released, and cells can continue throughout the cell cycle [88].

The mechanism of DNA repair depends on the complexity of the DNA damage. Base damages are repaired via one of the excision-resynthesis pathways: base excision repair (BER); nucleotide excision repair (NER); or mismatch repair (MM), where a part of the DNA strand is removed and replaced by DNA synthesis, using the undamaged DNA strand as a template. The half-time of repair is around 5–10 min [92]. Direct SSBs are repaired via the single strand break repair (SSBR) pathway, where poly-ADP-ribose polymerase (PARP1 or PARP2) is required for its detection. Repair is performed via either the short (single-base/nucleotide) or long (removal of a larger DNA segment) path, and repair half-time is around 10–20 min [92]. DNA DSBs are repaired by one of two main pathways: non-homologous end-joining (NHEJ) or homologous recombination (HR). NHEJ is active throughout the cell cycle and joins two DNA DSB end together without requiring homologous DNA sequences. The process is more rapid than HR but less accurate, since HR uses homologous undamaged DNA as the template for repair, whereas HR is only active in the S- and G2-phase, when a sister chromatid is present [88]. The half-time of DSB repair is above 50 min [92].

The DNA damage response to DSBs has been extensively studied in recent years. One of the earliest events known to occur in the repair process is the phosphorylation of the histone protein H2AX, a variant of the H2A histone and a component of the core nucleosome structure in which the DNA is packed. Starting within a few minutes after the DSB formation, the sensor proteins, including the MRN-complex (MRE11, RAD50 and NBS1), recruit the ataxia telangiectasia mutated (ATM) protein which phosphorylates the H2AX in a region around the site of the unrepaired DSBs, called a focus (*pl. foci*). The phosphorylated form, denoted “ γ -H2AX”, is necessary to recruit other proteins involved in the repair process [88]. Figure 4.2 illustrates the first steps in the damage response to a DNA DSB and the formation of γ -H2AX foci.



Figur 4.2. Illustration of the formation of γ -H2AX foci and its role in the DNA damage response to DSB, a hierarchical process starting with the recognition of the DSB by the MRN (MRE11-RAD50-NBS1) complex, followed by recruitment of the ataxia telangiectasia mutated (ATM) kinase and its autophosphorylation at the DSB site. The resulting ATM-mediated phosphorylation of H2AX leads to the formation of γ -H2AX. Illustration created with BioRender.com.

4.1.2 Cell death and radiobiological modelling

Cell death after irradiation can occur in several ways. The most common definition of cell death is the loss of proliferative capability. In most cases, cells die after attempting mitosis via a so-called “mitotic catastrophe”. Other cell death endpoints are apoptosis (genetically programmed cell death), autophagy (self-engulfment of cytoplasmic components), necrosis (loss of cell membrane integrity), or senescence (permanent cell-cycle arrest) [13, 88]. Different assays exist to quantify clonogenic cell survival after irradiation, during which the surviving fraction (SF) of cells is determined.

This section describes the most widely used mathematical model developed to describe cell survival as a function of the absorbed dose, the linear-quadratic (LQ) model [88]. It has proven useful in describing both experimental and clinical cell survival data [93]. The most common expression of the LQ model describes the survival fraction of a cell following exposure to a single absorbed dose D :

$$SF = e^{-(\alpha D + \beta D^2)} \quad (4.1)$$

where α and β are parameters describing the rate of induction of cell lesions, increasing linearly and quadratically with the absorbed dose. The LQ model shows a ‘shouldered’ absorbed dose response, where the initial region is dominated by the linear α -term followed by increasing curvature as the β -term becomes more dominant at higher absorbed doses. The linear term, represented by α , is often interpreted as intra-track interactions yielding non-repairable lethal damages, whereas the quadratic term, represented by β , describes intertrack interactions inducing sublethal damages that may coincide to yield lethal damages [94].

In the version of the LQ model described above, it is assumed that fractions are delivered instantaneously and are so well separated in time that all sub-lethal damage is fully repaired between fractions. However, this is not the case for nuclear medicine exposures, where the absorbed dose is delivered over a protracted time, allowing time to repair sub-lethal DNA damage during irradiation. Thus, the surviving fraction will increase for a given absorbed dose when the irradiation is fractionated or protracted. To account for the effect of repair within the context of the LQ model, the application of a dose-protraction factor G to the quadratic term in (Equation 4.2) has been proposed by Lea and Catchside [95]:

$$SF = e^{-(\alpha D + G\beta D^2)} \quad (4.2)$$

Where the dose protraction factor G considers the varying dose rate, the time between sub-lethal DNA breaks, and an exponential repair of sub-lethal DNA breaks. Including sub-lethal DNA damage-repair via the G factor reduces the effect of the intertrack β term, whereas a series of well-separated acute fractions returns to the simple LQ model.

This absorbed dose rate-dependent variation on biological effect, even though the same absorbed dose is delivered, makes the absorbed dose alone a poor parameter for comparing different irradiation schemes. To account for this, the concept of biologically effective dose (BED) was proposed [96-98] defined as the absorbed dose required to cause a given biological effect at a very low absorbed dose rate (equivalently, delivered in infinitely small doses per fraction). In this limit, the quadratic term in the LQ model goes to zero, as all sub-lethal damages will have time to repair before any intertrack interaction can occur. The survival fraction becomes:

$$SF = e^{-(\alpha BED)} \quad (4.3)$$

Solving for BED, the formulation that applies to nuclear medicine becomes:

$$BED = -\frac{\ln(SF)}{\alpha} = D + \frac{G}{\alpha/\beta} D^2 \quad (4.4)$$

Clinical interest in BED in RPT arose in 2005 when it was demonstrated that BED was more relevant than absorbed dose to describe renal toxicity after ^{90}Y -DOTA-TOC treatment [99]. Since then, BED has become more widespread, *e.g.*, within the Iluminet study where kidney BED was used for regions at risk limit [32, 33]. Applying BED instead of absorbed dose to kidneys, as illustrated in the MIRP Pamphlet No. 20, the correlation between the normal tissue response curves for PRRT and EBRT was improved, indicating ways to improve the correlation between different radiotherapies [100]. The greatest uncertainty in the calculation of BED lies in the values for the radiobiological parameters. Values for α and β are traditionally established from *in vitro* cell colony forming assays, which complicate the determination of normal tissue cells. More intricate BED expressions are developed by taking other radiobiological concepts, such as relative biological effectiveness RBE and oxygenation, into account [13].

4.1.3 Stepping away from classical radiobiology

Described above is the standard model of targeted effects, including both direct and indirect damage to DNA [91]. However, the effect of ionization is not strictly localized along the particle track. The so-called “non-targeted” effects include the bystander effect and the abscopal effect, where non-irradiated cells, either on the near cellular level or on the far away systemic level, respond as if they were exposed to radiation. This indicates that the effect of *in vivo* irradiation triggers intercellular communications and systemic responses, even if the irradiation itself was localized. These effects raise the hypothesis that radiation can be seen as an immune system activator, via alterations on the tumour cell surface and its microenvironment [101]. Research in radiobiology can now start to benefit from new technologies and insights from biological research, such as genomics, proteomics and metabolomics-derived models. New hypotheses about the effects of ionizing radiation on biological systems and insights for therapy improvements are anticipated [102].

4.2 Radiobiology in nuclear medicine

The above-described ‘classical’ radiobiology is mostly based on experiments with acute and uniform radiation exposures with high dose rates, which is rarely the physical characteristics of radionuclide therapeutic irradiations. The irradiation response of a biological system depends on the distribution of the absorbed dose in space and time. Hence, the establishment of a relationship between biological effect and the deposited energy is, within nuclear medicine, not straightforward and is related to the intrinsically fundamental differences between EBRT and RPT, as mentioned in chapter 2.3.1.3: time variations in the systemic treatment (pharmacokinetics); spatial nonuniformity of energy deposition due to uptake heterogeneity; physiological transport and mixed radiation qualities; and protracted irradiation and temporal nonuniformity of the absorbed dose; *i.e.* the dose rate. Consequently, the resulting absorbed dose distribution is heterogeneous, and the radiation-induced biological effects are expected to be specific for RPTs.

4.3 γ -H2AX as a biomarker for DNA DSB in tissues

To detect and identify radiation-induced double-strand breaks (DSBs), a specific target that changes with the incidence of DSB must be identified. The most common targets are the phosphorylated variant of the H2AX histone called γ -H2AX, which is formed as a primary response to the induction of a DNA DSB. Hence, detection and quantification of γ -H2AX has been widely used as a surrogate marker for DNA DSBs

and is a sensitive marker for ionizing radiation-induced DSBs [5]. One similar surrogate marker for DSBs is the damage sensor p53-binding protein 1 (53BP1), which is attracted to the chromatin structure surrounding the DSB and has been used to detect radiation-induced DSBs. The local accumulation of DNA damage response proteins are called foci, hence the terminology γ -H2AX or 53BP1 foci.

γ -H2AX foci are formed within seconds to minutes after irradiation and are proportional to the absorbed dose from ^{137}Cs irradiation up to 200 Gy [103]. The absorbed dose needed for observation of irradiation-induced foci depends on the endogenous level of foci within the studied cells or tissue. The first radiobiologic studies of γ -H2AX foci were performed using acute low LET irradiation of fibroblasts and lymphocytes, where the endogenous level of γ -H2AX foci is low. [104].

When this thesis was begun, studies of γ -H2AX after continuous internal irradiation were still rare. A study by Lassmann *et al.* [105] performed on leukocytes from patients administered ^{131}I for thyroid remnant ablation showed an excess foci peak two hours after administration. Afterwards, the foci count decreased even though the cumulated absorbed dose increased. Further studies on *in vivo* irradiated peripheral blood lymphocytes demonstrated a linear relationship between the absorbed dose to the blood and the average number of radiation-induced γ -H2AX foci per cell up to 5 h after treatments with ^{177}Lu Lu-DOTA-TATE and -TOC [44]. Furthermore, studies of *in vivo* irradiated blood leukocytes of prostate cancer patients undergoing PET/CT imaging with ^{68}Ga Ga-PSMA I&T and treatment with ^{223}Ra RaCl₂ have been investigated [106, 107]. High LET alpha particles are associated with the induction of closely stacked DSBs and DNA modifications that can be visualized as tracks of closely packed γ -H2AX foci. *Ex vivo* irradiation of blood leukocytes with the alpha emitters ^{223}Ra and ^{224}Ra revealed a linear relationship of α -particle induced γ -H2AX tracks through their cell nuclei and the absorbed dose to the blood. In contrast, the frequency of small γ -H2AX, indicative of β -irradiation, was similar to the baseline value [108, 109].

In **Paper II** the induction of γ -H2AX foci was quantified in tissue sections from the testis and liver of mice after internal irradiation of administered $^{111}\text{InCl}_3$, showing that it was possible to also use tissue biopsies as a tool to study absorbed-dose response relationships after internal irradiation. However, the formation of γ -H2AX is not restricted to DSB induction. Uniform pan nuclear γ -H2AX staining is an indicator of apoptosis, where all the DNA in the nucleus is fragmented [110]. Furthermore, in the testis, the creation of haploid germ cells requires the formation and repair of meiosis-specific DNA DSBs through programmed changes in the chromatin structure [111, 112].

4.4 Visualizing tissue properties

The main task in experimental radiobiology is to accurately measure tissue response through a reliable system of measurements, *i.e.* performing an assay. These can be assays of tissue function, such as blood cell counting as an indicator of bone marrow function, or clonogenic assays, where irradiated cells' possibility of proliferation is investigated [88]. Through a DNA damage assay, it is possible to label and measure initiated DNA DSB repair by antibody detection of the phosphorylated form of histone H2AX (γ -H2AX).

4.4.1 Immunolabeling

Immunolabeling in the form of immunohistochemistry (IHC) or immunofluorescence (IF), is a biochemical technique used to find and identify cell types or cells undergoing a specific process. Cells or a specific cell process can be identified using a primary antibody specific for an antigen present on or within the cells at its spatial position within a tissue section. The antigen–antibody binding can be visualized using a chromogen or a fluorophore, connected to either the primary antibody (direct method) or a secondary antibody (indirect method), specific for the primary antibody (Figure 4.3 C) [113].

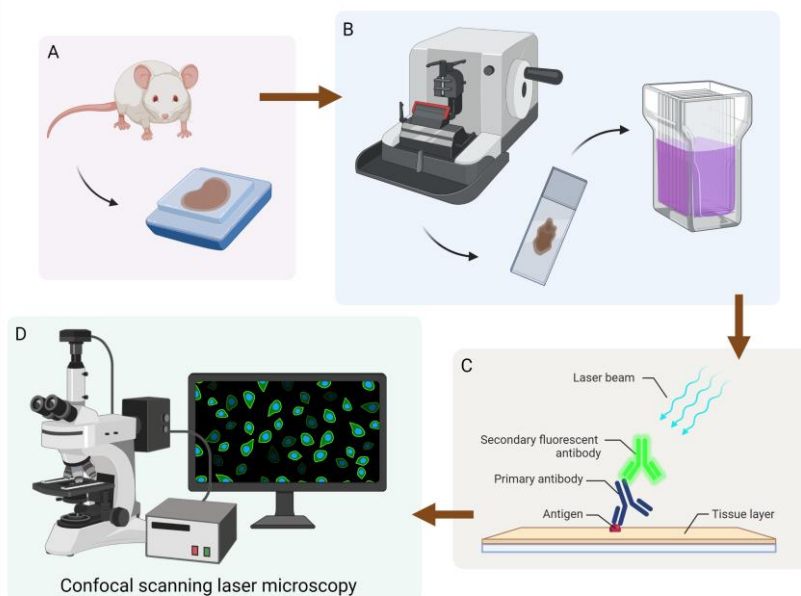


Figure 4.3. Schematics of the IF process of visualizing a tissue properties. Tissue biopsies from mice are fixated and embedded (A), followed by tissue sectioning and staining (B). Sub-figure C shows the indirect method of visualizing the tissue antigen via a primary antibody specific against that antigen and fluorophore-carrying secondary antibody, specific against the primary antibody, that is excited via laser light. Sub-figure D illustrates a microscopy setup. Figure created with BioRender.com

The technique comprises two main steps: the preparation of the tissue section in combination with the laboratory steps involved in the biochemical reaction (figure 4.3 A and B), and the interpretation and quantification of the antibody expression (figure 4.3 D). The first step includes fixation of the tissues or cells. Fixation prevents autolysis and displacement of the cell constituents and preserves the cellular components within the tissue and can be done either by fast freezing the tissue or by formalin fixation. The following laboratory steps in the IHC or IF process are often specific to the protocol designed to identify the antigen of interest. Regardless of the protocol design, antigen-antibody binding sites must be visualized by either a chromogen (for IHC) or a fluorophore (for IF). Chromogens will be visible using a bright field microscope. In contrast, the fluorophores need to be excited by photons of a specific wavelength, and their emission light detected to visualize their binding sites. Hence there is a need for different microscopy techniques, depending on the labelling method.

The haematoxylin-eosin (H&E) stain is one of the standard stains for IHC examinations of tissue sections (figure 4.4). The staining method was introduced more than a century ago but is still one of the common stains performed by pathologists and scientists worldwide [113]. The two dyes stain different cellular constituents within the tissue. The haematoxylin is a positively charged basic dye, staining the cell nucleus and its membrane blue, and the eosin is a negatively charged acid dye, staining the cell membrane, mitochondria, lysosome and other structures within the cell pink. Lipids will remain unstained and will appear as empty spaces [114]. In Paper II, H&E staining is used for histological validation of the testis and liver tissue, before further investigations.

Using an IF-method, cell nuclei are often counterstained to create an anatomical background in the image and to give morphological information about the cell nuclei and chromatin structures. Typically, 4',6-diamidino-2-phenylindole (DAPI) that emits blue light or propidium iodide (PI) that emits red light are used. Both these agents bind between the base pairs in the DNA and are called “intercalating” dyes.

For radiobiological purposes, IHC or IF can be used to detect cells undergoing cell death through apoptosis (activated Caspase-3), fragmentation of DNA (TUNEL) [115] or senescence, *i.e.* when a normal cell ceases to divide. Senescence-Associated-(SA) beta-Gal [116] detects alteration in cell proliferation (Ki67) [117] or repair of double-strand breaks (γ -H2AX, 53BP1) [118].

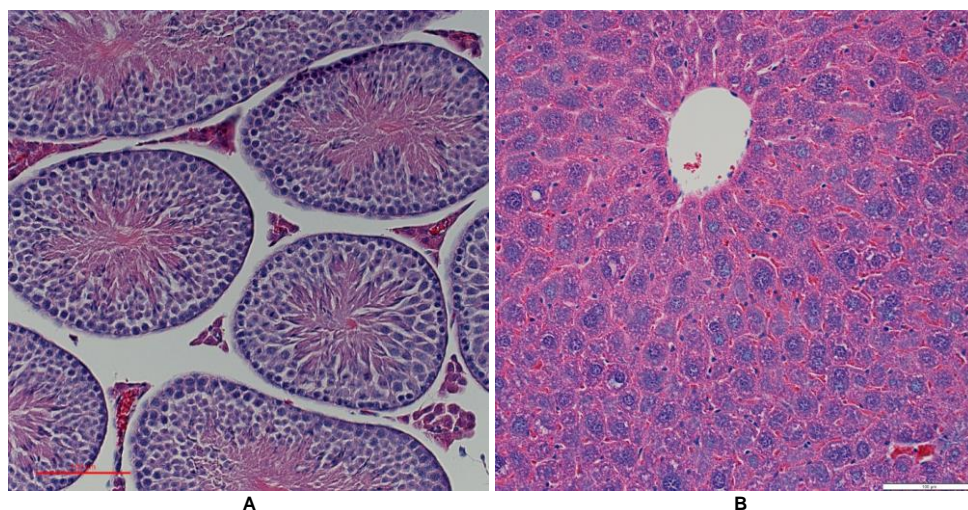


Figure 4.4. Tissue sections (5 μm thick) from testes (A) and liver (B) stained with H&E staining. (A) show a cross-section of the seminiferous tubules containing differently-matured spermatogenic cells. The seminiferous tubules are surrounded by interstitial tissue, which contains blood and lymphatic vessels, nerves, tissue macrophages, and groups of endocrine Leydig cells responsible for the secretion of testosterone [64]. Blue colours represent cellular nuclei, and pink represents the sperm cells that are released into the lumen in the centre of the tubule, as well as the erythrocytes visible within the vessels in the interstitial space. (B) shows a cross-section of a liver lobule, with the central vein at the top of the image and a portal tract vessel in the bottom right corner. Blue colours represent cellular nuclei, whereas pink represents the cytoplasm of the hepatocytes. The hepatocytes constitute the bulk cells of the liver parenchyma. They are surrounded by the liver capillaries—the sinusoids—some of them containing erythrocytes. The scale bar (red in (A), white in (B)) represents 100 μm .

4.4.2 Microscopy imaging

To assess the results of the IHC and IF labelling, optical tools are needed. Light microscopy is most common, which can be further divided into bright-field and fluorescence microscopy.

4.4.2.1 Bright-field microscopy

Bright-field microscopy uses the transmission of white light through the sample, where the contrast within the sample is generated by differences in absorbance of the transmitted light within the sample. The typical appearance of a bright-field microscopy image is a bright background with darker sample structures. To enhance the contrast between different tissue structures, tissue-specific stains, such as H&E-staining, are used to enhance contrast within the tissue section.

4.4.2.2 Wide-field fluorescence microscopy

In fluorescence microscopy, the fluorescent light from the sample itself and the fluorophores added to it are used to create an image with increased detail visibility than that of bright-field microscopy. An excitatory light, suitable for the fluorophores applied to the tissue sample, is passed through the objective and onto the sample. The

light emitted from the fluorophore is led to an eyepiece on the microscope and/or to a camera, for visual inspection or image capture fluorophores location [119].

The light source within a fluorescence microscope is either a Xenon- or Mercury-arc-discharge lamp, or a high-powered LED or laser source. Depending on the light source, different filters and dichroic beam splitters, reflecting wavelengths below the transmission wavelength and transmitting wavelengths above, are used to produce monoenergetic excitation light and capture monoenergetic emission light at the detector. By changing this unit, called a filter cube, fluorophores absorbing and emitting light in different wavelength intervals can be illuminated, and different labelled structures within the sample can be visualized sequentially. Different filters can be used depending on the mixture of fluorophores within the sample. Long-pass filters, passing all wavelengths past a certain value, will give a more intense signal for a given fluorophore than a band-pass filter, passing only wavelengths within a narrower interval. Thus, for samples labelled with multiple fluorophores, band-pass filters will often be necessary to avoid overlapping the emission spectra from different fluorophores and achieve full spectral separation of the fluorophores [119].

In wide-field fluorescence microscopy, the whole depth of the sample is illuminated evenly and excited with the excitation wavelength, leading to a full-depth emission of fluorescent light, with a high amount of out-of-focus light detected. This can obscure the resolution of the image and lead to a loss of fine details. However, the technique may be suitable for thin samples, or samples with high fluorescent intensities restricted to thin shells, or when spatial resolution is not the main objective [120]. Used together with slide scanning techniques, whole slide microscopy images can be acquired by stitching several fields of view (FOVs) together, enabling high specificity investigations of large tissue areas.

4.4.2.3 *Confocal laser scanning microscopy*

Confocal laser scanning microscopy (CLSM) offers advantages over conventional wide-field microscopy via the ability to detect emission light primarily from the focal plane, which eliminates or reduces background signal not emerging from the plane of interest. This also enables the collection of light from individual optical sections from different depths of thick specimens.

The excitation light source within a CLSM is a laser source that passes through a pinhole aperture situated in a conjugate plane with a scanning point in the tissue sample. A second pinhole is situated in front of the detector, often a photomultiplier tube (PMT). The excitation laser light is reflected by a dichromatic mirror and passed to the tissue sample. The fluorescent light emitted from point in the focal plane within the tissue sample will be passed back through the dichromatic mirror and are focused as a confocal point at the detector pinhole aperture. Hence, the pinhole excludes out-of-focus light and only light from one optical section is detected. However, a single point within a tissue sample does not provide that much information, which is why the laser spot needs to be scanned over the sample to acquire full spatial information. The

scanning is often performed by using galvanometer-based oscillating mirrors, allowing the spot of illumination to be raster-scanned over the area of interest. By a consecutive change of focal plane, optical sections at different depths of the section can be obtained, often called a z-stack [121].

In **Paper II**, 5 μm thick specimens of testis and liver tissues from mice after intravenous administration of $^{111}\text{InCl}_3$ were scanned with CLSM to capture optical sections to be able to separate overlapping foci. Z-stacks of the sections were created before the image analysis.

4.4.3 Image analysis

Conventionally, microscopy images were qualitatively and comparatively analysed through the eyepiece of the microscope. With the development of digital imaging, different techniques with the purpose of segmenting different image properties for quantitative analysis have evolved. In **Paper II** quantitative techniques to segment and count the number of $\gamma\text{-H2AX}$ foci within cell nuclei were applied.

In image segmentation, an image is divided into different regions, or segments, having one or more characteristics in common. The process can be divided into two main steps: recognition and delineation [122]. The process of determining where the object to be segmented is within the image is called recognition, whereas the process of delineation defines the spatial position and extent of the object region within the image. These two processes make it hard to develop automatic imaging segmentation methods, since the recognition step often requires an experienced operator.

One of the simplest image segmentation methods is thresholding. A thresholding method will divide an image into two regions: the object region containing all pixels with a pixel value above the threshold value, and the background region containing all pixels with pixel values below the threshold value. The operator can set the threshold value as a fixed fraction of the maximum value within the image. Thus, the optimal threshold will vary with object size, image contrast and system spatial resolution [123]. Image thresholding was used in the image analysis of **Paper II** to help delineate cell nuclei and foci in the CLSM images, using the freeware software ImageJ [124]. .

4.5 Targeting, labelling, and visualization of γ -H2AX foci in testis and liver tissues after systemic irradiation

In **Paper II** a cell-specific analysis of DNA DSB in testis and liver tissues was developed after systemic irradiation of mice from $^{111}\text{InCl}_3$. At the time, there were almost no *ex vivo* studies of normal tissue DNA DSB induction after *in vivo* irradiation from radionuclides. Hence the aim was to develop a method suitable for labelling, visualization, and quantification of DNA DSB.

The target of choice for the analysis was the DNA DSB surrogate marker γ -H2AX, labelled using antibodies against the phosphorylated form of H2AX histone protein. Cell nuclei were counter-stained with DAPI. The labelling protocol for immunofluorescence with anti- γ -H2AX antibodies, conjugated with the fluorophore Alexa Fluor 568, was optimized for labelling of formalin-fixed tissue sections, and imaging acquisition parameters were determined for CLSM imaging of 5 μm tissue sections. Representative images for testis and liver sections are shown in figure 4.5.

Quantification of intranuclear γ -H2AX foci was performed in high-resolution 3D CLSM image z-stacks. An image analysis pipeline (macro) was designed first to segment the cell nuclei in each z-stack to use that delineation as a mask wherein the γ -H2AX foci were counted.

The testis analysis was performed in morphologically identified spermatogonia (type A and B) and primary spermatocytes (*i.e.*, diploid cells) which previously have shown induction of radiation-induced γ -H2AX foci [125]. For the image analysis of the testis nuclei, only the γ -H2AX positive channel was used to determine both the number of nuclei and the number of foci within each z-stack. The number of nuclei was manually counted, whereas the number of foci was determined using the built-in function 3D Foci Picker [126] within the ImageJ software [124]. A γ -H2AX focus was defined as a coherent region larger than 20 voxels, with one local maximum, and the average number of foci per nuclei was determined for each animal.

The analysis of the liver z-stack images aimed to determine the average number of γ -H2AX foci per cell nuclei within hepatocytes and non-hepatocytes. Image analysis was initiated using the maximum intensity projection (MIP) of the DAPI channel to, by thresholding, create a two-dimensional (2D) mask of the nuclei border. The mask was applied to the 3D image of the γ -H2AX positive channel, defining the regions wherein γ -H2AX foci were to be segmented using the built-in function 3D Foci Picker. For hepatocytes and non-hepatocytes, after manual verification, a focus was determined as a coherent region larger than eight voxels.

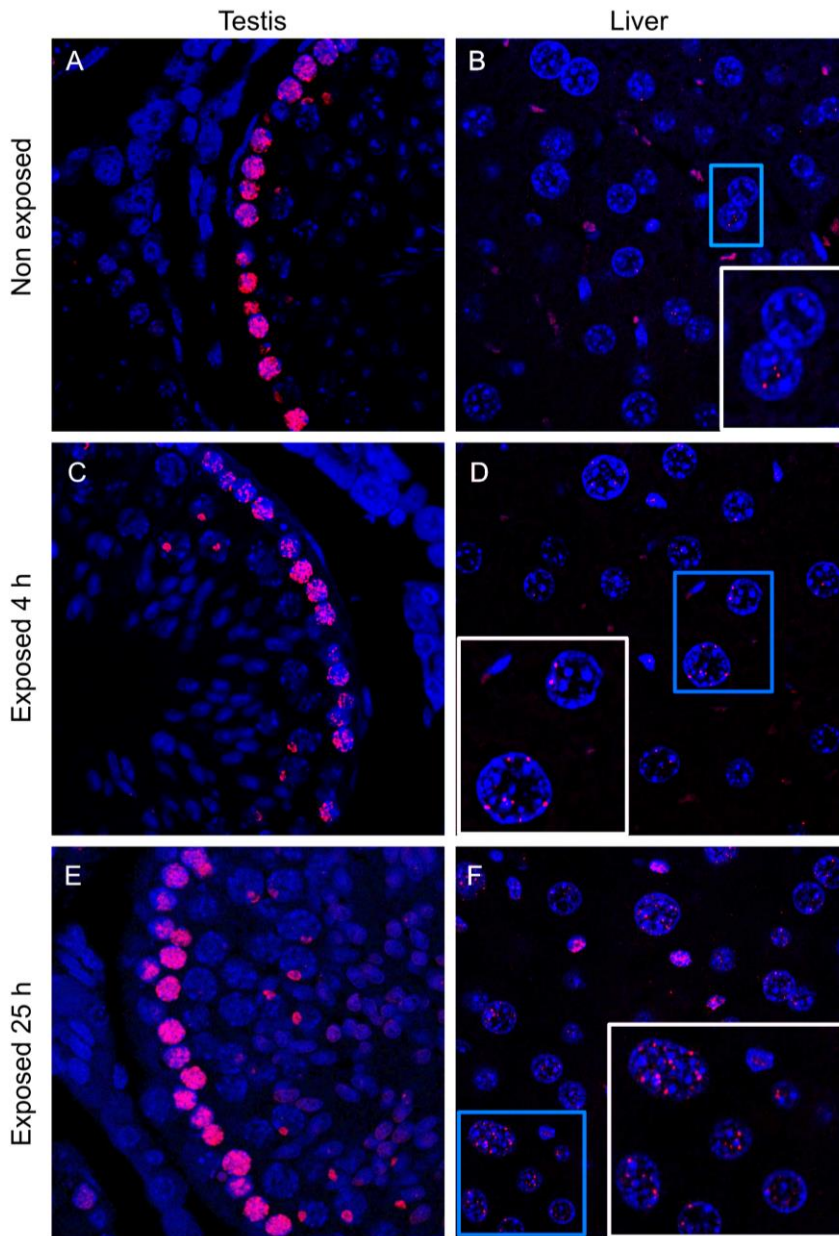


Figure 4.5. Confocal laser scanning microscopy of testis (left column (A, C, E)) and liver (right column (B, D, F)) tissue sections. Shown are on optical section. Top row (A and B) show non-exposed animals, middle row (C and D) show animals exposed for 4 h and bottom row (E and F) show animals exposed for 25 h. Cell nuclei is counter stained with DAPI (blue) and γ -H2AX foci are visualized with Alexa Fluor 568 conjugated secondary antibodies (red). In the testis, spermatogonia (type A and B) and primary spermatocytes nuclei form the high density γ -H2AX foci outer layer of the seminiferous tubules. In the liver, the hepatocyte nuclei circular with bright areas of heterochromatin regions compared with the non-hepatocyte nuclei, which are more elongated in shape and have more homogeneous nuclear staining. Images were adjusted for brightness and contrast. Nuclei within the blue squares are, for higher visibility, enlarged within the white squares. Subfigures are 143 x 143 μm .

On the group level, the irradiation gave rise to average absorbed doses of 20 mGy and 0.1 Gy in the testes and 0.5 Gy and 3.20 Gy in the liver 4 h and 25 h after the intravenous injection of 63 MBq $^{111}\text{InCl}_3$. The results (figure 4.6) were then presented as the average number of γ -H2AX foci per cell nuclei at two different time points. Studying the induction of γ -H2AX foci in the liver and testis, two tissues with major differences in proliferation rate and radiosensitivity, was a way to interrogate the method. A significant difference in the γ -H2AX foci counts between non-exposed and animals exposed for 25h for both hepatocytes and non-hepatocytes. For hepatocytes, the average foci count per cell nuclei rose from 0.5 to 7 foci. For non-hepatocytes, the respective number was 0.06 to 5 foci per cell. In contrast, no significant differences were observed in the primary spermatocytes or spermatogonia in the testis count of γ -H2AX foci between non-exposed and exposed animals. However, a higher endogenous number of foci per cell nuclei of around 20 was seen for both exposed and non-exposed animals. Hence, a lower endogenous level of γ -H2AX foci and a higher absorbed dose, as seen in the liver, led to increased separation between exposed and non-exposed animals.

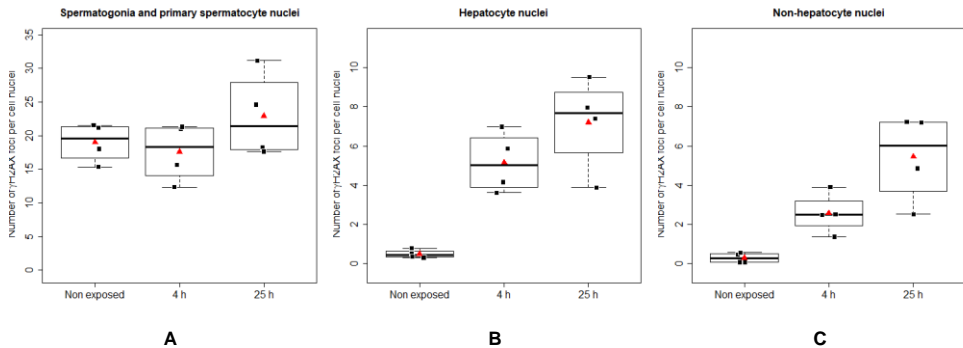


Figure 4.6 Boxplots illustrating the number of identified γ -H2AX foci per cell nuclei for (a) spermatogonia and primary spermatocytes, (b) hepatocytes, and (c) non-hepatocytes for the three groups of animals: exposed for 4 h, exposed for 25 h and non-exposed. The mean value for each animal within a group is illustrated by a black square (■). The points have been randomly displaced along the horizontal axis to increase visibility; it should not be interpreted as a variation in time after injection. The average number of foci per cell is illustrated by a red triangle (▲). The bottom and top of the box are the first and third quartiles and the band inside the box is the second quartile (the median). The whiskers extend between the lowest and the highest observed value that still lies within 1.5 times the difference between the upper and lower quartiles.

5 Imaging, activity quantification and absorbed dose determination

Imaging in nuclear medicine is the central method used to establish a diagnosis or determine an absorbed dose with sufficient accuracy. In this chapter two different clinical imaging systems, the Single Photon Emission Computed Tomography (SPECT), and the Positron Emission Tomography (PET), are briefly presented. Their major components, data acquisition, and image reconstruction are described. Furthermore, methods for activity quantification and absorbed dose determination are presented.

5.1 Imaging in nuclear medicine

Imaging in nuclear medicine is a method used to produce images via position-sensitive detection of the radiation emitted from an object after radiopharmaceutical administration. In a clinical procedure, the object is often a patient that has been administered a radiopharmaceutical for diagnostic or therapeutic purposes. However, equally important are the image quality and calibration phantoms imaged to control or calibrate the system.

In vivo imaging utilizing emitted x-rays or gamma photons originating from radioactive decay inside the body, can be used for functional imaging. Examples are detecting or measuring perfusion, ventilation, metabolism, or receptor binding of a specific radiopharmaceutical. In addition, quantitative imaging can determine activity on a macroscopic level; *i.e.*, total body, organs, sub-organs, or lesions. Imaging methods are categorized based on the detection principle. In planar gamma camera imaging and SPECT imaging, single photons are detected, whereas in PET imaging, pairs of photons are detected in coincidence. Gamma camera imaging is based on detecting photons resulting from nuclear transition. PET imaging is based on detecting the 511 keV photons generated in the annihilation process between the emitted positron and an electron in the interacting medium.

The fundamental principle of imaging in nuclear medicine is the simultaneous determination of the incident photon's energy and point of interaction. These spectroscopical characteristics are provided by a scintillation or semiconductor crystal, converting deposited radiation energy into more easily measurable quantities;

scintillation light or electrical currents. The photons originating from the patient or phantom (either primary or already-scattered photons), will deposit energy within the crystal by either photoelectric or Compton scattering interactions. Position determination of this energy deposition is achieved via a geometrical array of sensors coupled to the crystal surface. The term sensor will represent different components depending on the crystal type and readout system. For a scintillation crystal, the sensor would traditionally represent a photomultiplier tube (PMT) or its solid state-based counterpart (SiPMT). Still, it could also represent pixels in a semi-conductor detector, where the photon energy deposited is directly converted into an electrical signal, thus bypassing the need for a PMT [127].

Most clinical nuclear medicine systems today are hybrid systems, where the SPECT or PET camera is serially combined with an x-ray computed tomography (CT) system. This sequential imaging allows for attenuation-corrected hybrid images of the patient's physiology (localisation of radiopharmaceutical) and anatomy (density variations).

One key difference between the gamma camera and the PET system is the method of defining the direction of the incident photons. In the gamma camera system, a lead collimator is placed in front of the crystal. In most cases, it consists of numerous holes and septa, defining which photons are accepted for detection. Photons entering the detector orthogonally or within a small angular range will be projected onto the crystal. Others will be absorbed in the septa. The collimator's dimensions will affect the imaging system's resolution and sensitivity. On the other hand, PET systems do not rely on physical collimation. Instead, it uses electronic logic to perform coincidence detection of the pair of annihilation photons associated with positron decay, which are emitted simultaneous approximately 180° apart. The detection creates a line of response, along which the origin point of decay can be localised.

The imaging system design affects the resolution of the final image. The typical spatial resolution for a SPECT system is 7–15 mm (FWHM) compared to 4–7 mm for a PET system [13].

5.2 The gamma camera and SPECT imaging

The conventional gamma camera consists of one to three (usually two) detector heads that rotate around the patient, which are usually equipped with one full field of view (FOV) thallium doped sodium iodide NaI(Tl) crystal or multiple small cadmium zinc telluride (CZT) crystals. Other specialized semi-conductor SPECT cameras, such as dedicated pinhole collimated cardiac imaging systems, or larger 360-degree systems with a shape-adaptive gantry, are now available.

Major components of the conventional clinical gamma camera of the type used in **Paper III** and **Paper IV** include the lead parallel-hole collimator, a large NaI(Tl) scintillation crystal, a set of PMTs, associated pulse-processing electronics and

computer equipment. When a gamma or x-ray photon interacts in the crystal material, a scintillation; *i.e.*, a flash of visible light, is produced. The light is converted into an electrical signal, registered by the array of PMTs, where the signal is amplified and processed by electronic circuitry. The position of interaction is determined based on the signal distribution over the PMTs, and the total energy absorbed in the interaction is deduced from the sum of signals from all PMTs, a technique first introduced by Anger [128, 129]. The registered energy can be used to distinguish between primary or scattered photons. Since the emissions from a radionuclide are isotropic, a high atomic number and high density (usually lead) collimator is needed to make the imaging system position sensitive. The parallel-hole collimator allows photons travelling perpendicular and within a limited acceptance angle to pass through and hit the crystal (event 1 in figure 5.1). Consequently, the inferred emission position of the photon will lie somewhere along the straight perpendicular line from the point of interaction. This will yield a two-dimensional planar image, reflecting the emission intensity in the plane co-aligned with the collimator where the depth, the third dimension, remains unresolved.

The gamma camera is commonly used in either the above-mentioned planar mode or these 2D planar projections are collected from multiple angles and subsequently reconstructed into a three-dimensional image, referred to as single photon emission computed tomography (SPECT).

5.2.1 Image degradation

Even though the gamma camera system allows for localisation and quantification of energy via photon emissions, the measured projections are degraded due to attenuation, scatter, limited spatial resolution, partial volume effect and septal penetration. Furthermore, the limited number of photons detected will affect the accuracy of the activity quantification.

Attenuation

Attenuation is the interaction of photons, mainly via Compton interactions in the tissue, resulting in a lowered number of detected photons per projection compared to a source located in the air (event 3 in figure 5.1). Photons originating from greater depths within the image object, will have higher probability of attenuation. Hence, attenuation correction is essential for absolute quantification. In hybrid SPECT/CT systems, an attenuation map is acquired from the x-ray CT. The Hounsfield units are converted to attenuation coefficients at the energy of the photons emitted [130].

Scatter

The imaged object will also introduce scattered photons that have interacted via coherent or Compton scattering processes before entering the crystal (event 5 in figure 5.1). Scattered photons will degrade the image contrast and quantitative accuracy since scattered events do not represent the true location of the decay and result in a net increase to the signal. Hence, scatter correction can be energy-based, where the

scattered component in the primary emission energy window is estimated based on the photon count in one or more scatter energy windows flanking the acquisition window [131]. However, the limited energy resolution of a NaI(Tl)-based gamma camera will not allow for perfect discrimination of scattered photons, leaving a contribution of scattered events in the final image. Instead of using measured data for the scatter correction, model-based approaches using Monte Carlo simulated scatter kernels [132], such as the effective source scatter estimation (ESSE) method used in **Paper IV** or analytical methods based on Klein-Nishina cross sections [133], have been developed.

Spatial resolution

The finite spatial resolution, resulting in a blurring of the image from the SPECT system, significantly affects image contrast and quantification accuracy. Spatial resolution effects result in a loss of apparent activity concentration within an object, often referred to as partial volume effects (PVEs) [134]. This is since the object only partially—either spatially or temporally—occupies the sensitive volume of the detector [135]; *i.e.*, the volume from which emitted photons would be detected at a given detector location. The apparent loss of activity concentration is a count redistribution to the surrounding volume, often termed spill-over, and conversely to an overestimation in objects with lower activity concentration compared to their surroundings. This effect can be seen as a convolution between the object and the system point-spread function (PSF). Hence, a large object will be less affected than a small or thin object.

The most widely-used approach to recover the activity concentration and enhance spatial resolution is to implement the system PSF within the reconstruction framework, known as “resolution recovery”. This approach has been seen to reduce, but not eliminate, the impact of PVE while introducing Gibbs-like ring artefacts along the object edges [134]. For SPECT imaging, the PSF is also referred to as the “collimator-detector response”, which consists of the intrinsic response of the detector and three components originating from the collimator response; geometric, septal penetration, and scatter [13]. The geometric response is the dominating effect for low-energy photon emitters—such as ^{99m}Tc —where septal penetration is negligible. The geometric response is then approximated by a distance-dependent Gaussian function, where the full width at half maximum (FWHM) increases linearly as a function of the source-to-collimator distance. Another often-used post-processing method to compensate for the spill-out is the use of recovery coefficients (RCs), defined as the apparent activity concentration of an object divided by its actual concentration. The RC can be calculated based on the PSF of the imaging system and the geometry of the object [134] or be experimentally determined from phantom measurements in a fixed geometry, often using spheres of different sizes in a homogeneous activity concentration background [136-138]. The object size and the object-to-background ratio will strongly affect the RC and measured RCs are applicable only in the given environment.

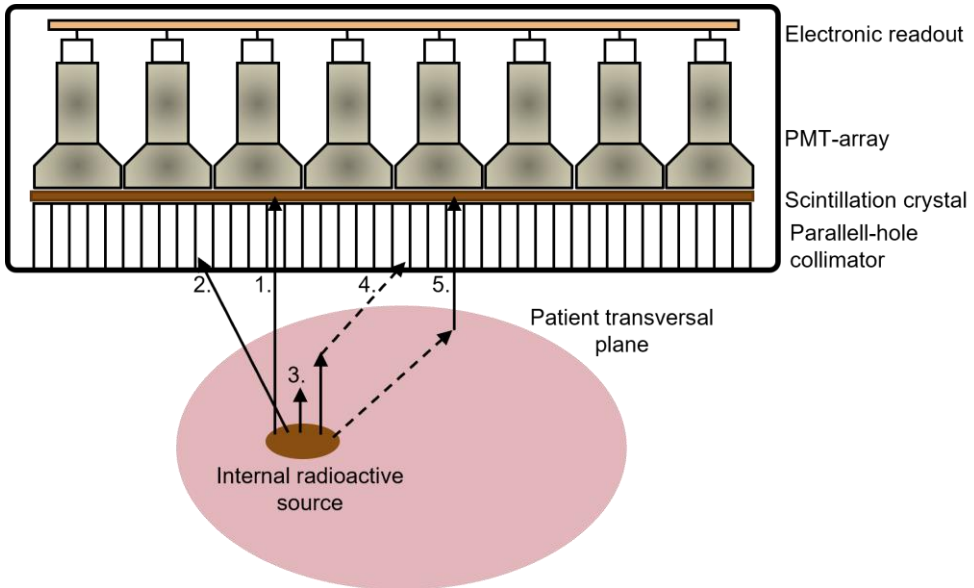


Figure 5.1. Illustration of the essential components of a conventional gamma-camera and the photon interaction process. Photons emerging from a source within a patient may be transmitted through or scattered within the patient. Unscattered photons will, depending on their angle of incidence to the collimator, (1) be transmitted through to be absorbed in the crystal or (2) be absorbed in the collimator. Photons may (3) interact by photoelectric effect or, more realistically, interact by multiple Compton scattering within the patient, never reaching the crystal. Photons may Compton scatter, resulting in (4) potential absorption in the collimator or (5) the detection of a scattered secondary photon.

5.2.2 SPECT reconstruction and calibration

Reconstruction

Tomographic reconstruction of 2D projections is performed to create a 3D image to overcome the principal limitation of planar imaging, the lack of source-depth information. By rotating the detectors around the patient or object in the conventional SPECT system, projections of the activity distribution at multiple angles are acquired. Both analytical and iterative methods can be used to reconstruct 3D distribution data from 2D projections.

An analytic approach is the filtered back-projection, a mathematical method used to compute the image directly, which was the dominant approach in the early days of SPECT reconstructions. The intuitive starting point is to invert the projection, *i.e.*, directly back-project via even distribution of the signal along its acquisition angle and use the sum over all projection angles as the tomographic image. Mathematically this is the inversion of the Radon transformation, which describes the projections at different angles as line integrals of the source distribution [139]. Thus, it assumes straight-line projections and does not take attenuation and scatter into account, and an analytical model accounting for these effects would be complex and challenging to create [140].

As an alternative to analytical methods, iterative techniques are more suitable for incorporating complex models for image-degrading effects and offer the best quantitative performance. Today, iterative methods are often used in clinical practice to reconstruct tomographic images, even though being more computationally demanding [138]. The principle of iterative reconstruction is to find a solution through a series of successive refinements. The process is initiated with an initial first estimate of the activity distribution, typically a uniform image. The calculated projections of the estimate—where the system model, including selected compensations for image degradation effects, are included in the projector model—are compared to the measured projections, and the result is used to modify the current estimate. The process is typically stopped after a predefined number of iterations has been performed. [139]. The most widely used iterative algorithm for the reconstruction of emission images is the maximum likelihood expectation maximization (ML-EM) [141] or its accelerated counterpart ordered subsets expectation maximization (OS-EM) [142].

The convergence of the ML-EM algorithm is relatively slow since all image projections are used for each image update. The accelerated process of OS-EM processes the data in blocks (subsets) of projections, and the image is updated after each subset. This procedure accelerates convergence by a factor proportional to the number of subsets [142]. This has made the OS-EM algorithm the clinical standard method for the reconstruction of SPECT images. However, a known shortcoming of EM-reconstructions is the excessive noise in the images if many iterations are used to reach full convergence. Hence, regularization algorithms utilizing a penalty function that prohibits excessive noise while still reaching full convergence are being used clinically.

Calibration

Prior to calibration of the gamma camera system, calibration of the activity meter for a specific container needs to be assured. The measured activity should be traceable to a primary standard, which can be assured by calibration of the dial settings of the activity meter for the corresponding isotope toward a source with a traceable activity statement. The importance of cross-calibration of in-house sources to an activity meter with traceability to primary standard was shown in a study of international multi-centre investigation [143].

Projections and raw images from the gamma camera come in the unit of counts, *i.e.* the number of photons registered to each image voxel, representing the spatial distribution and the amount of activity as seen by the camera. A truer distribution is obtained by correcting the raw images for image-degrading effects, which is of interest to both qualitative use and quantitative values. Transformation of the image from counts into units of activity or activity concentration—an essential integral step for the absorbed dose calculations—requires a conversion factor describing the fraction of decays that gives rise to an event in the given energy window, *i.e.* the system sensitivity, commonly denoted in counts per second (cps) per MBq (cps/MBq).

Two main methods of achieving system sensitivity are to either measure the planar count rate per unit activity in air or in a reconstructed image of a phantom. The in-air measurement is easily performed by measuring a shallow layer of known activity in a Petri dish. But for the calibration to be fully accurate in a reconstructed image, the image degrading effects, such as scatter and attenuation, must be fully compensated for in the reconstruction. Calibrations from reconstructed images of a phantom better approximate the scatter and attenuation properties of a patient image—provided that the acquisition and reconstruction are equivalent for both the calibration and the patient study [138].

5.2.3 Image segmentation

Image segmentation, as defined in chapter 4.4.3 is when an image is divided into different segments that share one or more characteristics. Dosimetry in radiopharmaceutical therapy (RPT) for tumours and regions at risk is based on SPECT image segmentation and extraction of the enclosed activity or activity concentration. Several methods for segmentation exist and need to be both robust and accurate; robust in terms of user-independent results and accurate in terms of proper delineation of the object border to achieve the truest possible object volume and object activity concentration [137, 144]. Image segmentation is affected by image resolution, size, shape, location (lesion to background ratio), and image noise, resulting in low contrast and unclear boundaries between objects [122].

The most common method in medical image segmentation is manual delineation, which suffers from being intra- and inter-operator dependent and time-consuming [122], especially in SPECT images due to its 3D nature. Threshold-based segmentation methods may be the most commonly proposed segmentation methods, ranging from fixed thresholds to adaptive or iterative methods [137]. Fixed thresholds delineate all voxels with values above or equal to the threshold value (usually a percentage of the maximum value) inside an initial VOI. The optimum threshold depends on object volume and shape, target-to-background ratio, the imaging system and reconstruction. Different methods to adapt the threshold relative to the background level exist. In **Paper III** the following formulation was used¹:

$$T_{adapt} = T \cdot \frac{(AC_{max} - AC_{BG})}{AC_{max}} + \frac{AC_{BG}}{AC_{max}} \quad (5.1)$$

where T_{adapt} is the background-adapted threshold, T is the uncorrected threshold value, AC_{max} is the measured maximum activity concentration in the VOI, and AC_{BG} is the mean activity concentration of the background, a method presented by Firouzian et al. [145], and illustrated in figure 5.2.

¹ In the published article (**Paper III**), unfortunately equation 5.1 is wrongly presented.

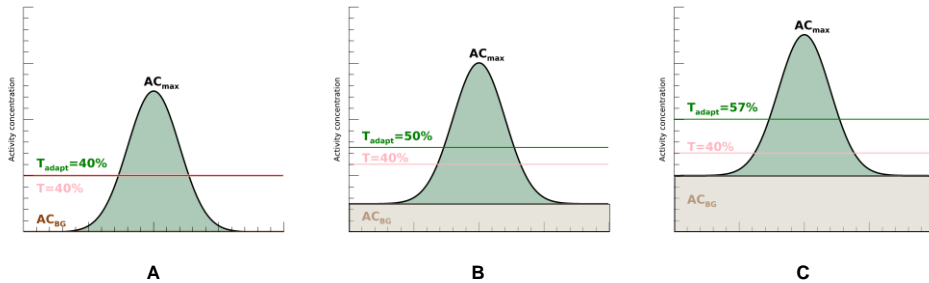


Figure 5.2. Illustration of the background-adapted threshold method for three different background ratios: no background (A), background ratio 0.2 (B) and background ratio 0.4 (C). The maximum measured activity concentration (AC_{max}) is assumed to be the sum of the actual uptake (green) and the background activity concentration (AC_{BG}) (beige). Using equation 5.1, the selected threshold of 40 % (illustrated with pink lines) are adapted relative to the mean background, resulting in adapted thresholds (T_{adapt}) of 50 % and 57 % for the two background ratios of 0.2 and 0.4 (panel B and C).

Within the group of semi-automatic methods, where recognition still is a manual process, but delineation is an automatic process, we find the method of deformable surfaces based on Fourier descriptors. The Fourier surface method aims to determine appropriate values for a set of Fourier coefficients for a given number of Fourier orders, such as the resulting surface enclosed around the object represented in the SPECT image. The method is shown to be advantageous if the image noise levels are high, *i.e.*, for tumour imaging over long periods of time [137].

Using phantom images of either physical or digital phantoms is one way to create a surrogate truth to determine the performance of a segmentation method, even though human anatomy and associated motion blurring is hard to mimic in a phantom measurement [122]. In **Paper III**, the first three mentioned methods; manual CT-based delineation, fixed threshold, and background adjusted thresholding, were applied to SPECT images of ^{111}In and PET images of ^{68}Ga , to investigate the accuracy of volume and activity concentration estimations for different sphere sizes in various sphere-to-background ratios (SBRs). In **Paper IV** normal organs were segmented using manual delineation, relying on the CT for guidance. The tumours were manually identified by defining a rough VOI encompassing the tumour with a margin, and the tumours were delineated using an automatic method based on Fourier surfaces [137].

5.2.4 Time activity determination and absorbed dose calculations

Quantitative imaging is the basis for image-based dosimetry since there is a linear relationship between absorbed dose and the time-integrated activity (TIA), where $TIA = \int A(t)dt = \tilde{A}$ within the source region. Hence, the activity distribution and kinetics over time are needed.

5.2.4.1 Time-activity determination

The activity in the source region can be determined in several ways, including quantitative gamma camera imaging, either planar or SPECT, followed by image

segmentation of the source regions. The activity can also be determined via non-imaging techniques, such as tissue sampling of biopsies, blood, or urine [59]. Such measurements are often performed using a well-type NaI(Tl) gamma counter to achieve near 4π measurement geometry, yielding counts per unit time. The measured counts per unit time are converted to activity using calibration factors for the specific radionuclide, measured sample volume, and container. By measuring tissue sample weight in grams, the biodistributions data output is often reported as activity per gram of tissue at a specific time point.

These measurements produce only single or multiple time points, which need to be interlinked to obtain a continuous activity curve. A simple and accessible method is interpolation between time-points, sometimes in combination curve fitting with mono-exponential extrapolation of the decay phase. It is also possible to obtain time-activity curve (TIAC) in the source region using pharmacokinetic compartment models, describing the time-dependent biokinetic distribution of activity in the source organs and/or sub-organs of interest. The model simulates various source regions, in which the time-dependent activity is calculated by a set of first-order differential equations, linking the various compartments in the model [59, 146].

5.2.4.2 Absorbed dose determination

The accuracy of the TIAC depends on the methods used for its determination. A multiple time-point SPECT activity quantification is considered more accurate than a hybrid technique since the correction methods are more precise, and in-depth information is obtained through the 3D structure of the images. However, planar acquisitions are more suitable for whole-body imaging and offer a lower workload regarding delineation compared to SPECT images. Hence, a hybrid planar-SPECT approach is used in **Paper IV**, with the underlying assumption that the general shape of the time-activity curve can be determined from planar images, but the absolute amplitude of the curve is better determined from a single time-point SPECT image, which is used to scale the planar-derived curve [147].

An EGS4-based Monte Carlo program was used for the image-based dosimetry to calculate absorbed dose rate images [86, 148]. Shortly, an activity voxel-map determines the probability of a simulation history to begin with, given a decay point within the voxel by uniform sampling. A particle: *i.e.*, a photon or an electron, is traced until its energy falls below the defined cut-off energy, after which the remaining energy is assumed to be locally absorbed. In **Paper IV**, the absorbed dose-rate maps were calculated from SPECT images with 40 iterations and 6 angles per subset with compensations for attenuation, scatter, and resolution. Images were calibrated, by an in-air measurement of the system's sensitivity, to reflect activity per voxel. Absorbed doses were calculated under the assumption that the absorbed-dose rate followed the shape of the time-activity curve and was achieved by analytical integration according to the method described in Roth *et al.* [149].

5.3 PET camera and imaging

The positron emission tomography (PET) camera is based on the coincidence detection of the pair of 511 keV annihilation photons generated when the emitted positron has reached its rest energy and then interacts with an electron. The PET camera system consists of a ring of detectors surrounding the patient, enabling simultaneous detection of the generated annihilation photons. The detection medium in the PET camera is a scintillation crystal, typically cerium-doped lutetium oxyorthosilicate (LSO(Ce)), and the visible light created in the interaction process, proportional to the energy deposited by the photon, is converted to an electric signal by conventional PMTs or SiPMTs. The PET camera used in **Paper III** and **Paper IV** was equipped with conventional PMTs.

The nature of the two emitted annihilation photons emitted from the same event makes physical collimators obsolete. Instead, collimation is electronically performed by coincidence detection, where the two annihilation photons are detected in two opposing detectors within a specified coincidence timing window. The point of emission origin is along this line of response (LOR). Further development introduced time of flight (ToF) PET, where the time difference between detection in the opposing detectors can restrict the position of annihilation to a subsection of the LOR [133].

The non-physical collimation results in a higher detection yield in PET compared to SPECT. This gain in sensitivity can be used for improved image quality, shorter imaging times and multiple FOV imaging. However, coincidence detection also introduces issues affecting the resolution, one being the non-linearity of the annihilation photons, the other being detection of random coincidences.

5.3.1 Image degradation in PET

Event detection in the PET camera relies on electronic collimation. Single photons are detected, and if two photons are detected within the predefined electronic time and energy window, a so-called prompt coincidence event is detected. However, the prompt events will consist of true events (annihilation photons created in a single positron-electron annihilation) and accidental detection of photons from unrelated positron annihilations. A random coincidence arises from two positrons in which one photon from each event is counted. A scattered coincidence arises when one or both of the annihilation photons undergo Compton interaction within the patient or phantom. Both random and scattered LORs will be spatially uncorrelated with the tracer distribution (see figure 5.3). Hence, scatter correction and estimation of random events are needed to correct the PET data and improve image contrast and quantitative accuracy.

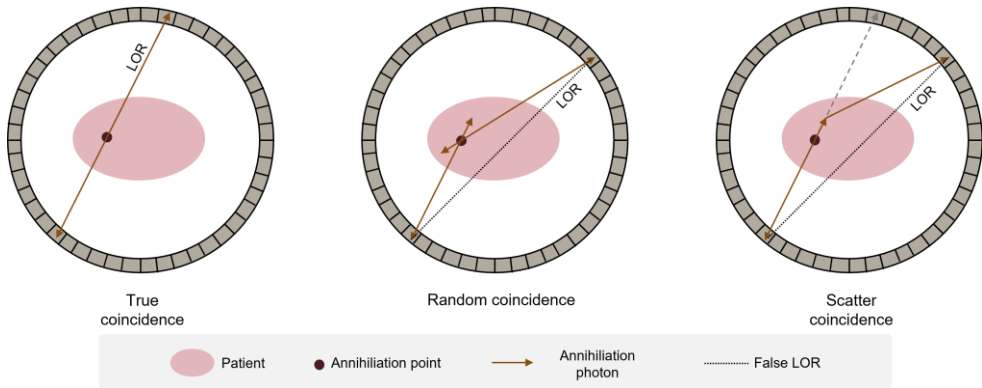


Figure 5.3. Illustration of the three coincidence detections occurring during the PET acquisition; true, scattered and random coincidences. In a random coincidence, the two photons creating a LOR originate from two different decay events, and in a scattered coincidence, one of the photons from the annihilation event is scattered in the object—both random and scattered coincidences results in miss-placed LORs.

Even though the energy of the annihilation photons detected by the PET camera always has the same energy, the energy of the emitted positrons is different for each PET radionuclide. Higher positron energy means a longer path length from the position of positron emission to the position of annihilation, meaning that the measured point of annihilation differs from the point of emission. For ^{18}F , the endpoint energy of the positron is 633.5 keV, resulting in a mean positron range before the annihilation of 0.27 mm in soft tissue. In contrast, for ^{68}Ga the endpoint energy is 1899.1 keV, resulting in a pathway almost four times longer, *i.e.* 1.05 mm [150]. Since the momentum of the emitted photon and the electron with which it annihilates can be non-zero, a non-collinearity of the annihilation photons can be introduced. The deviation is around $180 \pm 0.25^\circ$, which will introduce resolution blurring [133].

5.3.1.1 Attenuation

In PET, the dually-emitted photons must travel the full thickness of the imaged object to reach each opposing detector. Therefore, attenuation is independent of the point of annihilation along the LOR, thus making the attenuation correction in PET more straightforward than in SPECT. Incorporation of the CT-determined attenuation factors can either be done as a pre-correction in the measured data or applied as a correction in the reconstruction [133].

5.3.1.2 Random coincidences

Random coincidences in PET originate from two different annihilation events, as illustrated in figure 5.3, where two uncorrelated single events are detected sufficiently close in time to be mistakenly identified as a true coincidence. The occurrence rate of random coincidences is related to the singles rate and the width of the timing window. Random coincidences provide false information, which results in a loss of contrast and quantitative accuracy. Hence corrections for random coincidences are required for

quantitative PET reconstructions. There are two common ways for random correction: using a delayed timing window or estimating the random event rate from the measured singles rate [13]. The latter method is applied for PET images in **Paper III** and **Paper IV**.

5.3.1.3 Scatter

As in SPECT imaging, the imaged object will introduce scattered photons, which will introduce non-correct LORs that are not colinear with the site of annihilation and can be positioned outside of the imaged object. The proportion of accepted coincidences that have undergone Compton scattering is referred to as “scatter fraction”, and its magnitude can, for a 3D PET system, be 40–60% [133]. The most common method of scatter correction in PET today is single scatter simulation (SSS), which assumes that the scattered photons that fall within the photopeak window have only been scattered once, *i.e.* single-scattered events [151]. The probability of scatter is object-dependent. It is hence possible to, through analytical or numerical Monte Carlo methods, estimate the initial scatter contribution to each projection based on the attenuation map of the scattering medium densities.

5.3.1.4 Prompt gamma

Some PET-radionuclides have a decay branch to an excited state of its daughter nuclide, which is followed by prompt gamma emission. The decay of Gallium-68 (^{68}Ga) has a positron branch to an excited state of the daughter nuclide ^{68}Zn , which emits a prompt gamma photon of 1.077 MeV to reach its ground state. Thus, there is a risk of coincidences between an annihilation photon and the prompt gamma photon. Hence, a correction for prompt-gamma were applied for PET images in **Paper III** and **Paper IV**.

5.3.2 Calibration

5.3.2.1 Calibration

For PET cameras, the system sensitivity, just as for the gamma camera system, is determined from a measurement using a calibration phantom. Thus, contrary to the gamma camera, the calibrations are solely performed using reconstructed images of a phantom. The user is then obliged to periodically check and re-calibrate the system, using a cylindrical phantom with a uniform solution with a known concentration of a known PET-radionuclide. The system sensitivity is often embedded in the system software, making voxels directly displayed in activity concentration (kBq/ml). Hence protocols for the correct isotope are needed since the system sensitivity is scaled to the positron yield of the relevant radionuclide.

5.3.2.2. Semi-quantitative measures

The standardized uptake value (SUV) is a quantity closely connected to PET imaging, but it is defined as a measure of the uptake in an organ, part of an organ, or a tumour normalized on the basis of a distribution volume [152]. Hence, the SUV value can also be calculated for SPECT images. The most used version of the SUV is the one normalized to the body weight (BW) of the patient, denoted SUV_{BW} :

$$SUV_{BW} = \frac{AC_{VOI}(t)}{A_{adm}(t)/BW} \quad (5.2)$$

where $AC_{VOI}(t)$ is the activity concentration in the specified VOI at time t , $A_{adm}(t)$ is the administered activity at time t , and BW is the body weight in kilograms. Hence, SUV is defined in units of $g\ mL^{-1}$.

For metabolic tracers such as $[^{18}F]FDG$, SUV can be used as a reasonable measure of metabolism, assuming the tracer's distribution volume is the whole body since all tissues consume glucose. For receptor ligands, such as $[^{68}Ga]Ga-DOTA-TATE$, the distribution volume is instead tissues with uptake of tracer, which may affect the SUV values [153]. The SUV value will be affected by the size of the uptake since it is proportional to the apparent activity concentration. Also, SUV is affected by physiological factors, such as blood glucose level, accumulation time of the radiopharmaceutical, patient and breathing motion during imaging, and technical factors, such as the calibration of the PET-camera system acquisition and reconstruction parameters and VOI segmentation [154].

6 Quantitative imaging for neuroendocrine tumours

Imaging of neuroendocrine tumours is performed by targeting the somatostatin receptor (SSTR), which is expressed in tissues and organs throughout the body, but with an especially high receptor density in neuroendocrine tumours (NETs). It is estimated that at least 80 % of well-differentiated NETs express SSTR [155].

Pre-therapeutic imaging of neuroendocrine tumours is preferably performed today using [^{68}Ga]Ga-DOTA-TATE or [^{68}Ga]Ga-DOTA-TOC to assure adequate receptor expression. PET/CT whole-body images are usually acquired 60 min after injection due to the short half-life of the radionuclide ^{68}Ga [156]. To achieve quantitative accuracy of the images, acquisition and reconstruction parameters need to be optimized, corrections for image-degrading effect applied, and the PET/CT system calibrated. The use of the same or similar peptides for imaging and therapy, or “theragnostics”, offers unique assistance in therapy stratification, but there is no current consensus on the predictive value of ^{68}Ga -SSTR-PET/CT imaging with respect to response, absorbed dose to, or activity uptake in tumours and normal organs after the [^{177}Lu]Lu-DOTA-TATE therapy.

During PRRT with ^{177}Lu -SSTR analogues, peri-therapeutic imaging is possible due to the properties of the radionuclide ^{177}Lu , which undergoes β^- decay to stable Hafnium-177, with a half-life of 6.647 days. The emitted beta-particle has a mean energy of 149 keV per decay and a maximum electron energy of 498 keV [29]. Corresponding to ranges (continuous slowing down approximation) in soft tissue of 0.28 mm and 1.8 mm [28]. This decay also results in the emission of gamma photons where the 112.9 keV (yield 6.2%) and 208.4 keV (yield 10.4%) photons are used for gamma camera imaging. For peri-therapeutic imaging of [^{177}Lu]Lu-DOTA-TATE, with a dosimetry purpose, a minimum of three time-points is recommended, performed on the day of administration (between 1 and 4 h), up to 7 days post-administration [43]. Hybrid planar-SPECT imaging, including rescaling the time-activity curve to the SPECT image, yields a quantitative time sequence of images. An example of a patient’s PET/CT, acquired 1 h after injection of [^{68}Ga]Ga-DOTA-TATE and SPECT/CT image acquired 24 h after administration are shown in figure 6.1.

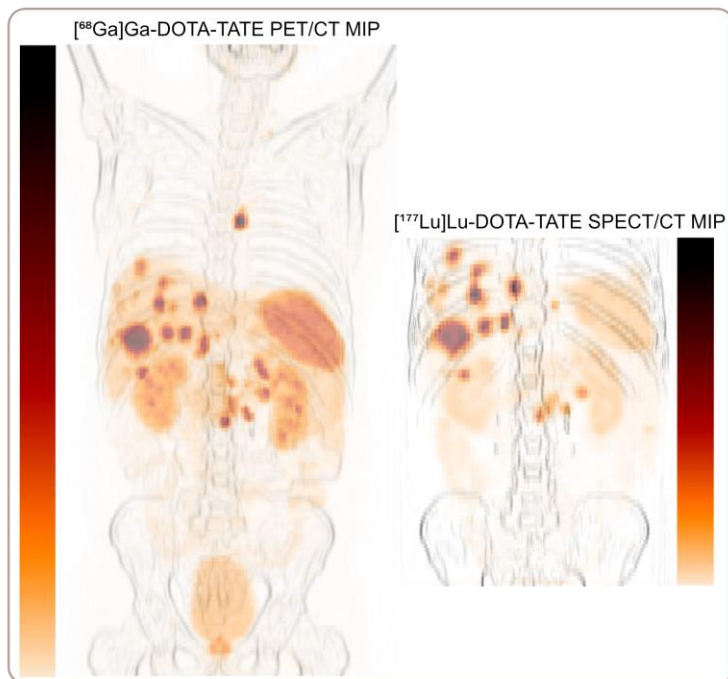


Figure 6.1. Example of a patient's coronal fused ^{68}Ga -DOTA-TATE PET/CT image acquired 1 h after injection (left) and a coronal fused ^{177}Lu -DOTA-TATE SPECT/CT image acquired 24 h after administration (right). PET and SPECT images are shown as maximum-intensity projections (MIPs) (reversed hot metal colour scale) overlaid on high-pass-filtered MIP of the CT (reversed grayscale). The FOV of the SPECT/CT image covers only parts of the multiple-FOV PET/CT. However, the kidneys and the majority of the patient's tumours are covered.²

6.1 Biodistribution of ^{68}Ga - and ^{177}Lu -SSTR analogues

The uptake of somatostatin receptor (SSTR) analogues is generally much higher in NET cells or meningioma, compared to normal tissues. Among normal organs, the highest tracer accumulation is seen in the spleen, followed by the kidneys, liver, and pituitary gland [43, 157]. The normal liver parenchyma shows moderate physiological uptake and has, in ^{111}In -Octreotide imaging, been used as a reference organ for the selection of patients suitable for ^{177}Lu -PRRT, according to the so-called Krenning index. The intensity of the lesion is visually compared with the uptake in healthy liver parenchyma, and a tumour uptake higher than the uptake in the liver and/or spleen is

² Image data were obtained from two clinical trials, Iluminet (EudraCT No 2011-000240-16, Regionala etikprövningsnämnden Lund, Dnr 2011/287), Gapetto (EudraCT No 2012-004313-13, Regionala etikprövningsnämnden Lund, Dnr 2012/657). Complementary ethics approval was obtained for inclusion of patient data acquired after the closure of Gapetto (Etikprövningsmyndigheten Verksamhetsregion Lund, Dnr 2019-00564). Written informed consent for participation in the studies was obtained from all patients. All procedures performed were in accordance with the ethical standards of the institutional and national research committee and with the principles of the 1964 Declaration of Helsinki and its later amendments.

predictive of response to PRRT [158]. However, in a recent study by G alne *et al.* [159], normal liver uptake was shown to decrease after the initialisation of treatment with long-acting somatostatin analogues. In contrast, no change in lesion uptake was seen, which may have implications for image interpretation.

Biodistribution after a bolus injection of [^{68}Ga]Ga-DOTA-TATE or -TOC has been reported after dynamic 45 min PET/CT, followed by static scans at 60, 120, and 180 minutes. The biodistribution is characterized by a fast blood clearance with only small amounts residing in blood 45 min post-injection. In healthy organs, such as the kidneys, liver, and spleen, the tracer accumulation plateaus after 50 min, but an even longer time to maximum uptake was reported for tumours [160, 161]. Illustrated in figure 6.2 are preliminary biokinetic data for tumours from a physiologically based pharmacokinetic model of [^{68}Ga]Ga DOTA-TATE and [^{177}Lu]Lu-DOTA-TATE [162, 163], based on activity quantification of 12 patients that underwent imaging with both modalities not more than 20 weeks apart. The top row shows the decay corrected activity concentration as a function of time, showing the tracers' biological uptake and elimination for ^{68}Ga (left) and ^{177}Lu (middle and right). At the time of PET imaging (1 h p.i.), most tumour uptakes have not plateaued, whereas, at the time of SPECT imaging (24 h p.i.), all tumours are in the excreting phase.

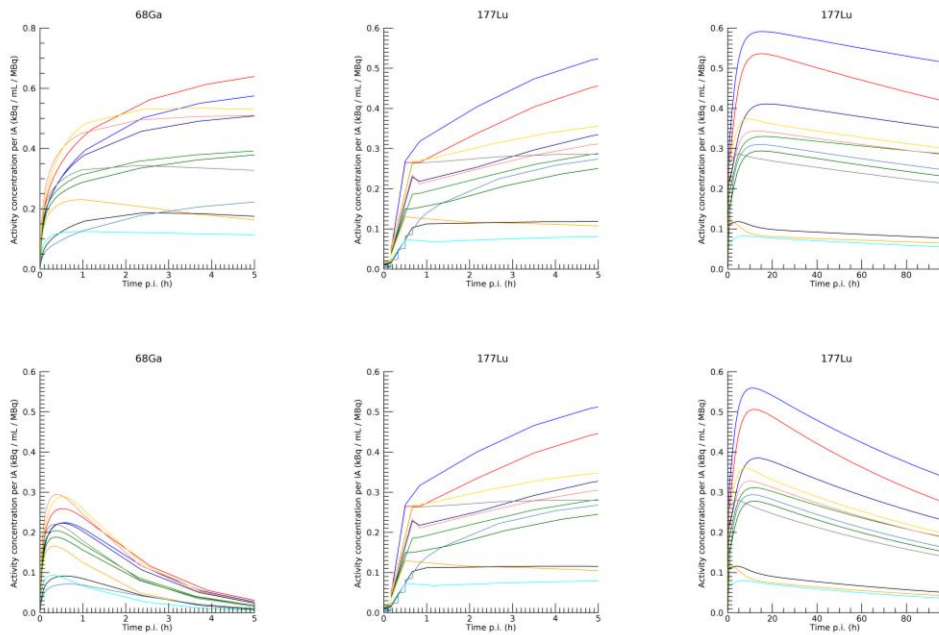


Figure 6.2. Preliminary biokinetic time-activity curves for tumours from a physiologically based pharmacokinetic model of [^{68}Ga]Ga DOTA-TATE and [^{177}Lu]Lu-DOTA-TATE [162, 163]. Illustrated is the activity concentration per injected activity for tumours as a function of time p.i. One tumour per patient (in total 12 patients, as indicated by the different colours) are included. The upper row illustrates the decay corrected activity concentration as a function of time after administration, showing the tracers' biological uptake and elimination. The lower row shows the effective biokinetics, including both biological elimination and physical decay, for [^{68}Ga]Ga-DOTA-TATE for the first 5 h p.i. (left column) and for [^{177}Lu]Lu-DOTA-TATE for the first 5 h (middle column) and first 100 h (right column) after administration.

Effective half-lives of lesions and organs can be determined from the multiple-time point imaging performed during [^{177}Lu]Lu-DOTA-TATE therapy. For the kidneys, the main organ at risk, an effective half-life of around 50 h was found for patients included in the Iluminet trial [32]. For tumours, within the same patient cohort, the effective half-lives differ depending on tumour grade, varying from 103 h for G1 and 81 h for G2 tumours [149]. Fast clearance of [^{177}Lu]Lu-DOTA-TATE from blood is demonstrated from patient measurements, with an initial half-life of 1.6 h for the first 0–24 h followed by an effective half-life of 43 h for the second phase. Data for the total body clearance show longer half-lives, 1.3 h and 50 h for the two elimination phases [164].

6.2 Application of pre-therapeutic imaging in SSTR treatment

The use of ^{68}Ga -SSTR PET imaging has recently replaced the use of ^{111}In -Octreotide SPECT imaging in peptide receptor RPT. ^{111}In -Octreotate as a surrogate imaging marker has been used for kidney dosimetry to predict toxicity for both [^{90}Y]Y-DOTA-TOC and [^{177}Lu]Lu-DOTA-TATE RPTs [165]. The advantages of ^{111}In include its high yield of gamma-rays at 171 keV (yield 0.906) and 245 keV (yield 0.941) [27], and relatively long physical half-life of 2.8 days, making it suitable for assessing pharmacokinetics for absorbed dose predictions. However, due to the two gamma rays, the lower energy window will contain down-scatter from the 245 keV gamma rays, making proper scatter correction a prerequisite for quantitative imaging [13]. Thus, the disadvantages of ^{111}In -Octreotide imaging compared to ^{68}Ga -SSTR PET in terms of lower sensitivity, poorer quantitative properties, higher radiation exposure to the patient, and a more time-consuming diagnostic procedure have led to ^{68}Ga -SSTR PET imaging becoming the method of choice [136]. The apparent image quality of ^{111}In SPECT and ^{68}Ga PET, for different sphere-to-background concentration ratios, is illustrated in Figure 6.3 (image data from **Paper III**). The detectability of the spheres in the NEMA Body phantom, in true volume ranging from a diameter of 10 mm to 37 mm, is superior in the ^{68}Ga -PET images compared to ^{111}In -SPECT images for all background ratios. For increasing background activity concentration, *i.e.*, decreasing sphere-to-background ratio, the smaller spheres are sequentially becoming non-visible. For the highest background ratio of 0.8, no spheres are visible in ^{111}In SPECT. In contrast, spheres equal to and larger than 22 mm are visible in ^{68}Ga -PET.

In **Paper III**, the quantification accuracy of ^{68}Ga PET and ^{111}In -SPECT was investigated using clinically available tools for delineation; CT-based ROIs, threshold-based ROIs and background-adapted threshold ROI (equation 5.1). For ^{111}In -SPECT images, no segmentation method gave reasonably accurate activity concentration or sphere volume results. Hence, the conclusion was that for the ^{111}In -SPECT-method in NET diagnostics, a qualitative evaluation like the Krenning index [158] is the most suitable approach.

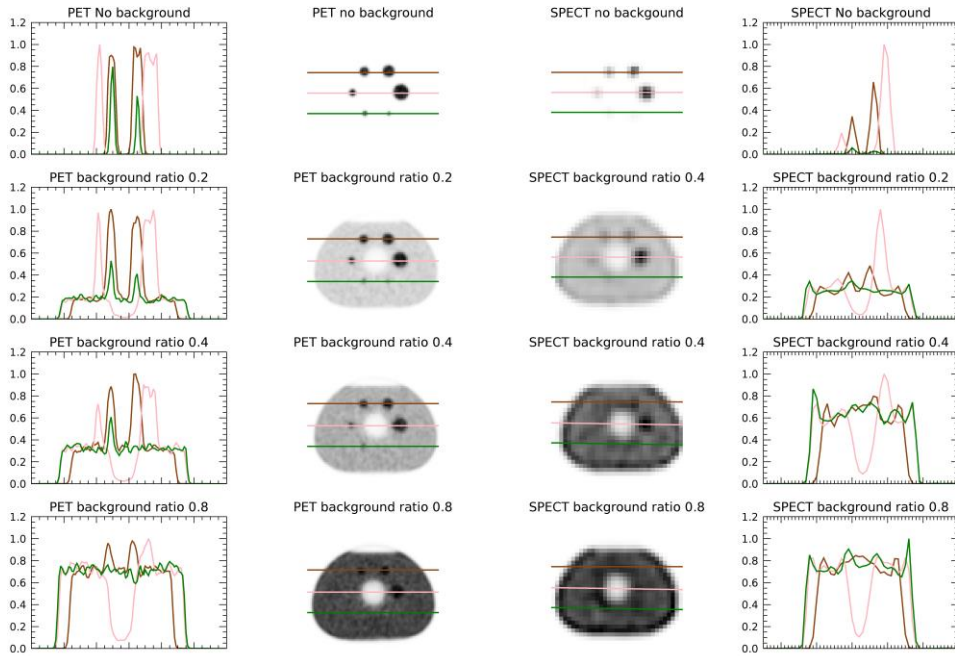


Figure 6.3. Illustration of the qualitative analysis of the ^{68}Ga -PET (left columns) and ^{111}In -SPECT images (right columns). Line profiles through the differently sized spheres (with inner diameters of 10, 13, 17, 22, 28 and 37 mm, corresponding to volumes of 0.5, 1.2, 2.6, 5.6, 11.5 and 26.5 cm^3) for background ratios of 0, 0.2, 0.4 and 0.8 are shown. The amplitude of the sphere signal is normalised to the highest signal in each image.

Concerning ^{68}Ga PET imaging, the activity quantification was more accurate and consistent. All segmentation methods gave recovery coefficients for the two largest spheres around 0.94 to 1.04 for a background ratio of 0.2. However, the two smallest spheres were underestimated for all methods ($\text{RC} = 0.40\text{-}0.82$) for a background ratio of 0.2. Generally, for all background ratios, the RCs received with the background-adapted threshold method are higher, and the spread in RCs between the threshold levels are smaller, as illustrated for background ratio of 0.4 in figure 6.4. This implies that the background-adapted thresholding results in a more robust correction, hence applying a smaller correction to the apparent activity concentration.

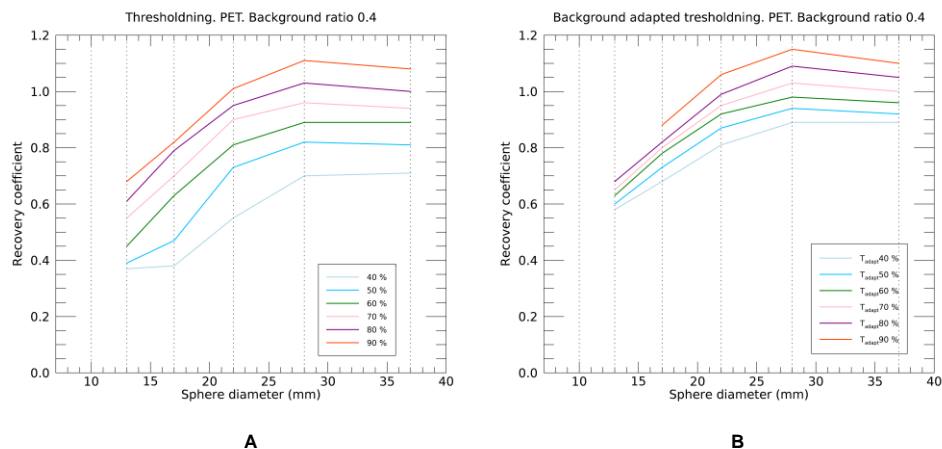


Figure 6.4. Recovery coefficients for threshold-based segmentation (A) and background-adapted thresholding (B) for ^{68}Ga PET as a function of sphere diameter for thresholds ranging from 40 % to 90 % of the maximum value. The background-adapted thresholds are calculated according to equation 5.1. Note that the 10 mm sphere is not visible (figure 6.3). The different thresholds are illustrated as differently coloured lines. The vertical dotted black lines indicate the different sphere diameters.

The quantitative accuracy of ^{18}F and ^{68}Ga from clinically reconstructed PET images of the NEMA Body Phantom with a background ratio of 0.2 was also compared. It showed an approximately 15 % lower recovery coefficient for ^{68}Ga than for ^{18}F -PET, for both CT-based ROIs and the maximum value within the spheres. One part of the deviation is due to the activity meter calibration for ^{68}Ga , which was not calibrated against a primary standard at the time. The measured (accurate) activity was retroactively discovered to be too high and later corrected by a factor of 0.94. Hence, the presented recovery coefficients for ^{68}Ga in **Paper III** are slightly too low. Later, similar deviations for ^{68}Ga were reported by others [166, 167]. Further deviation might be explained by differences in maximum positron energy and the applied correction for prompt gamma rays. The phantom measurements presented in **Paper III** [136] were further used in **Paper IV** to perform background-dependent partial volume correction of the delineated tumours.

6.3 Relationships between uptake of [^{68}Ga]Ga-DOTA-TATE and absorbed dose in [^{177}Lu]Lu-DOTA-TATE therapy

Although Gallium-68 labelled peptides are used as imaging surrogates for Lutetium-177, it is unlikely to provide accurate pre-therapeutic dosimetry estimates for the ^{177}Lu -PRRT, due to the short physical half-life of ^{68}Ga compared with the effective half-life of the ^{177}Lu -labelled peptide. However, studies have shown a concordance in lesion detectability between uptake in ^{68}Ga -PET images and absorbed doses or treatment outcomes in ^{177}Lu -PRRT [168].

Tumour SUV_{mean} or SUV_{max} , from [^{68}Ga]Ga-DOTA-TATE PET/CT exams has been demonstrated to correlate with lesion absorbed doses in NET [169] and meningioma patients [170] and has also been used as a predictor of therapy response [171]. In a study by Krebs *et al.* [172], investigating paired imaging with an SSTR antagonist, a modest correlation between ^{68}Ga - SUV_{peak} and absorbed dose to lesions in the ^{177}Lu -SSTR therapy was seen. Since SUV values differ between scanners and reconstruction parameters, a site-independent cut-off of a tumour-to-liver, tumour-to-spleen or tumour-to-blood SUV ratio has been suggested [153, 171, 173], where changes in the tumour-to-spleen ratio were a better predictor of therapy outcome than differences in tumour SUV_{max} .

In **Paper IV** the relationship between uptake of [^{68}Ga]Ga-DOTA-TATE quantified in PET images and activity uptake in and absorbed dose to organs and tumours during subsequent treatment with [^{177}Lu]Lu-DOTA-TATE for NETs was investigated. This investigation can be made from different perspectives. Generally, relationships are approached on a population level, reflecting the overall relationship across patients. For metastatic disease, analyses can also be made across the tumours within individual patients, *i.e.*, whether a higher uptake of [^{68}Ga]Ga-DOTA-TATE in one tumour than another within the same patient generally means that the absorbed dose is higher for that tumour in [^{177}Lu]Lu-DOTA-TATE therapy. Separate analyses were made of between-patient and within-patient correlations, using weighted correlation coefficients and repeated-measures correlations, respectively, as suggested by Bland and Altman [174, 175]. This study presented in **Paper IV** aimed to investigate between- and within-patient relationships for tumours and between-patient relationships for organs.

Studies that have compared the activity uptakes in ^{68}Ga -SSTR-PET/CT with the uptakes and absorbed doses in ^{177}Lu -PRRT have mainly used different variants of SUV for evaluation of the ^{68}Ga images. However, a simpler and more fundamental parameter than SUV is the activity concentration. Although SUV is well established as a metric in diagnostics and patient selection from ^{68}Ga -SSTR-PET/CT, the reasons for using SUV are less evident when attempting to find a relationship to the therapeutic absorbed dose from ^{177}Lu . Specifically, the inclusion of the patient's weight can be questioned, as used in the calculation of SUV, as the weight does not enter the calculation of the absorbed dose to tumours and organs. Besides SUV, different tumour-to-tissue ratios have been proposed, which partly is methodologically motivated, as this may partly mitigate the SUV dependence on factors such as reconstruction settings, the PET/CT system, and the accumulation time [152].

To summarize the results from **Paper IV**, for tumours, we see a significant but moderately strong relationship between patients with respect to the absorbed dose from ^{177}Lu -PRRT and the activity concentration measured in ^{68}Ga -PET images both with respect to between-patients ($r = 0.7$) and within-patients ($r = 0.4$) analyses. However, a stronger relationship is seen with respect to ^{177}Lu activity uptake measured from SPECT images 24 h after injection, both with respect to between-patients

($r = 0.9$) and within-patients ($r = 0.8$) analyses. So, to conclude, within a given patient, the variation in ^{68}Ga uptakes between tumours generally also translated to a difference in ^{177}Lu uptakes and absorbed doses.

Interestingly, this study provides no support for any type of normalization of the ^{68}Ga activity concentration to improve the relationship to absorbed dose in ^{177}Lu -PRRT, either with respect to normalization to body weight, *i.e.*, calculation of SUV, or with respect to normalization to a reference tissue. However, in this study, SUVs were calculated according to clinical practice, with no recovery coefficient applied, which may in part affect the correlations obtained.

One proposed approach to predict therapy absorbed doses, recently shown for PSMA ligand imaging and therapy [176], is to use pre-therapeutic activity concentrations quantified in the ^{68}Ga -PET/CT, and effective half-lives derived from intra-therapeutic imaging. In our case, tumour absorbed doses were estimated from ^{68}Ga PET activity concentration, propagating it back to the concentration at $t = 0$, assuming a mono-exponential time-activity curve with effective half lives of 103 h and 81 h, for grade-1 and grade-2 tumours, respectively, derived from the same patient population and presented in Roth *et al.* [149]. The corresponding ^{177}Lu -activity concentration was calculated by scaling from the ^{68}Ga activity concentration at $t = 0$, scaled to the injected respective injected activities. The absorbed doses were calculated assuming local deposition of energy emitted as charged particles from ^{177}Lu .

Comparing the ^{68}Ga -derived absorbed doses to the absorbed doses measured at therapy showed a mean deviation of the ^{68}Ga -based estimates being 11 % higher than the absorbed doses measured at therapy, with a 95 % coverage interval of -65 % to 248%. In practice, this means that the absorbed dose in tumours can be predicted based on ^{68}Ga within approximately a factor of 2. Thus, a good correlation as seen between ^{68}Ga activity concentration and ^{177}Lu absorbed dose, does not necessarily make one parameter a good predictor of the other. The results indicate that ^{68}Ga -PET activity uptake in combination with a population mean values can give a rough idea of the absorbed doses in upcoming therapy. Treatment planning based on pre-therapeutic imaging will require more input information or a more refined modelling approach, such as physiologically-based pharmacokinetic modelling.

7 Summary of papers

Paper I: A small-scale anatomical dosimetry model of the liver

In Paper I, a small-scale dosimetry model of liver microarchitecture was developed. The aim was to produce dosimetry reference data according to MIRD schema, for internal irradiation within the liver tissue, where the distribution of radionuclides or radiopharmaceuticals is inhomogeneously distributed. Monte Carlo simulations were used to determine specific absorbed fractions and S values for monoenergetic electrons, photons, alpha particles, and some clinically used radionuclides; ^{125}I , ^{90}Y , ^{211}At , $^{99\text{m}}\text{Tc}$, ^{111}In , ^{177}Lu , ^{131}I and ^{18}F . The ratio between the small-scale and whole-organ average absorbed dose was presented, giving conversion factors from macro to small-scale absorbed dose determination. The results showed that absorbed doses within the hepatic tissues might vary considerably between different target cells, because of heterogeneously distribution. As an example, uptake of radionuclides emitting low-energy electrons (*e.g.* ^{125}I) or high-LET alpha particles (*e.g.* ^{211}At) in Kupffer cells results in a local absorbed dose for part of the space of Disse (*i.e.* the space between hepatocytes and endothelial cells of the sinusoid), of eight- and five-fold the average absorbed dose to the whole liver, respectively. The overall results indicate the importance of internal dosimetry improvements at small-scale anatomical levels.

Paper II: Quantitative γ -H2AX immunofluorescence method for DNA double-strand break analysis in testis and liver after intravenous administration of $^{111}\text{InCl}_3$

In Paper II, an experimental method for *ex vivo* detection and quantification of γ -H2AX foci, a surrogate marker for a DNA double-strand break, from $^{111}\text{InCl}_3$ *in vivo* irradiated tissue sections from mice was developed. The method includes advanced immunofluorescence labelling and confocal laser scanning microscopy imaging followed by quantitative image analysis. The method was applied to the testis and liver, representing two quite different radiosensitive tissues. Biopsies were extracted at two different timepoints after injection. The developed method was found to work well for both tissues. The results revealed an elevation of γ -H2AX foci in liver cells after exposure, measured for both hepatocytes and non-hepatocytes. However, no significant difference was seen for the spermatogonia or primary spermatocytes from the testis tissue at either point after injection. The analysis demonstrated an absorbed dose-dependent elevation of γ -H2AX foci after internal exposure of the liver cells. The results indicate that a lower endogenous level of γ -H2AX foci and a higher absorbed

dose, as seen in the liver compared to the testis, lead to increased separation between exposed and non-exposed animals.

Paper III: Quantitative analysis of phantom studies of ^{111}In and ^{68}Ga imaging of neuroendocrine tumours

In Paper III, differences in image quality and accuracy in activity quantification for ^{111}In SPECT and ^{68}Ga PET images were investigated through phantom measurements of the NEMA ICE Body phantom. The sphere to background concentration was varied from no background activity to a sphere to background ratio of 1.25:1, to mimic clinically relevant lesion-to-background ratios. Images were acquired using clinical acquisition and reconstruction protocols, and the activity concentration and sphere volume was segmented using CT-based, threshold-based, and background-adapted threshold delineation. The results showed that sphere diameter and background activity concentration strongly affect the possibility of accurate quantification. Gallium-68 PET/CT imaging showed superiority compared to ^{111}In SPECT/CT imaging both concerning detection of smaller lesions and higher accuracy in the quantification of activity in and the volume of a lesion. For ^{111}In SPECT images, no quantification method gave accurate results for neither activity concentration nor the volume of the spheres. For ^{68}Ga PET images, the activity concentration of spheres with a diameter larger than 17 mm could be accurately determined using the value of maximum activity concentration in the VOI. A threshold of around 40% gave an acceptable accuracy of sphere volume for a higher sphere-to-background ratios.

Paper IV: The relationship between uptake of [^{68}Ga]Ga-DOTA-TATE and absorbed dose in ^{177}Lu peptide receptor radionuclide therapy

In Paper IV, the relation between uptakes of [^{68}Ga]Ga-DOTA-TATE quantified in pre-therapeutic PET images, and uptakes and absorbed doses to tumours and organs during subsequent treatment with [^{177}Lu]Lu-DOTA-TATE for NETs was investigated. The dosimetry was performed using a hybrid planar-SPECT/CT method, including Monte Carlo-based voxel-wise absorbed dose rate calculation and partial volume correction. Furthermore, the possibility to predict the tumour absorbed doses for therapy was explored, based on tumour-specific ^{68}Ga activity concentrations and group-based estimates of the effective half-lives for grade 1 and 2 NETs. Only the spleen showed a significant correlation between the ^{68}Ga activity concentrations and ^{177}Lu absorbed doses among the organs. For tumours, a significant but moderately strong relationship was seen between the activity concentration measured in ^{68}Ga -PET images and the absorbed dose in ^{177}Lu -PRRT. However, the relationship with respect to the ^{177}Lu activity concentration measured in SPECT images 24 h after injection was stronger. The results provide no support for using different normalizations of ^{68}Ga activity concentration to improve the relationship to absorbed dose in ^{177}Lu -PRRT, neither with respect to normalization to body weight, *i.e.*, calculation of SUV, nor with respect to a reference tissue. The ability to predict the ^{177}Lu absorbed dose to tumours based solely on a ^{68}Ga -PET image is limited and the therapeutic absorbed dose to tumours can be predicted within approximately a factor of 2.

8 Concluding remarks and future directions

Radiation exposure in nuclear medicine procedures is diverse in terms of radiation quality, absorbed dose rate, and spatial distribution of the absorbed dose, and differs considerably between diagnostic and therapeutic radiopharmaceuticals. Thus, determining the absorbed dose to tissues or an organ at the cellular or sub-cellular level is a prerequisite to establishing a dose–effect relationship for the radiopharmaceutical therapy (RPT) outcome or normal tissue toxicity. The accuracy of the absorbed dose determination is a double-sided problem, which depends on the method used for the activity quantification and the model used for the radiation transport process.

The four studies on which this thesis is based have investigated quantitative methods within the field of nuclear medicine internal dosimetry and radiobiology. The studies have provided methods for more detailed quantification of activity concentration, absorbed dose and absorbed dose distribution and the resulting biological effect. Methods providing a deeper understanding of the biological effect, in combination with a more accurate activity concentration quantification and absorbed dose determination, is the basis for a more refined absorbed dose-effect relationship after internal irradiation.

In **Paper I**, a sophisticated organ dosimetry model was developed using a Monte Carlo method to simulate the radiation transport through the model in order to determine microarchitecture absorbed dose conversion factors (S values). The results enlighten the importance of internal dosimetry calculations beyond the traditional average absorbed dose to organs at risk, especially in RPT. In small-scale dosimetry, the traditional organ level is subdivided into several subregions. Individual cellular structures can serve as source and target regions, and their geometric dimensions are comparable to the range of emitted alpha particles, beta particles, and low-energy electrons. As a result, this allows for absorbed dose calculations on a scale comparable to the range of emitted particles without abandoning general MIRD. However, when the dimensions of the model geometry no longer can be considered large compared to the electron range, the demands on the electron transport calculation increase to calculate an accurate absorbed dose. Furthermore, there is an increased need for an even more realistically defined anatomical geometry to compute the absorbed dose to the radiobiologically interesting target with satisfactory accuracy.

For the generated small-scale dosimetry S values, as a part of **Paper I**, to be useful, the cumulated activity within the defined source regions must be estimated. Hence, the activity distribution and biokinetics must be obtained on the spatial scale of the model. Due to the limited spatial resolution of clinical imaging systems, the non-uniformity of the activity distribution for small-scale dosimetry needs to be determined from *ex vivo* autoradiography of tissue sections from human or animal biopsies. Another approach to account for the small-scale distribution of activity and absorbed dose could be a combination of clinical imaging, compartment modelling, and small-scale dosimetry models [177].

One way to improve our understanding of the relationship between absorbed dose and biological effect is through experimental radiobiological techniques. In **Paper II**, an experimental *ex vivo* method was developed to visualize and quantify γ H2AX foci, a surrogate marker for DNA DSB, within *in vivo* systemically irradiated organs from mice. The method is potentially applicable to study and establish dose-effect relationships in different differentiated tissues during internal irradiation. Similar methods for quantifying DNA DSB have been applied to *in vivo*, and *ex vivo* irradiated blood cells [44, 105-109] which have been suggested could act as biological dosimeters. Also, targeting the DNA damage response signal for PET and SPECT imaging has been proposed [178], where *in vivo* imaging of γ H2AX expression could be used for therapy determination by monitoring DSBs caused by chemo- or radiotherapy.

For dosimetry to be a relevant predictor of a biological endpoint, it must be accurate. The non-uniform tissue distribution of radiopharmaceuticals or radionuclides is an important factor to consider when predicting the biological effects of radiopharmaceutical therapy. In **Paper II**, the fraction of locally absorbed dose to the organ's average absorbed dose for ^{111}In is discussed in relation to results extracted from the human small-scale dosimetry model presented in **Paper I**. The local absorbed dose close to the source region, the Kupffer cells, would increase slightly (5–10%) for 10% of the hepatocytes. Thus, the self-absorbed dose to Kupffer cells was determined to be 25 times the average organ-absorbed dose.

In contrast to fractionated external radiotherapy, in which the time between fractions is long enough to allow for the complete repair of sublethal damages, the absorbed dose in RPTs is delivered continuously due to prolonged retention of the radioactive agent. Hence, the number of DNA DSB foci per cell at a specific time will depend on the absorbed dose rate in combination with the rate of DNA repair. Therefore, the number of DNA DSB foci will be a function of time, and the measurement time-point will only show a momentaneous value. The biological effect of radiation is ultimately an effect at the cellular level, which makes dose-effect relationships challenging to establish due to the non-uniformity of the deposited energy. Hence, further development of pre-clinical and experimental radiobiology and dosimetry models is needed to fully understand the relationship between absorbed dose and biological effect. And as our understanding of the relationship evolves, so will our development of dosimetry and radiobiological models.

Regardless of the spatial scale, the source region activity quantification is an important step in internal dosimetry due to the linear relationship between the time-integrated activity and the absorbed dose. Activity quantification from imaging data is affected by the selected imaging parameters, methods for image reconstruction, compensation for image-degrading effects, the calibration methods used for absolute quantification from images, and the segmentation method. The poor spatial resolution of the clinical imaging systems, the SPECT and PET camera, is an important factor for both **Paper III** and **Paper IV**, affecting both the target delineation and the activity quantification [179].

Quantitative nuclear medicine imaging is the basis for dosimetry in radiopharmaceutical therapy. For the absorbed dose estimation to different structures to be reliable, the segmentation method must be robust and accurate in determining the object border, which determines the object volume and the subsequent activity concentration. In **Paper III**, the accuracy of quantification of images acquired with the clinically used acquisition and reconstruction parameters was investigated. In recent years, the demand for quantitative ^{111}In -SPECT images has decreased considerably, and the ^{68}Ga -labelled SSTR analogues are today the dominant radiopharmaceutical for diagnostic NET imaging. The results of **Paper III** showed that the presence or absence of background activity needs to be accounted for when determining the recovery, due to the spill-out of object signal and the spill-in from background signal, which will affect the recovery for a specific segmentation method. In **Paper IV**, the Fourier surface method for segmentation was used to delineate tumours in both PET and SPECT images. The method has been thoroughly validated for ^{177}Lu -SPECT images [137] and was harmonized for the PET images using the phantom data from **Paper III**.

For nuclear medicine imaging and therapy—or theragnostics—of neuroendocrine tumours, the relationship between the uptake of ^{68}Ga]Ga-DOTA-TATE and the uptake and absorbed dose of ^{177}Lu]Lu-DOTA-TATE was investigated in **Paper IV**. The radiopharmaceuticals are an accepted theragnostic pair, but the relationship between the activity uptakes observed at ^{68}Ga PET imaging and absorbed doses at subsequent ^{177}Lu therapy is still little investigated and relatively poorly understood.

Similar comparison studies investigating the relationship between the activity uptakes in ^{68}Ga -SSTR-PET/CT with the uptakes and absorbed doses in ^{177}Lu -PRRT have mainly used different variants of SUV or different tumour-to-tissue ratios for evaluation of the ^{68}Ga images [169, 170, 172]. Although SUV is well established as a metric in diagnostic ^{18}F]FDG PET imaging, it is less evident for ^{68}Ga -SSTR-PET imaging and when attempting to find a relationship to the therapeutic absorbed dose from ^{177}Lu . Interestingly, the relationship presented in **Paper IV** did not improve when normalization of the activity concentration was used, neither with respect to normalization of body weight, *i.e.* calculation of SUV, nor with respect to reference tissue. However, for the simpler and more fundamental parameter activity concentration per administered activity, the relation to absorbed dose from ^{177}Lu increased. The result from the study also showed a stronger correlation between ^{68}Ga

and ^{177}Lu activity concentrations compared to the ^{177}Lu absorbed dose. This was an expected result since the absorbed dose depends on a combination of initial activity uptake and excretion, whereas the activity concentration measured in ^{68}Ga -PET at 1h almost exclusively reflects initial activity uptake.

An essential requirement for treatment planning in RPT is the in-advance estimate of the therapeutic absorbed dose. Based on the approach presented in **Paper IV**, using the ^{68}Ga -PET activity concentration combined with population-based effective half-lives for [^{177}Lu]Lu- DOTA-TATE for NETs only gave an estimate within about a factor of two of the absorbed doses in the upcoming therapy. This, even though a moderately strong correlation at the group level was found between the ^{68}Ga activity concentration and the ^{177}Lu absorbed dose. Therefore, personalised treatment planning for RPT of NETs will require more elaborate approaches, such as pharmacokinetic modelling, where patient-specific parameters can be considered [180]. Physiologically-based pharmacokinetic models that describe the distribution, binding, internalization, and degradation of the sst2 receptor targeting peptide used have been developed for DOTA-TATE [162, 163] and PSMA [181] treatment planning. In such models, differences in administration protocols between pre-therapeutic and therapeutic administrations, tumour burden, and kidney filtration rates can be considered. Further developments are needed, where modern quantitative imaging techniques for ^{177}Lu are applied. Machine learning techniques are an alternative solution for dosimetry prediction based on pre-therapy PET imaging [182].

To fully identify the importance of dosimetry and radiobiology in nuclear medicine, dosimetry-guided patient-specific treatment planning of RPT will need to be proven beneficial through studies showing a long-term survival benefit or a decrease in treatment-related toxicity. The innate characteristic of RPT, the heterogeneity of absorbed dose distribution, demands the establishment of methods for local absorbed dose calculation, together with the integration of dose rate effects and the individual DNA repair capacity, in order to find relationships to different bioeffective measures. To further understand the biological effects of RPT on tissues, radiobiological methods to identify and quantify intracellular signalling, interactions within the microenvironment, and the bystander effect must be established. It is expected that radiobiology will play an important role in optimizing the benefits of therapeutic radiopharmaceuticals and exploiting the capabilities of new nuclear medicine applications for each individual patient. Hence, dosimetry and radiobiology should be integrated into all stages of development and the individualization of new and present radiopharmaceutical therapies. The four studies on which this thesis is based have all presented novel results within the field of nuclear medicine dosimetry and radiobiology research.

Measure what is measurable and make measurable what is not so.

Galileo Galilei

Acknowledgements

There are many people to whom I would like to express my gratitude, from whom I have received help and support during my time as a PhD student. I would like to thank all of you, and in particular:

My main supervisor *Bo-Anders Jönsson*. Thank you for, first of all, encouraging me to trust in the application process for the Medical Radiation Physics program; I didn't move to Lund in vain! I would also like to thank you for introducing me to the field of internal dosimetry and for encouraging me to perform experimental research. But mostly, I would like to thank you for also showing value in things non-academic. That has made me feel less weird.

My supervisor *Erik Larsson*. Thank you for your patience and endless support. And I mean it! Thanks for your invaluable knowledge and skill in radiation physics and programming—you have saved me many times—and thanks for always being there, even in the last minute!

My supervisor *Katarina Sjögren Gleisner*. Thanks for 'adopting' me halfway through my PhD and for introducing me to the field of clinical dosimetry. I would also like to thank you for being a true role model in academia; your wise approach in numerous situations has been invaluable.

My supervisor *Bo Baldetorp*. Thank you for always believing in me and for your never-ending optimism.

My co-authors, for providing your expertise. I would like to express a special thanks to:

Lena Jönsson. Thank you for your endless knowledge in the field of nuclear medicine and your support and encouragement in research and clinical work. And thanks for sharing and thanks for caring!

Johan Gustafsson. Thank you for your tireless support and for always finding solutions to the most, for me, unsolvable problems. Thank you for your invaluable collaboration.

Sven-Erik Strand. Thank you for your never-ending enthusiasm. You are a true inspiration.

Bo Holmqvist. Halloj! and thank you for being my mentor in the world of biology and microscopes. But mostly, I would like to thank you for being, if so involuntarily, a mentor in the world of academia and in life in general.

My former and present friends and colleagues at the Department of Medical Radiation Physics in Lund, with special thanks to the past and present Nuclear Medicine group.

My former and present friends and colleagues at the Radiation Physics department, Nuclear Medicine and Clinical Physiology department and Radionuclide Therapy department at Skåne University Hospital. I would also like to express my gratitude to my former colleagues at the Cyclotron facility; thanks for being early bird friends and for the unforgettable and unexpected knowledge these mornings have given me!

Anneli Edwardsson, for the pleasure and lifesaving of sharing office space with you during my early years as a PhD-student.

My former classmates in the Medical Radiation Physics program for being invaluable during the sometimes struggling, but mostly extraordinary fun times, of our education. Without you, I wouldn't be a medical physicist, and I wouldn't have the best of friends!

My family and friends. Thank you for all your love and unconditional support.

Alva and *Eira*, my dear daughters, thank you for unknowingly joining this journey. Even with minimal sleep, I become a better person everyday thanks to you! And yes, the same goes for you *Cruz*!

Finally. Thank you, *Johan*, for bringing love and joy to my life. Thanks for enduring, even during the most desperate times of this long journey. I love you!

Support for this work was granted by the Swedish Cancer Society, the Berta Kamprad foundation, and the Gunnar Nilsson foundation.

References

1. Virgolini, I., et al., Procedure guidelines for PET/CT tumour imaging with 68Ga-DOTA-conjugated peptides: 68Ga-DOTA-TOC, 68Ga-DOTA-NOC, 68Ga-DOTA-TATE. *Eur J Nucl Med Mol Imaging*, 2010. **37**: p. 2004-2010.
2. Council of the European Union. European Council directive 2013/59/Euratom on basic safety standards for protection against the dangers arising from exposure to ionising radiation and repealing directives 89/618/Euratom, 90/641/Euratom, 96/29/Euratom, 97/43/Euratom and 2003/122/Euratom. *Off J Eur Union.*, 2014: p. L13:11–73.
3. ICRU, Fundamental Quantities and Units for Ionizing Radiation. Report 85. Volume 11. No 1. 2011.
4. Sgouros, G., et al., MIRD Pamphlet No. 22 (abridged): radiobiology and dosimetry of alpha-particle emitters for targeted radionuclide therapy. *J. Nucl. Med.*, 2010. **51**: p. 311-328.
5. UNSCEAR 2012 REPORT, Sources ,effects and risk of ionizing radiation - UNSCEAR 2012 Report -Report to the General Assembly, with Scientific Annexes A and B.
6. ICRP, ,2012 ICRP Statement on Tissue Reactions / Early and Late Effects of Radiation in Normal Tissues and Organs – Threshold Doses for Tissue Reactions in a Radiation Protection Context. *Ann. ICRP*, 2012. **41**: p. 1-322.
7. SSM., Swedish Radiation Safety Authority. 2022 Available from: <https://dosreg.ssm.se/Isotopstatistik/RegistreringPublik>.
8. ICRP, 1988. Radiation Dose to Patients from Radiopharmaceuticals. ICRP Publication 53. *Ann. ICRP* 18 (1-4).
9. ICRP, 1998. Radiation Dose to Patients from Radiopharmaceuticals (Addendum to ICRP Publication 53). ICRP Publication 80. *Ann. ICRP* 28 (3).
10. ICRP, 2008. Radiation Dose to Patients from Radiopharmaceuticals - Addendum 3 to ICRP Publication 53. ICRP Publication 106. *Ann. ICRP* 38 (1-2).
11. Cristy, M. and K. Eckerman, Specific Absorbed Fractions of Energy at Various Ages for Internal Photon Sources. Oak Ridge, TN: Oak Ridge National Laboratory. 1987 p. ORNL/TM-8381.
12. SSM., Swedish Radiation Safety Authority. Last updated 2021-02-12; Available from: <https://www.stralsakerhetsmyndigheten.se/omraden/stralning-i-varden/doskatalog/>.
13. Sgouros, G.B., W. E.; Chiti, A.; Dewaraja, Y. K.; Emfietzoglou, D.; Hobbs, R. F.; Konijnenberg, M.; Sjögren-Gleisner, K.; Strigari, L.; Yen, T.-C.; Howell, R. W., ICRU REPORT 96, Dosimetry-Guided Radiopharmaceutical Therapy. *Journal of the ICRU*, 2021. **Vol. 21(1)**: p. 1–212.
14. Konijnenberg, M., et al., EANM position paper on article 56 of the Council Directive 2013/59/Euratom (basic safety standards) for nuclear medicine therapy. *Eur J Nucl Med Mol Imaging*, 2021. **48**: p. 67-72.
15. Poeppel, T.D., et al., EANM guideline for radionuclide therapy with radium-223 of metastatic castration-resistant prostate cancer. *Eur J Nucl Med Mol Imaging*, 2018. **45**: p. 824-845.
16. Bodei, L., et al., The joint IAEA, EANM, and SNMMI practical guidance on peptide receptor radionuclide therapy (PRRT) in neuroendocrine tumours. *Eur J Nucl Med Mol Imaging*, 2013. **40**: p. 800-816.
17. Sartor, O., et al., Lutetium-177-PSMA-617 for Metastatic Castration-Resistant Prostate Cancer. *N. Engl. J. Med.*, 2021. **385**: p. 1091-1103.
18. Lassmann, M., et al., Dosimetry for Radiopharmaceutical Therapy: The European Perspective. *J. Nucl. Med.*, 2021. **62**: p. 73S-79S.

19. Strigari, L., et al., The evidence base for the use of internal dosimetry in the clinical practice of molecular radiotherapy. *Eur. J. Nucl. Med. Mol. Imag.*, 2014. **41**: p. 1976-1988.
20. Garin, E., et al., Personalised versus standard dosimetry approach of selective internal radiation therapy in patients with locally advanced hepatocellular carcinoma (DOSISPHERE-01): a randomised, multicentre, open-label phase 2 trial. *Lancet Gastroenterology & Hepatology*, 2021. **6**: p. 17-29.
21. Sjögreen Gleisner, K.S., et al., Variations in the practice of molecular radiotherapy and implementation of dosimetry: results from a European survey. *Ejnmmi Physics*, 2017. **4**.
22. Wahl, R.L. and J. Sunderland, *Radiopharmaceutical Dosimetry for Cancer Therapy: From Theory to Practice*. *J. Nucl. Med.*, 2021. **62**: p. 1S-2S.
23. Krenning, E.P., et al., Somatostatin receptor scintigraphy with indium-111-DTPA-D-Phe-1-octreotide in man: metabolism, dosimetry and comparison with iodine-123-Tyr-3-octreotide. *J. Nucl. Med.*, 1992. **33**: p. 652-658.
24. Krenning, E.P., et al., Somatostatin receptor scintigraphy with [111In-DTPA-D-Phe1]- and [123I-Tyr3]-octreotide: the Rotterdam experience with more than 1000 patients. *Eur. J. Nucl. Med.*, 1993. **20**: p. 716-731.
25. Krenning, E.P., et al., Radiotherapy with a Radiolabeled Somatostatin Analog, [in-111-Dtpa-D-Phe(1)]-Octreotide. *Molecular and Cell Biological Aspects of Gastroenteropancreatic Neuroendocrine Tumor Disease*, 1994. **733**: p. 496-506.
26. Teunissen, J.J., et al., Nuclear medicine techniques for the imaging and treatment of neuroendocrine tumours. *Endocr Relat Cancer*, 2011. **18 Suppl 1**: p. S27-51.
27. Bé, M.-M., et al., *Table of Radionuclides*. Monographie BIPM-5. Vol. 3. 2006, Sévres, France: Bureau International des Poids et Mesures.
28. Berger, M.J., et al. *Stopping-Power and Range Tables for Electrons, Protons, and Helium Ions*. NIST Standard Reference Database 124. July 2017; Available from: <http://www.nist.gov/pml/data/star/index.cfm>.
29. Bé, M.-M., et al., *Table of Radionuclides*. Monographie BIPM-5. Vol. 2. 2004, Sévres, France: Bureau International des Poids et Mesures.
30. Bodei, L., et al., Long-term evaluation of renal toxicity after peptide receptor radionuclide therapy with Y-90-DOTATOC and Lu-177-DOTATATE: the role of associated risk factors. *Eur. J. Nucl. Med. Mol. Imag.*, 2008. **35**: p. 1847-1856.
31. Strosberg, J., et al., Phase 3 Trial of (177)Lu-Dotatate for Midgut Neuroendocrine Tumors. *N. Engl. J. Med.*, 2017. **376**: p. 125-135.
32. Sundlöv, A., et al., Individualised Lu-177-DOTATATE treatment of neuroendocrine tumours based on kidney dosimetry. *Eur. J. Nucl. Med. Mol. Imag.*, 2017. **44**: p. 1480-1489.
33. Sundlöv, A., et al., Phase II trial demonstrates the efficacy and safety of individualized, dosimetry-based Lu-177-DOTATATE treatment of NET patients. *Eur. J. Nucl. Med. Mol. Imag.*, 2022. **49**: p. 3830-3840.
34. Giammarile, F., et al., EANM procedure guideline for the treatment of liver cancer and liver metastases with intra-arterial radioactive compounds. *Eur. J. Nucl. Med. Mol. Imag.*, 2011. **38**: p. 1393-1406.
35. Welsh, J.S., A.S. Kennedy, and B. Thomadsen, Selective Internal Radiation Therapy (SIRT) for liver metastases secondary to colorectal adenocarcinoma. *Int. J. Radiat. Oncol. Biol. Phys.*, 2006. **66**: p. S62-73.
36. Wahl, R.L., et al., Normal-Tissue Tolerance to Radiopharmaceutical Therapies, the Knowns and the Unknowns. *J. Nucl. Med.*, 2021. **62**: p. 23S-35S.
37. Sgouros, G., et al., Tumor Response to Radiopharmaceutical Therapies: The Knowns and the Unknowns. *J. Nucl. Med.*, 2021. **62**: p. 12S-22S.
38. Emami, B., et al., Tolerance of normal tissue to therapeutic irradiation. *Int. J. Radiat. Oncol. Biol. Phys.*, 1991. **21**: p. 109-122.
39. Marks, L.B., et al., Use of normal tissue complication probability models in the clinic. *Int. J. Radiat. Oncol. Biol. Phys.*, 2010. **76**: p. S10-19.
40. Reilly, R.M., et al., Problems of delivery of monoclonal antibodies. *Pharmaceutical and pharmacokinetic solutions*. *Clin. Pharmacokinet.*, 1995. **28**: p. 126-142.

41. Tennvall, J., et al., EANM procedure guideline for radio-immunotherapy for B-cell lymphoma with 90Y-radiolabelled ibritumomab tiuxetan (Zevalin). *Eur J Nucl Med Mol Imaging*, 2007. **34**: p. 616-622.
42. Hindie, E., et al., Microautoradiographic study of technetium-99m colloid uptake by the rat liver. *J. Nucl. Med.*, 1988. **29**: p. 1118-1121.
43. Sjögreen Gleisner, K., et al., EANM dosimetry committee recommendations for dosimetry of 177Lu-labelled somatostatin-receptor- and PSMA-targeting ligands. *Eur J Nucl Med Mol Imaging*, 2022. **49**: p. 1778-1809.
44. Eberlein, U., et al., DNA damage in blood lymphocytes in patients after (177)Lu peptide receptor radionuclide therapy. *Eur J Nucl Med Mol Imaging*, 2015. **42**: p. 1739-1749.
45. Denoyer, D., et al., Analysis of 177Lu-DOTA-octreotate therapy-induced DNA damage in peripheral blood lymphocytes of patients with neuroendocrine tumors. *J. Nucl. Med.*, 2015. **56**: p. 505-511.
46. Stenvall, A., et al., A small-scale anatomical dosimetry model of the liver. *Phys. Med. Biol.*, 2014. **59**: p. 3353-3371.
47. Jönsson, B.A., S.E. Strand, and B.S. Larsson, A quantitative autoradiographic study of the heterogeneous activity distribution of different indium-111-labeled radiopharmaceuticals in rat tissues. *J. Nucl. Med.*, 1992. **33**: p. 1825-1833.
48. ICRU, Absorbed-dose Specification in Nuclear Medicine, ICRU Report No 67. 2002, Ashford, UK: Nuclear Technology Publishing.
49. Gardin, I., et al., Dosimetry at the cellular level of Kupffer cells after technetium-99m-sulphur colloid injection. *J. Nucl. Med.*, 1992. **33**: p. 380-384.
50. De Jong, M., et al., Inhomogeneous localization of radioactivity in the human kidney after injection of [(111)In-DTPA]octreotide. *J. Nucl. Med.*, 2004. **45**: p. 1168-1171.
51. Konijnenberg, M., et al., Radiation dose distribution in human kidneys by octreotides in peptide receptor radionuclide therapy. *J. Nucl. Med.*, 2007. **48**: p. 134-142.
52. Jönsson, B.-A., et al., Tissue, cellular, and subcellular distribution of indium radionuclides in the rat, in *Biophysical Aspects of Auger Processes*, AAPM Symposium Series No. 8. 1992, American Institute of Physics: Woodbury, NY. p. 249-272.
53. Jönsson, B.-A., Biokinetics and localization of some In-111-radiopharmaceuticals in rats at the macroscopic and microscopic level - An approach towards small scale dosimetry [Doctoral Thesis]. Lund University, 1991. **Lund**.
54. Oakberg, E.F., A Description of Spermiogenesis in the Mouse and Its Use in Analysis of the Cycle of the Seminiferous Epithelium and Germ Cell Renewal. *Am. J. Anat.*, 1956. **99**: p. 391-413.
55. Meistrich, M.L. and R.C. Samuels, Reduction in Sperm Levels after Testicular Irradiation of the Mouse - a Comparison with Man. *Radiat. Res.*, 1985. **102**: p. 138-147.
56. Strigari, L., et al., Efficacy and toxicity related to treatment of hepatocellular carcinoma with 90Y-SIR spheres: radiobiologic considerations. *J. Nucl. Med.*, 2010. **51**: p. 1377-1385.
57. Wahl, R.L., et al., Prospective SPECT-CT Organ Dosimetry-Driven Radiation-Absorbed Dose Escalation Using the In-111 (In-111)/Yttrium 90 (Y-90) Ibritumomab Tiuxetan (Zevalin(R)) Theranostic Pair in Patients with Lymphoma at Myeloablative Dose Levels. *Cancers*, 2021. **13**: p. 2828.
58. International Commission on Radiation, U. and Measurements, Report 85: Fundamental quantities and units for ionizing radiation. *J ICRU*, 2011. **11**: p. 1-31.
59. Bolch, W.E., et al., MIRD pamphlet No. 21: a generalized schema for radiopharmaceutical dosimetry--standardization of nomenclature. *J. Nucl. Med.*, 2009. **50**: p. 477-484.
60. ICRP (2016), "ICRP Publication 133: The ICRP computational framework for internal dose assessment for reference adults: Specific absorbed fractions,". *Ann. ICRP*. **39**: p. 1-165.
61. Andersson, M., et al., IDAC-Dose 2.1, an internal dosimetry program for diagnostic nuclear medicine based on the ICRP adult reference voxel phantoms. *EJNMMI Res*, 2017. **7**: p. 88.
62. Hobbs, R.F., et al., A nephron-based model of the kidneys for macro-to-micro alpha-particle dosimetry. *Phys. Med. Biol.*, 2012. **57**: p. 4403-4424.
63. Jönsson, L., et al., A dosimetry model for the small intestine incorporating intestinal wall activity and cross-doses. *J. Nucl. Med.*, 2002. **43**: p. 1657-1664.

64. Larsson, E., et al., A small-scale anatomic model for testicular radiation dosimetry for radionuclides localized in the human testes. *J. Nucl. Med.*, 2012. **53**: p. 72-81.
65. Goddu, S.M. and T.F. Budinger, MIRDCellular S. Values: Self-absorbed Dose Per Unit Cumulated Activity for Selected Radionuclides and Monoenergetic Electron and Alpha Particle Emitters Incorporated Into Different Cell Compartments. 1997: Society of Nuclear Medicine.
66. Howell, R.W., The MIRDC Schema: from organ to cellular dimensions. *J. Nucl. Med.*, 1994. **35**: p. 531-533.
67. Roeske, J.C., et al., Small-scale dosimetry: challenges and future directions. *Semin. Nucl. Med.*, 2008. **38**: p. 367-383.
68. Larsson, E., et al., Dosimetry calculations on a tissue level by using the MCNP4c2 Monte Carlo code. *Cancer Biother Radiopharm*, 2005. **20**: p. 85-91.
69. Hobbs, R.F., et al., A bone marrow toxicity model for (2)(2)(3)Ra alpha-emitter radiopharmaceutical therapy. *Phys. Med. Biol.*, 2012. **57**: p. 3207-3222.
70. Gulec, S.A., et al., Hepatic structural dosimetry in (90)Y microsphere treatment: a Monte Carlo modeling approach based on lobular microanatomy. *J. Nucl. Med.*, 2010. **51**: p. 301-310.
71. Hindorf, C., M. Ljungberg, and S.E. Strand, Evaluation of parameters influencing S values in mouse dosimetry. *J. Nucl. Med.*, 2004. **45**: p. 1960-1965.
72. Segars, W.P., et al., Development of a 4-D digital mouse phantom for molecular imaging research. *Mol. Imag. Biol.*, 2004. **6**: p. 149-159.
73. Snyder, W.S., et al., Estimates of Absorbed Fractions for Monoenergetic Photon Sources Uniformly Distributed in Various Organs of a Heterogeneous Phantom. *J. Nucl. Med.*, 1969. **10**: p. 7-&.
74. Zubal, I.G., et al., Computerized 3-Dimensional Segmented Human Anatomy. *Med. Phys.*, 1994. **21**: p. 299-302.
75. ICRP 2009, Adult Reference Computational Phantoms. ICRP Publication 110. *Ann. ICRP*. **39**.
76. Lee, C., et al., The UF series of tomographic computational phantoms of pediatric patients. *Med. Phys.*, 2005. **32**: p. 3537-3548.
77. Segars, W.P., et al., 4D XCAT phantom for multimodality imaging research. *Med. Phys.*, 2010. **37**: p. 4902-4915.
78. Segars, W.P., et al., Population of anatomically variable 4D XCAT adult phantoms for imaging research and optimization. *Med. Phys.*, 2013. **40**.
79. Norris, H., et al., A set of 4D pediatric XCAT reference phantoms for multimodality research. *Med. Phys.*, 2014. **41**.
80. Larsson, E., et al., Mouse S-factors based on Monte Carlo simulations in the anatomical realistic Moby phantom for internal dosimetry. *Cancer Biother Radiopharm*, 2007. **22**: p. 438-442.
81. Zaidi, H., Relevance of accurate Monte Carlo modeling in nuclear medical imaging. *Med. Phys.*, 1999. **26**: p. 574-608.
82. X-5 Monte Carlo Team (I), MCNP - A General Monte Carlo N-Particle Transport Code., Version 5, Volume I: Overview and theory, Los Alamos National Laboratory report, LA-UR-03-1987.
83. Klein, O.N., T., Über die Streuung von Strahlung durch freie Elektronen nach der neuen relativistischen Quantendynamik von Dirac. *Zeitschrift für Physik*, 1929. **52**: p. 853-868.
84. Pelowitz, D.B., MCNPX User's Manual. 2011: p. Version 2.7.0, Los Alamos National Laboratory report, LA-CP-11-00438.
85. Nelson, W.R., Hirayama, H., and Rogers, D.W.O., The EGS4 code system. 1985, Stanford, California, USA.
86. Bielajew, A.F. and D.W.O. Rogers, Presta - the Parameter Reduced Electron-Step Transport Algorithm for Electron Monte-Carlo Transport. *Nuclear Instruments & Methods in Physics Research Section B-Beam Interactions with Materials and Atoms*, 1987. **18**: p. 165-181.
87. Kim, J. and Y. Jung, Radiation-induced liver disease: current understanding and future perspectives. *Exp. Mol. Med.*, 2017. **49**: p. e359.
88. Joiner, M. and A.v.d. Kogel, *Basic clinical radiobiology*. 4th ed. 2009, London. vi, 375 p.
89. Hall, E.J. and A.J. Giaccia, *Radiobiology for the Radiologist*. Seventh edition ed. 2012: Wolters Kluwer Health.
90. Pouget, J.P., et al., Introduction to radiobiology of targeted radionuclide therapy. *Front Med (Lausanne)*, 2015. **2**: p. 12.

91. Prise, K.M. and J. O'Sullivan, Radiation-induced bystander signalling in cancer therapy. *Nat Rev Cancer*, 2009. **9**: p. 351-360.
92. Lavelle, C. and N. Foray, Chromatin structure and radiation-induced DNA damage: from structural biology to radiobiology. *Int. J. Biochem. Cell Biol.*, 2014. **49**: p. 84-97.
93. McMahon, S.J., The linear quadratic model: usage, interpretation and challenges. *Phys. Med. Biol.*, 2019. **64**.
94. Gustafsson, J., P. Nilsson, and K.S. Gleisner, On the biologically effective dose (BED)-using convolution for calculating the effects of repair: I. Analytical considerations. *Phys. Med. Biol.*, 2013. **58**: p. 1507-1527.
95. Lea, D.E. and D.G. Catcheside, The mechanism of the induction by radiation of chromosome aberrations in *Tradescantia*. *Journal of Genetics*, 1942. **44**: p. 216-245.
96. Barendsen, G.W., Dose fractionation, dose rate and iso-effect relationships for normal tissue responses. *Int. J. Radiat. Oncol. Biol. Phys.*, 1982. **8**: p. 1981-1997.
97. Dale, R.G., Dose-rate effects in targeted radiotherapy. *Phys. Med. Biol.*, 1996. **41**: p. 1871-1884.
98. Fowler, J.F., Radiobiological aspects of low dose rates in radioimmunotherapy. *Int. J. Radiat. Oncol. Biol. Phys.*, 1990. **18**: p. 1261-1269.
99. Barone, R., et al., Patient-specific dosimetry in predicting renal toxicity with (90)Y-DOTATOC: relevance of kidney volume and dose rate in finding a dose-effect relationship. *J. Nucl. Med.*, 2005. **46 Suppl 1**: p. 99S-106S.
100. Wessels, B.W., et al., MIRD pamphlet No. 20: the effect of model assumptions on kidney dosimetry and response--implications for radionuclide therapy. *J. Nucl. Med.*, 2008. **49**: p. 1884-1899.
101. Frey, B., et al., Antitumor immune responses induced by ionizing irradiation and further immune stimulation. *Cancer Immunol. Immunother.*, 2014. **63**: p. 29-36.
102. Aerts, A., et al., EANM position paper on the role of radiobiology in nuclear medicine. *Eur J Nucl Med Mol Imaging*, 2021. **48**: p. 3365-3377.
103. Rogakou, E.P., et al., DNA double-stranded breaks induce histone H2AX phosphorylation on serine 139. *J. Biol. Chem.*, 1998. **273**: p. 5858-5868.
104. Löbrich, M., et al., gammaH2AX foci analysis for monitoring DNA double-strand break repair: strengths, limitations and optimization. *Cell Cycle*, 2010. **9**: p. 662-669.
105. Lassmann, M., et al., In vivo formation of gamma-H2AX and 53BP1 DNA repair foci in blood cells after radioiodine therapy of differentiated thyroid cancer. *J. Nucl. Med.*, 2010. **51**: p. 1318-1325.
106. Schumann, S., et al., DNA Damage in Blood Leukocytes of Prostate Cancer Patients Undergoing PET/CT Examinations with [Ga-68]Ga-PSMA I&T. *Cancers*, 2020. **12**.
107. Schumann, S., et al., alpha-Particle-induced DNA damage tracks in peripheral blood mononuclear cells of [Ra-223]RaCl₂-treated prostate cancer patients. *Eur. J. Nucl. Med. Mol. Imag.*, 2021. **48**: p. 2761-2770.
108. Schumann, S., et al., DNA damage in leukocytes after internal ex-vivo irradiation of blood with the alpha-emitter Ra-223. *Scientific Reports*, 2018. **8**.
109. Schumann, S., et al., Correlation of the absorbed dose to the blood and DNA damage in leukocytes after internal ex-vivo irradiation of blood samples with Ra-224. *Ejnm Research*, 2018. **8**.
110. Rogakou, E.P., et al., Initiation of DNA fragmentation during apoptosis induces phosphorylation of H2AX histone at serine 139. *J. Biol. Chem.*, 2000. **275**: p. 9390-9395.
111. Inagaki, A., S. Schoenmakers, and W.M. Baarends, DNA double strand break repair, chromosome synapsis and transcriptional silencing in meiosis. *Epigenetics*, 2010. **5**: p. 255-266.
112. Blanco-Rodriguez, J., gammaH2AX marks the main events of the spermatogenic process. *Microsc. Res. Tech.*, 2009. **72**: p. 823-832.
113. Ramos-Vara, J.A. and M.A. Miller, When tissue antigens and antibodies get along: revisiting the technical aspects of immunohistochemistry--the red, brown, and blue technique. *Vet. Pathol.*, 2014. **51**: p. 42-87.
114. Chan, J.K., The wonderful colors of the hematoxylin-eosin stain in diagnostic surgical pathology. *Int J Surg Pathol*, 2014. **22**: p. 12-32.
115. Hughes, J. and G. Gobe, Identification and quantification of apoptosis in the kidney using morphology, biochemical and molecular markers. *Nephrology (Carlton)*, 2007. **12**: p. 452-458.

116. Noda, A., et al., Unrepairable DNA double-strand breaks that are generated by ionising radiation determine the fate of normal human cells. *J. Cell Sci.*, 2012. **125**: p. 5280-5287.
117. Scholzen, T. and J. Gerdes, The Ki-67 protein: from the known and the unknown. *J. Cell. Physiol.*, 2000. **182**: p. 311-322.
118. Sak, A. and M. Stuschke, Use of gammaH2AX and other biomarkers of double-strand breaks during radiotherapy. *Semin. Radiat. Oncol.*, 2010. **20**: p. 223-231.
119. Buchwalow, I.B. and W. Böcker, *Immunohistochemistry : basics and methods*. 2010, Heidelberg ; New York: Springer. x, 153 p.
120. Pawley, J.B., *Handbook of biological confocal microscopy*. 3rd ed. 2006, New York, NY: Springer. xxviii, 985 p.
121. Price, R.L. and W.G. Jerome, *Basic confocal microscopy*. 2011, New York: Springer. xi, 302 p.
122. Foster, B., et al., A review on segmentation of positron emission tomography images. *Comput. Biol. Med.*, 2014. **50**: p. 76-96.
123. Erdi, Y.E., et al., Threshold estimation in single photon emission computed tomography and planar imaging for clinical radioimmunotherapy. *Cancer Res.*, 1995. **55**: p. 5823s-5826s.
124. Rasband, W.S., ImageJ. U.S. National Institutes of Health, Bethesda, Maryland, USA, <http://imagej.nih.gov/ij/>, 1997-2014.
125. Hamer, G., et al., DNA double-strand breaks and gamma-H2AX signaling in the testis. *Biol. Reprod.*, 2003. **68**: p. 628-634.
126. Du, G., et al., Spatial dynamics of DNA damage response protein foci along the ion trajectory of high-LET particles. *Radiat. Res.*, 2011. **176**: p. 706-715.
127. Peterson, T.E. and L.R. Furenlid, SPECT detectors: the Anger Camera and beyond. *Phys. Med. Biol.*, 2011. **56**: p. R145-182.
128. Anger, H.O., Use of a Gamma-Ray Pinhole Camera for In vivo Studies. *Nature*, 1952. **170**: p. 200-201.
129. Anger, H.O., Scintillation Camera. *Rev. Sci. Instrum.*, 1958. **29**: p. 27-33.
130. Patton, J.A. and T.G. Turkington, SPECT/CT physical principles and attenuation correction. *J. Nucl. Med. Technol.*, 2008. **36**: p. 1-10.
131. Zaidi, H. and K.F. Koral, Scatter modelling and compensation in emission tomography. *Eur. J. Nucl. Med. Mol. Imag.*, 2004. **31**: p. 761-782.
132. Frey, E.C. and B.M.W. Tsui, A new method for modeling the spatially-variant, object-dependent scatter response function in SPECT. 1996 Ieee Nuclear Science Symposium - Conference Record, Vols 1-3, 1997: p. 1082-1086.
133. Rahmim, A. and H. Zaidi, PET versus SPECT: strengths, limitations and challenges. *Nucl. Med. Commun.*, 2008. **29**: p. 193-207.
134. Erlandsson, K., et al., A review of partial volume correction techniques for emission tomography and their applications in neurology, cardiology and oncology. *Phys. Med. Biol.*, 2012. **57**: p. R119-159.
135. Hutton, B.F. and A. Osiecki, Correction of partial volume effects in myocardial SPECT. *J. Nucl. Cardiol.*, 1998. **5**: p. 402-413.
136. Jönsson, L., et al., Quantitative analysis of phantom studies of (111)In and (68)Ga imaging of neuroendocrine tumours. *EJNMMI Phys*, 2018. **5**: p. 5.
137. Gustafsson, J., A. Sundlöv, and K. Sjögreen Gleisner, SPECT image segmentation for estimation of tumour volume and activity concentration in (177)Lu-DOTATATE radionuclide therapy. *EJNMMI Res*, 2017. **7**: p. 18.
138. Dewaraja, Y.K., et al., MIRD pamphlet No. 23: quantitative SPECT for patient-specific 3-dimensional dosimetry in internal radionuclide therapy. *J. Nucl. Med.*, 2012. **53**: p. 1310-1325.
139. Bruyant, P.P., Analytic and iterative reconstruction algorithms in SPECT. *J. Nucl. Med.*, 2002. **43**: p. 1343-1358.
140. Tsui, B.M. and E.C. Frey, *Quantitative analysis in nuclear medicine imaging*, H. Zaidi, Editor. 2006, Springer. p. 82-106.
141. Shepp, L.A. and Y. Vardi, Maximum likelihood reconstruction for emission tomography. *IEEE Trans. Med. Imaging*, 1982. **1**: p. 113-122.

142. Hudson, H.M. and R.S. Larkin, Accelerated Image-Reconstruction Using Ordered Subsets of Projection Data. *IEEE Trans. Med. Imaging*, 1994. **13**: p. 601-609.
143. Vargas, C.S., et al., An international multi-center investigation on the accuracy of radionuclide calibrators in nuclear medicine theragnostics. *Ejnmni Physics*, 2020. **7**.
144. Sandström, M., et al., Method dependence, observer variability and kidney volumes in radiation dosimetry of (177)Lu-DOTATATE therapy in patients with neuroendocrine tumours. *EJNMNI Phys*, 2015. **2**: p. 24.
145. Firouzian, A., M.D. Kelly, and J.M. Declerck, Insight on automated lesion delineation methods for PET data. *Ejnmni Research*, 2014. **4**.
146. Brolin, G., et al., Pharmacokinetic digital phantoms for accuracy assessment of image-based dosimetry in (177)Lu-DOTATATE peptide receptor radionuclide therapy. *Phys. Med. Biol.*, 2015. **60**: p. 6131-6149.
147. Roth, D., et al., A method for tumor dosimetry based on hybrid planar-SPECT/CT images and semiautomatic segmentation. *Med. Phys.*, 2018. **45**: p. 5004-5018.
148. Ljungberg, M., et al., A 3-dimensional absorbed dose calculation method based on quantitative SPECT for radionuclide therapy: Evaluation for I-131 using Monte Carlo simulation. *J. Nucl. Med.*, 2002. **43**: p. 1101-1109.
149. Roth, D., et al., Dosimetric Quantities in Neuroendocrine Tumors over Treatment Cycles with (177)Lu-DOTATATE. *J. Nucl. Med.*, 2022. **63**: p. 399-405.
150. Sanchez-Crespo, A., Comparison of Gallium-68 and Fluorine-18 imaging characteristics in positron emission tomography. *Appl. Radiat. Isot.*, 2013. **76**: p. 55-62.
151. Watson, C.C., D. Newport, and M.E. Casey, A single scatter simulation technique for scatter correction in 3D pet. *Three-Dimensional Image Reconstruction in Radiology and Nuclear Medicine*, 1996. **4**: p. 255-268.
152. Boellaard, R., et al., FDG PET/CT: EANM procedure guidelines for tumour imaging: version 2.0. *Eur. J. Nucl. Med. Mol. Imag.*, 2015. **42**: p. 328-354.
153. Ilan, E., et al., Tumor-to-Blood Ratio for Assessment of Somatostatin Receptor Density in Neuroendocrine Tumors Using Ga-68-DOTATOC and Ga-68-DOTATATE. *J. Nucl. Med.*, 2020. **61**: p. 217-221.
154. Boellaard, R., Standards for PET Image Acquisition and Quantitative Data Analysis. *J. Nucl. Med.*, 2009. **50**: p. 11s-20s.
155. Reubi, J.C. and A. Schonbrunn, Illuminating somatostatin analog action at neuroendocrine tumor receptors. *Trends Pharmacol. Sci.*, 2013. **34**: p. 676-688.
156. Bozkurt, M.F., et al., Guideline for PET/CT imaging of neuroendocrine neoplasms with Ga-68-DOTA-conjugated somatostatin receptor targeting peptides and F-18-DOPA. *Eur. J. Nucl. Med. Mol. Imag.*, 2017. **44**: p. 1588-1601.
157. Kunikowska, J., et al., Semiquantitative Analysis and Characterization of Physiological Biodistribution of Ga-68-DOTA-TATE PET/CT. *Clin. Nucl. Med.*, 2012. **37**: p. 1052-1057.
158. Kwekkeboom, D.J., et al., Radiolabeled somatostatin analog [Lu-177-DOTA(0),Tyr(3)] octreotate in patients with endocrine gastroenteropancreatic tumors. *J. Clin. Oncol.*, 2005. **23**: p. 2754-2762.
159. Gálne, A., et al., A Prospective Observational Study to Evaluate the Effects of Long-Acting Somatostatin Analogs on Ga-68-DOTATATE Uptake in Patients with Neuroendocrine Tumors. *J. Nucl. Med.*, 2019. **60**: p. 1717-1723.
160. Sandström, M., et al., Comparative biodistribution and radiation dosimetry of 68Ga-DOTATOC and 68Ga-DOTATATE in patients with neuroendocrine tumors. *J. Nucl. Med.*, 2013. **54**: p. 1755-1759.
161. Velikyan, I., et al., Quantitative and Qualitative Inpatient Comparison of Ga-68-DOTATOC and Ga-68-DOTATATE: Net Uptake Rate for Accurate Quantification. *J. Nucl. Med.*, 2014. **55**: p. 204-210.
162. Kletting, P., et al., Differences in predicted and actually absorbed doses in peptide receptor radionuclide therapy. *Med. Phys.*, 2012. **39**: p. 5708-5717.
163. Kletting, P., et al., Optimized Peptide Amount and Activity for Y-90-Labeled DOTATATE Therapy. *J. Nucl. Med.*, 2016. **57**: p. 503-508.

164. Sandström, M., et al., Individualized Dosimetry of Kidney and Bone Marrow in Patients Undergoing Lu-177-DOTA-Octreotate Treatment. *J. Nucl. Med.*, 2013. **54**: p. 33-41.
165. Cremonesi, M., et al., Dosimetry in peptide radionuclide receptor therapy: A review. *J. Nucl. Med.*, 2006. **47**: p. 1467-1475.
166. Huizing, D.M.V., et al., Multicentre quantitative (68)Ga PET/CT performance harmonisation. *EJNMMI Phys*, 2019. **6**: p. 19.
167. Bailey, D.L., et al., Accuracy of Dose Calibrators for (68)Ga PET Imaging: Unexpected Findings in a Multicenter Clinical Pretrial Assessment. *J. Nucl. Med.*, 2018. **59**: p. 636-638.
168. Sainz-Esteban, A., et al., Comparison of sequential planar Lu-177-DOTA-TATE dosimetry scans with Ga-68-DOTA-TATE PET/CT images in patients with metastasized neuroendocrine tumours undergoing peptide receptor radionuclide therapy. *Eur. J. Nucl. Med. Mol. Imag.*, 2012. **39**: p. 501-511.
169. Ezziddin, S., et al., Does the Pretherapeutic Tumor SUV in Ga-68 DOTATOC PET Predict the Absorbed Dose of Lu-177 Octreotate? *Clin. Nucl. Med.*, 2012. **37**: p. E141-E147.
170. Hänscheid, H., et al., PET SUV correlates with radionuclide uptake in peptide receptor therapy in meningioma. *Eur. J. Nucl. Med. Mol. Imag.*, 2012. **39**: p. 1284-1288.
171. Kratochwil, C., et al., SUV of [Ga-68]DOTATOC-PET/CT Predicts Response Probability of PRRT in Neuroendocrine Tumors. *Mol. Imag. Biol.*, 2015. **17**: p. 313-318.
172. Krebs, S., et al., Comparison of (68)Ga-DOTA-JR11 PET/CT with dosimetric (177)Lu-satoreotide tetraxetan ((177)Lu-DOTA-JR11) SPECT/CT in patients with metastatic neuroendocrine tumors undergoing peptide receptor radionuclide therapy. *Eur J Nucl Med Mol Imaging*, 2020. **47**: p. 3047-3057.
173. Haug, A.R., et al., Ga-68-DOTATATE PET/CT for the Early Prediction of Response to Somatostatin Receptor-Mediated Radionuclide Therapy in Patients with Well-Differentiated Neuroendocrine Tumors. *J. Nucl. Med.*, 2010. **51**: p. 1349-1360.
174. Bland, J.M. and D.G. Altman, Calculating correlation coefficients with repeated observations: Part 1--Correlation within subjects. *BMJ*, 1995. **310**: p. 446.
175. Bland, J.M. and D.G. Altman, Calculating correlation coefficients with repeated observations: Part 2--Correlation between subjects. *BMJ*, 1995. **310**: p. 633.
176. Peters, S.M.B., et al., [Ga-68]Ga-PSMA-11 PET imaging as a predictor for absorbed doses in organs at risk and small lesions in [Lu-177]Lu-PSMA-617 treatment. *Eur. J. Nucl. Med. Mol. Imag.*, 2022. **49**: p. 1101-1112.
177. Meerkhan, S.A., et al., Testis dosimetry in individual patients by combining a small-scale dosimetry model and pharmacokinetic modeling-application of In-111-Ibritumomab Tiuxetan (Zevalin (R)). *Phys. Med. Biol.*, 2014. **59**: p. 7889-7904.
178. Knight, J.C., S. Koustoulidou, and B. Cornelissen, Imaging the DNA damage response with PET and SPECT. *Eur. J. Nucl. Med. Mol. Imag.*, 2017. **44**: p. 1065-1078.
179. Gear, J.L., et al., EANM practical guidance on uncertainty analysis for molecular radiotherapy absorbed dose calculations. *Eur J Nucl Med Mol Imaging*, 2018. **45**: p. 2456-2474.
180. Jimenez-Franco, L.D., et al., Treatment planning algorithm for peptide receptor radionuclide therapy considering multiple tumor lesions and organs at risk. *Med. Phys.*, 2018. **45**: p. 3516-3523.
181. Kletting, P., et al., Modeling and Predicting Tumor Response in Radioligand Therapy. *J. Nucl. Med.*, 2019. **60**: p. 65-70.
182. Xue, S., et al., Application of machine learning to pretherapeutically estimate dosimetry in men with advanced prostate cancer treated with (177)Lu-PSMA I&T therapy. *Eur J Nucl Med Mol Imaging*, 2022.